To the Graduate Council:

I am submitting herewith a thesis written by Kyung-Ju Choi entitled "Orientation Development in Tubular Film Extrusion of Polyethylene and Polystyrene." I recommend that it be accepted in partial fulfillment of the requirements for the degree of Master of Science, with a major in Polymer Engineering.

J. E. Spruiell

Joseph E. Spruiell, Major Professor

We have read this thesis and recommend its acceptance:

Jesse D. White

Edward S. Clark

Accepted for the Council

L. Evans Reed

Vice Chancellor
Graduate Studies and Research

ORIENTATION DEVELOPMENT IN TUBULAR FILM EXTRUSION OF POLYETHYLENE AND POLYSTYRENE

A Thesis

Presented for the

Master of Science

Degree

The University of Tennessee, Knoxville

Kyung-Ju Choi

August 1980

ACKNOWLEDGEMENTS

The author would like to express his deepest and sincere appreciation to both Dr. J. E. Spruiell and Dr. J. L. White, his advisors, for their advice and guidance throughout this research study and for their help in the preparation of this manuscript.

Thanks are extended to Dr. E. S. Clark for his interest and advice in this program and to the Chemplex Company for providing the polymer for research. Financial assistance provided by the Chemical, Metallurgical and Polymer Engineering Department is gratefully acknowledged.

Finally the author expresses his greatest love and appreciation to his wife and his son for their support.

ABSTRACT

Orientation in tubular film extrusion of atactic polystyrene and high density polyethylene were studied as a function of the stresses in the melt at the point of vitrification (polystyrene) or crystallization (polyethylene). The film forming conditions were varied over a wide range so that the orientation could be varied from essentially uniaxial orientation to approximately equal biaxial orientation. In the polystyrene samples the orientation was determined from measurements of the in-plane and out-of-plane birefringence. Both birefringence and wide angle x-ray pole figures were used for studying orientaion in polyethylene. Small angle x-ray scattering patterns were used to help further characterize the morphology of the polyethylene as a function of the kinematics (drawdown, blow-up ratio) and applied tensions and bubble pressures.

Both polystyrene and polyethylene experimental results are interpreted in terms of White and Spruiell's biaxial orientation factors.

The data for the amorphous polymer, polystyrene, can be correlated by comparing the birefringences with the stresses acting in the film at the position of vitrification. These data compare quantitatively with the Rheo-Optical Law and with Oda, White and Clark's correlation developed for the birefringence of samples vitrified during shear and uniaxial extensional flow.

The polyethylene films showed much higher levels of crystalline orientation from WAXS than would be expected from the Rheo-Optical Law

due to oriented nucleation and growth of crystals. The morphological changes of polyethylene with processing conditions are described. With uniaxial state, row structure first described by Keller is favored. A biaxially oriented sample exhibited a morphology which could be interpreted in terms of the superposition of two row structure components with one component having lamellae stacked along the machine direction and one component having lamellae stacked along the transverse direction.

TABLE OF CONTENTS

CHAPTER PAGE

LIST OF TABLES

LIST OF FIGURES

FIGURE PAGE

CHAPTER 1

INTRODUCTION

The tubular blown film process is the most important fabrication method for the production of thermoplastic films. This process is most commonly used for polymer film manufacturing operation because of its better economics and satisfactory mechanical properties. Although for many years the blown film process has been widely used, relatively little study of the process has been reported. This may be due to the complexity of the process.

In the film-blowing process the tube of extruded molten polymer is extended in both the transverse and the axial directions. Therefore this process should be treated from the point of view of a multiaxial or approximately biaxial elongational flow. The morphology and degree of orientation of macromolecules probably governs the physical properties of the finished film, such as the tensile strength, tear resistance, and heat seal characteristics; it is thus expected that a biaxially oriented film would have different physical properties from what a uniaxially oriented film would have. For these reasons one of the most technologically important areas associated with this process is the influence of the kinematics, stress fields and cooling conditions on the development of the structure, orientation and morphology of the products. Sometimes the process is operated in a uniaxial mode as in the seed packaging process with no inflation of the bubble. There has been much investigation on uniaxial elongational

flow in the analyses of fiber spinning process but biaxial elongational flow has been little investigated.

The purpose of this thesis is to determine the orientation development in both vitrifying polystyrene melt and crystallizing polyethylene melts produced in tubular film extrusion. For the crystallizing melts we shall determine as full a picture of the total crystalline morphology as we can.

CHAPTER 2

BACKGROUND REVIEW AND LITERATURE SURVEY

2.1 TUBULAR FILM PROCESS

The film-blowing process (see Figure 2.1) is a procedure by which thin thermoplastic films are produced by means of extruding a polymer melt through an annular die with pressure slightly higher than the ambient, maintained inside the moving bubble of melt. The molten polymer tube exiting from the die is drawn by a take-up device and expanded circumferentially by the internal pressure produced by blowing air into the tube. The air inflates the tube into a bubble of thin film. Usually an air cooling ring is installed around the bubble. As the bubble moves along the machine direction, it cools and solidifies at a certain distance from the die exit. The air cooling ring not only serves to cool the bubble, also helps shape and stabilize it. It is used to control the frost line height. Blown film dies are further varied by designs for pressure drops through the die. The pressure drop can be described as the pressure at which the die system operates as indicated by the pressure gage on the adapter. The die output must be balanced. The blow-up ratio, B , is the ratio of final bubble diameter to die diameter. The most common blow-up ratios for commercial films seem to be in the range 1 to 3.0. Films produced by this method are primarily polyethylene and some polypropylene, polybutene-1 and polystyrene, etc.

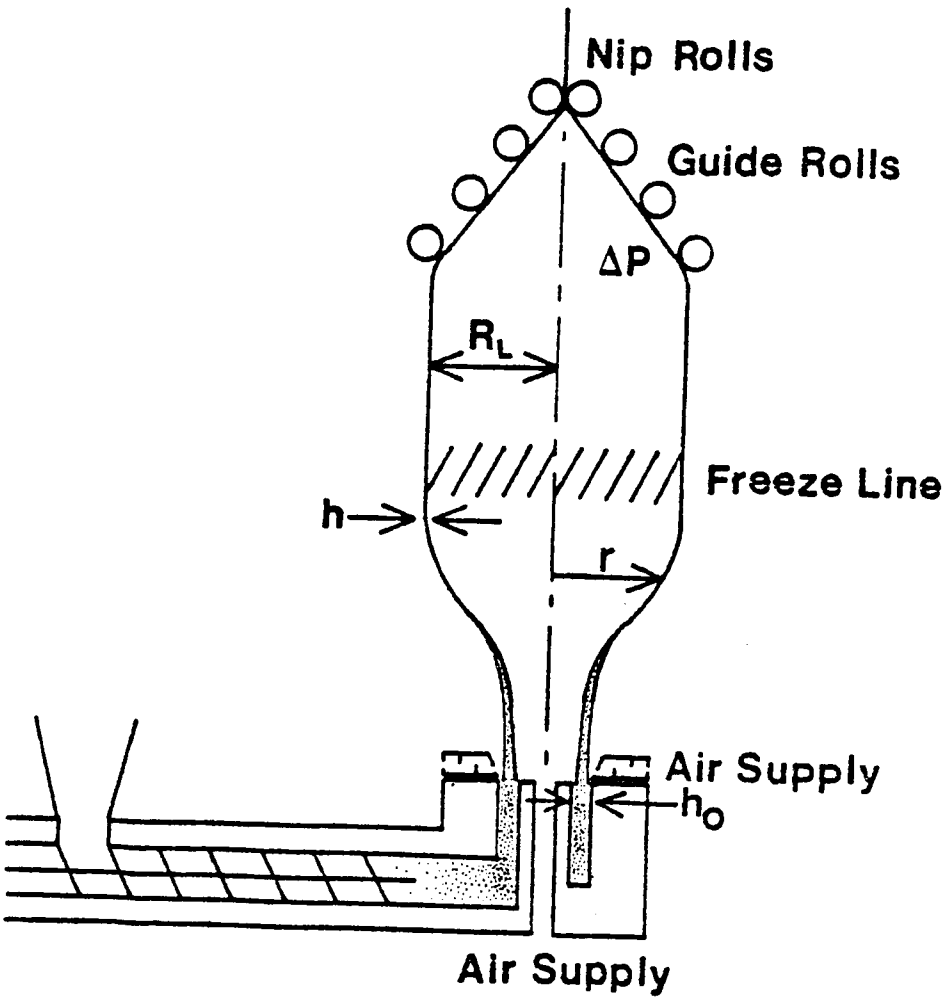

Figure 2.1 Tubular film extrusion process.

2.2 DYNAMICS AND FORCE BALANCE

The dynamics of the tubular film process are rather complex due to the expansion of the bubble. It was only in 1965 that appropriate force balance equations were developed by Alfrey (3) using the theory of mechanical equilibrium of shells of rotational symmetry. In 1970, the dynamics of this process were developed in great detail in a series of papers by Pearson and Petrie (66-68) presuming the film is a thin shell. The assumptions made are that the film thickness is small compared with other dimensions of the bubble including its radii of curvature, and that the velocity gradients can be approximated locally by those of a plane film being extended biaxially. This study is reviewed in monographs by Han (21) and Middleman (52). Here force balances in both the longitudinal and radial directions must be considered. The longitudinal or vertical force balance has the form

$$F_{rheo} = F_L - F_{grav} - F_{drag} - \pi(R_L^2 - r^2)\Delta P \qquad 2.1$$

where F_L is the applied tension on the film, F_{grav} is the gravitational force, F_{drag} is the air drag force, r is the radius of the bubble at an arbitrary position, R_L is the maximum radius, ΔP is the pressure difference across the film, and F_{rheo} is the rheological force which is the product of the acting stress, σ_{11}, in the film in the machine direction and the cross-sectional area;

$$F_{rheo} = 2\pi r h \sigma_{11} \cos\theta \qquad 2.2$$

Here h is the thickness of the film, θ is the angle between a tangent to the film and the vertical. When we neglect the effect of the gravity force and drag force, then the basic force balance along the

machine direction is rewritten as

$$F_L = 2\pi r h \sigma_{11} \cos\theta + \pi(R_L^2 - r^2)\Delta P \qquad 2.3$$

The radial force balance is given by

$$\Delta P = h\left(\frac{\sigma_{11}}{R_M} + \frac{\sigma_{22}}{R_H}\right) \qquad 2.4$$

in which σ_{22} is the circumferential stress and R_M and R_H are the principal radii of curvature in the local Cartesian coordinates at a point on the surface of the film. They are defined by

$$R_M = -\frac{\sec^3\theta}{\frac{d^2 r}{dz^2}} \qquad 2.5$$

$$R_H = r \sec\theta \qquad 2.6$$

This is illustrated in Figure 2.2.

At the freeze-line

$$R_M = \infty$$

$$R_H = R_L \qquad 2.7$$

$$\cos\theta = 1$$

Therefore at this position

$$\sigma_{11} = \frac{F_L}{2\pi R_L h} \quad , \quad \sigma_{22} = \frac{R_L \Delta P}{h} \qquad 2.8$$

2.3 KINEMATICS

Pearson and Petrie (68) proposed the coordinate system shown in Figure 2.2 for tubular film extrusion. The Cartesian coordinates (ξ_1 , ξ_2 , ξ_3) at a point P on the surface of the film are related to the cylindrical coordinates (r , θ , z). Here (v_1 , v_2 , v_3) are

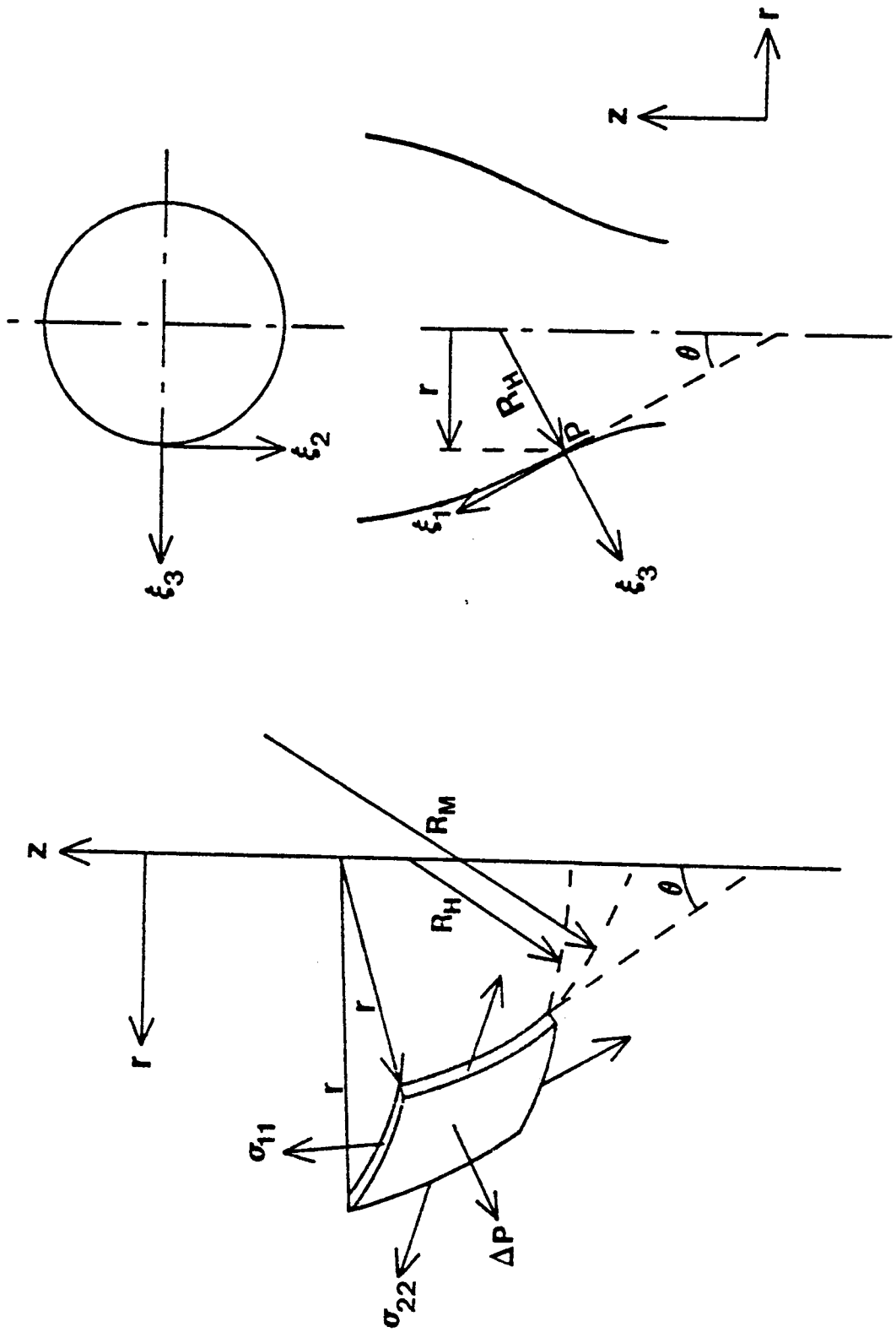

Figure 2.2 Coordinate systems for deformation of a bubble.

velocity components in the coordinates (ξ_1 , ξ_2 , ξ_3), h is the film thickness, r is the bubble diameter, (Z_L , R_L , h_L) and (z_o , R_o , h_o) are the height, the diameter and the thickness of film at the freeze line and at the die respectively, and r and h are functions of z. The rate of deformation tensor, $\underset{\sim}{d}$, for the melt on the deforming bubble is given by

$$\underset{\sim}{d} = \frac{1}{2}\left[\nabla \underset{\sim}{V} + (\nabla \underset{\sim}{V})^{T}\right] = \begin{vmatrix} \frac{\partial V_1}{\partial \xi_1} & 0 & 0 \\ 0 & \frac{\partial V_2}{\partial \xi_2} & 0 \\ 0 & 0 & \frac{\partial V_3}{\partial \xi_3} \end{vmatrix} \qquad 2.9$$

in which

$$d_{22} = \frac{V_1}{r}\frac{dr}{d\xi_1} \qquad 2.10$$

$$d_{33} = \frac{V_3}{h} = \frac{1}{h}\frac{dh}{dt} = \frac{1}{h}\frac{dh}{d\xi_1}\frac{d\xi_1}{dt} = \frac{1}{h}\frac{dh}{d\xi_1}V_1 \qquad 2.11$$

for an incompressible fluid

$$\begin{aligned} d_{11} &= -\left(d_{22} + d_{33}\right) \\ &= -V_1\left(\frac{1}{r}\frac{dr}{d\xi_1} + \frac{1}{h}\frac{dh}{d\xi_1}\right) \end{aligned} \qquad 2.12$$

Therefore $\underset{\sim}{d}$ is rewritten as

$$\underset{\sim}{d} = \frac{Q\cos\theta}{\pi r h} \begin{vmatrix} -\frac{1}{r}\frac{dr}{dz} - \frac{1}{h}\frac{dh}{dz} & 0 & 0 \\ 0 & \frac{1}{r}\frac{dr}{dz} & 0 \\ 0 & 0 & \frac{1}{h}\frac{dh}{dz} \end{vmatrix} \qquad 2.13$$

in which Q is the volumetric flow rate ($Q = 2\pi r h v_1$, $d\xi_1 = dz/\cos\theta$). Different special cases may be noted. For uniaxial extension $d_{22} = d_{33} = -0.5 d_{11}$. For biaxial extension $d_{11} = d_{22} = -2 d_{33}$. As shown by Han and Park (23) both types of deformation may be carried out in film blowing processes. For the different cases mentioned in the above paragraph we have

Uniaxial Extension

$$\frac{\partial V_2}{\partial \xi_2} = \frac{\partial V_3}{\partial \xi_3} = -\frac{1}{2}\frac{\partial V_1}{\partial \xi_1}$$

$$\frac{1}{r}\frac{dr}{dz} = \frac{1}{h}\frac{dh}{dz} \qquad 2.14$$

from which it follows that r/h is constant and the drawdown ratio (v_L / v_o) is related to bubble shape and film thickness by

$$\frac{V_L}{V_o} = \frac{h_o^2}{h_L^2} = \frac{R_o^2}{R_L^2} = \frac{1}{B^2} \qquad 2.15$$

For v_L / v_o greater than unity, the blow-up ratio B, R_L / R_o ,is less than unity

Planar Extension

$$\frac{\partial V_2}{\partial \xi_2} = 0 \quad , \quad \frac{\partial V_3}{\partial \xi_3} = -\frac{\partial V_1}{\partial \xi_1}$$

$$\frac{1}{r}\frac{dr}{dz} = 0 \quad , \quad \frac{1}{h}\frac{dh}{dz} = \frac{Q\cos\theta}{\pi r h}\left(\frac{1}{r}\frac{dr}{dz} - \frac{1}{h}\frac{dh}{dz}\right) \qquad 2.16$$

This implies that r is constant, which means the blow-up ratio B is unity

$$B = \frac{R_L}{R_o} = 1 \qquad 2.17$$

,and the drawdown ratio is related to the film thickness through

$$\frac{V_L}{V_o} = \frac{h_o}{h_L} \qquad 2.18$$

Equal Biaxial Extension

$$\frac{\partial V_2}{\partial \xi_2} = \frac{\partial V_1}{\partial \xi_1} \quad , \quad \frac{\partial V_3}{\partial \xi_3} = -2\frac{\partial V_1}{\partial \xi_1}$$

$$\frac{1}{r}\frac{dr}{dz} = -\frac{1}{r}\frac{dh}{dz} - \frac{1}{r}\frac{dR}{dz} \qquad 2.19$$

this leads to r^2h being constant and the drawdown ratio v_L/v_o being related to blow-up ratio by

$$\frac{V_L}{V_o} = \left(\frac{h_o}{h_L}\right)^{1/2} = \frac{R_L}{R_o} = B \qquad 2.20$$

The drawdown ratio is equal to blow-up ratio. Large v_L/v_o requires large blow-up ratios.

Unequal Biaxial Extension

$$\frac{\partial V_1}{\partial \xi_1} > \frac{\partial V_2}{\partial \xi_2} \quad or \quad \frac{\partial V_1}{\partial \xi_1} < \frac{\partial V_2}{\partial \xi_2} \qquad 2.21$$

this is equivalent to

$$\frac{V_L}{V_o} > B \quad or \quad \frac{V_L}{V_o} < B \qquad 2.22$$

respectively.

Basic experimental studies of kinematics are reported by Ast(4), Farber and Dealy (16), and Han and Park (23). Farber and Dealy (16) discuss motion picture techniques of following deformation history.

Han and Park also use photographs and carry out experiments ranging from uniaxial to biaxial extension through variation of the air pressure within the bubble.

2.4 HEAT TRANSFER

Heat is transported by conduction, convection and radiation. Since the film is thin enough, the heat conduction in the film is negligible. Therefore the heat loses are controlled by radiative and convective heat transfer;

$$q_t = q_r + q_c \qquad 2.23$$

where q_t is total heat transfer, q_r is heat transfer by radiation, q_c is heat transfer by convection.

A. HEAT TRANSFER BY RADIATION

$$q_r = \epsilon_t \sigma_s A_B \left[\left(\frac{T_B}{100} \right)^4 - \left(\frac{T_E}{100} \right)^4 \right] \qquad 2.24$$

where ϵ_t is total emission coefficient, σ_s is the radiation number of a black body ($\sigma_s = 4.96$), A_B is bubble surface area, and T_B and T_E are the bubble and environmental temperature.

Menges and Predohl (51) argue that the total emission coefficient is given by

$$\epsilon_t = \epsilon(2 - \epsilon) \qquad 2.25$$

where ϵ is emission due to thickness.

Calculating the heat transfer by radiation is a single step for the whole bubble is not yet possible because no uniform expression for

the temperature profile along the bubble, $T_B(z)$, could be found. The total value of q_r amount to 10-20 percent of the whole heat transfer rate.

B. HEAT TRANSFER BY CONVECTION

Heat transfer to the interior of the bubble is small since at thermal equilibrium the air inside the bubble cannot act as a heat sink. Hence heat transfer outward is dominant and is only considered.

The heat transfer by convection is given by

$$q_c = h(z)\, A_B\, (T_B - T_A) \qquad 2.26$$

where $h(z)$ is the heat transfer coefficient, T_B is the bubble temperature, T_A is the cooling air temperature.

Zeppenfeld (94) has developed on empirical correlationship between the heat transfer coefficient and cooling air velocity;

$$h(z) = 7.11\, w^{0.78} \qquad 2.27$$

where w is the cooling air mean velocity.

Menges and Predohl (51) experimentally determined the convective heat transfer coefficient. This was found to be the form

$$h(z) = 3.3(w_{max})^{1.5} \qquad 2.28$$

for heavy duty sacks

$$h(z) = 3.04(w_{max})^{1.3} \qquad 2.29$$

in which w_{max} is maximum cooling air velocity, $w_{max} = w_{max,F_L}\,(Z_L/z)^{0.74}$ and w_{max,F_L} is maximum air velocity at the freeze line and Z_L is the freeze line height. They combined these equations and then finally they obtained the following result.

$$q_c = 3.3\, D(w_{max,F_L})^{1.5} \times 9.1 \times Z_L^{1.11} \times \left\{-\theta_{F_L}(Z_2^{-0.11} - Z_1^{-0.11}) + 28.5\left[-\ln Z_L(Z_2^{-0.11} - Z_1^{-0.11}) + Z_2^{-0.11}(\ln Z_2 + 9.1) - Z_1^{-0.11}(\ln Z_1 + 9.1)\right]\right\} \qquad 2.30$$

where θ_{F_L} is temperature difference between bubble and air at the freeze line, and D is the diameter of bubble.

Ast (4) performed various experiments with five different cooling air mass flow rates. If the cooling air flow rate is increased, the bubble temperature is decreased with decreasing freeze line height. The blow-up ratio is also affected unless the amount of air inside the bubble is adjusted. He (4) predicted a heat transfer coefficient at each different cooling air rate by his experimental result.

Wagner (87) carried out various experiment which affect the heat transfer coefficient between the bubble surface and the cooling air. He obtained a heat transfer coefficient, h = 30 Kcal /m^2 h °c. His modelling used is based on temperature dependent Newtonian fluid proposed by Pearson and Petrie with energy balance equation.

Petrie (70) describes a fundamental study for heat transfer in film blowing.

2.5 RHEOLOGICAL MODELLING

The original study of the dynamic tubular blown film deals with an isothermal Newtonian melt and is reported by Pearson and Petrie (68). They neglect gravity, inertia, surface tension and any forces due to cooling air (66, 67). In later papers Petrie (69-71) included the surface tension term, as well as the gravity and inertia. The effect of inertia appears to be negligible for all practical purposes.

Han and Park report modelling using a power law fluid with a non-Newtonian elongational viscosity. Petrie (70) has modelled the

tubular film extrusion a convected Maxwell model behavior and a neo-Hookean nonlinear elastic model. Nonisothermal modelling of tubular blown film extrusion has been reported by Petrie (70), Wagner (87) and Han and Park (24).

2.6 ORIENTATION DEVELOPMENT IN FLOWING MELTS AND ITS RELATION TO STRESS

It is well known that a transparent non crystalline solid treated by heating and rapid quenching gives birefringence, which is the difference in magnitude of the principal axes of the refractive index ellipsoid. Early experiments of Brewster (5) showed that application of stresses produced birefringence. Neuman and Maxwell and later authors hypothesized the existance of the Stress-Optical Law which was subsequently verified by experiment. The Stress-Optical or Rheo-Optical Law may be stated

$$\Delta n_{ij} = n_i - n_j = C\,(\sigma_i - \sigma_j) \qquad 2.31$$

where Δn_{ij} is birefringence, $\underset{\sim}{n}$ is the refractive index tensor and σ_i and σ_j are the principal stresses along i and j direction respectively.

Kuhn and Grun (37) first considered the optical properties of a statistically-kinked long chain molecule, composed of optically anisotropic links. They showed that a stretched network of flexible chains could be characterized by two principal refractive indices, corresponding to directions of polarization respectively parallel and perpendicular to the direction of extension. Furhter consideration of

vulcanised rubber as a network of randomly kinked molecular chains was done by Treloar (86). He showed that the birefringence is a simple function of the principal extension and is proportional to the difference between the two corresponding principal stresses, i.e., the Rheo-Optical Law holds for cross linked rubbers.

Polymer molecules in a melt under stress have non-random distributions of orientation and birefringence will occur because it behaves as an anisotropic medium. Lodge (40) was the first to suggest that the Rheo-Optical Law could be applied to polymer solutions and melts. For shear flow he writes

$$\begin{aligned} \Delta n &= C(\sigma_{11} - \sigma_{22}) \cos 2\chi_{opt} \\ &= 2C\,\sigma_{12} / \sin 2\chi_{opt} \end{aligned} \qquad 2.32$$

in which the optical extinction angle χ_{opt} is defined as the angle between the direction of flow and the principal axes of the stress tensor, and σ_{12} is the shear stress. He argued that the stress-optical coefficient should be the same as that for a crosslinked elastomer of the same polymer using an entanglement network model. Philippoff (72) showed the validity of the Rheo-Optical Law on a range of polymer solutions. In shear flow, he showed that birefringence could be successfully used to measure normal stresses. Wales (88) gives a description of a rectangular slit apparatus which can be used for the measurement of flow birefringence of polymer melts at high shear stresses. He can measure Δn_{12} and Δn_{13} by using his apparatus. Han and Drexler (22) carried out similar experiments including measurements

in the entrance region under isothermal conditions. Matsumoto and Bogue (45) have also carried out a detailed experimental verification of the validity of the stress-optical relation in polystyrene under non-isothermal conditions.

2.7 ORIENTATION REPRESENTATION

Maxwell's displacement vector $\underset{\sim}{D}$ has two parts. One part which is present in the absence of the molecules, the other part which is produced by the molecules, so called polarization vector $\underset{\sim}{P}$ (64). Hence

$$\underset{\sim}{D} = \epsilon_o \underset{\sim}{E} + \underset{\sim}{P} \qquad 2.33$$

in which $\underset{\sim}{E}$ is the electric field strength and ϵ_o is the dielectric constant of vacuum. The electric dipole moment $\underset{\sim}{P}$ established under the influence of the field is proportional to the effective field $\underset{\sim}{E}'$

$$\underset{\sim}{P} = \alpha \underset{\sim}{E}' \qquad 2.34$$

where α is known as the polarizability.

In an anisotropic material

$$D_k = \sum_{\ell} \epsilon_{k\ell} E_\ell \qquad 2.35$$

$$P_k = \sum_{\ell} \alpha_{k\ell} E'_\ell \qquad 2.36$$

where ϵ_{kl} is the dielectric tensor and α_{kl} is the polarizability tensor. ϵ_{kl} and α_{kl} generally are coaxial for polymer.

By assuming fibre symmetry, the polymer is considered to be an aggregate of polarizable units with transverse isotropy. Each unit is defined by the second order polarizability tensor as

$$a_{k\ell} = \sum_{m} \sum_{n} \ell_{km} \ell_{\ell n} a_{mn} \qquad 2.37$$

In the chain axis coordinates

$$\underset{\sim}{a} = \begin{vmatrix} a_1 & 0 & 0 \\ 0 & a_2 & 0 \\ 0 & 0 & a_2 \end{vmatrix} \qquad 2.38$$

in which l_{km} and l_{lm} are the directional cosines, and α_1 and α_2 are polarizability along and perpendicular to the polymer chain. If $\alpha_{//}$ and $\alpha_{\perp}$ are taken as the average polarizabilities parallel and perpendicular to the fiber axis;

$$\begin{aligned} \alpha_{//} &= \alpha_1 \cos\phi_{1,//} + 2\alpha_2 \cos\phi_{2,//} \\ \alpha_{\perp} &= \alpha_1 \cos\phi_{1,\perp} + 2\alpha_2 \cos\phi_{2,\perp} \end{aligned} \qquad 2.39$$

Since the principal axes are orthogonal,

$$\begin{aligned} \cos^2\phi_{2,//} &= \tfrac{1}{2}(1-\cos\phi_{1,//}) \\ \cos^2\phi_{2,\perp} &= \tfrac{1}{2}(1-\cos\phi_{1,\perp}) \\ \cos^2\phi_{1,\perp} &= \tfrac{1}{2}(1-\cos\phi_{1,//}) \end{aligned} \qquad 2.40$$

Then

$$\begin{aligned} \overline{a_{//}-a_{\perp}} &= (a_1-a_2)(\cos^2\phi_{1,//}-\cos^2\phi_{1,\perp}) \\ &= (a_1-a_2)\left(\frac{3\cos^2\phi_{1,//}-1}{2}\right) \end{aligned} \qquad 2.41$$

Eq 2.41 leads to the definition of Hermans orientation function (26) as

$$f_H = \frac{\overline{a_{//}-a_{\perp}}}{a_1-a_2} = \tfrac{1}{2}(3\overline{\cos^2\phi}-1) \qquad 2.42$$

It was argued by Hermans et. al. (26) that this is equivalent to $f_H = \Delta n/\Delta^\circ$, where Δn is the birefringence which is the difference between the principal refractive index parallel to the stretch direction, $n_{//}$, and the principal refractive index perpendicular to it, $n_\perp$, for an oriented specimen, i.e. $\Delta n = n_{//} - n_\perp$, and $\phi = \theta_{1,//}$ is the angle between the molecular axis and the fiber axis, and $\Delta^\circ = (2/9)\pi\left[(n^2+2)^2/\bar{n}\right](\alpha_1 - \alpha_2)$ in which $\bar{n}$ is the average of $n_{//}$ and $n_\perp$ and Δ° is the maximum or intrinsic birefringence of the system at full orientation when $\overline{\cos^2\phi} = 1$.

For crystalline filaments Stein defined orientation factors with respect to all three crystallographic axes. These are called Hermans-Stein uniaxial orientation factors given by

$$f_j = \frac{1}{2}\left(3\overline{\cos^2\phi_{j,1}} - 1\right) \qquad 2.43$$

where $\overline{\cos\phi_{j,1}}$ is the average value of the cosine squared of the angle between the fiber axis and the j-crystallographic axis (j = a,b,c). The f_j factors are determined from wide angle x-ray diffraction experiment. Specifically

$$\overline{\cos^2\phi_{j,1}} = \frac{\int_0^{\frac{\pi}{2}} I_{hkl}(\phi_{j,1})\cos^2\phi_{j,1}\sin^2\phi_{j,1}\,d\phi_{j,1}}{\int_0^{\frac{\pi}{2}} I_{hkl}(\phi_{j,1})\sin\phi_{j,1}\,d\phi_{j,1}} \qquad 2.44$$

where $I_{hkl}(\phi_{j,1})$ is the intensity diffracted from the (hkl) planes which are normal to the j-crystallographic axis.

From the above equation it can be seen that the orientation function for a given crystal axis has a value of +1 for parallel

orientation, a value of 0 for random orientation and -1/2 for the perpendicular orientation with respect to the stretch direction. These are illustrated in Figure 2.3.

For crystals with orthogonal axes,

$$\overline{\cos^2\phi_{c,1}} + \overline{\cos^2\phi_{b,1}} + \overline{\cos^2\phi_{a,1}} = 1 \qquad 2.45$$

and

$$f_c + f_b + f_a = 0 \qquad 2.46$$

The Hermans-Stein orientation factors as defined above refer only to the crystalline phase. The total birefringence, Δn, is related to both the crystalline and the amorphous birefringence through

$$\Delta n = X\Delta^{oc} f_c + (1-X)\Delta^{oa} f_{am} + \Delta n_{form} \qquad 2.47$$

where X is crystallinity, f_c and f_{am} are the Hermans orientation factor of the crystalline and amorphous phases, Δ^{oc} and Δ^{oa} are intrinsic birefringence of fully oriented crystalline and amorphous material. Values of Δ^{oc} and Δ^{oa} for polyethylene and polystyrene developed in the literature are listed in Table 2.1.

Stein (79) was the first to be concerned with biaxial orientation. He defined biaxial orientation factors given by

$$f_{2j} = \overline{2\cos^2\delta_j} - 1 \qquad 2.48$$

where j is crystallographic axis (j = a,b,c) and Stein's angle δ_j is the Eulerian longitude angle between the crystallographic axis and an axis in the plane of the film. The range of values of Stein's biaxial orientation factor is +1 to -1 for each given crystal axis. When all the axes lie in the plane of the film it gives a value of +1, a value of 0 means axis random with respect to the plane of film (uniaxial) and a value of -1 indicates that axis lies in the plane perpendicular to

$$f_c = \frac{3\overline{\cos^2\phi_{1c}} - 1}{2}$$

CHAINS PARALLEL TO 1 $f_c = 1$

RANDOM ORIENTATION $f_c = 0$

CHAINS PERPENDICULAR TO 1 $f_c = -1/2$

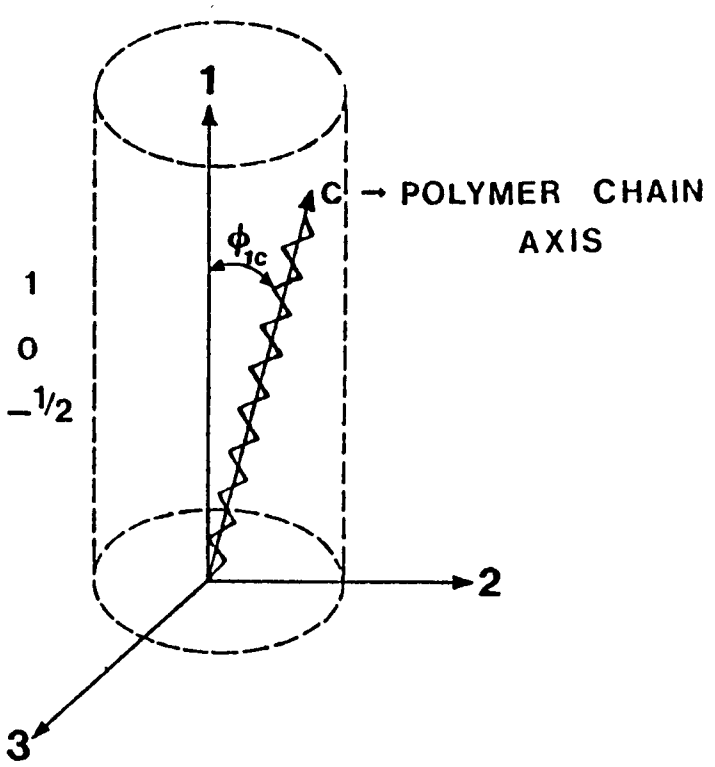

Figure 2.3 Uniaxial orientation illustration and a range of values of Hermans-Stein uniaxial orientation factors.

Table 2.1 Values of Intrinsic Birefringences of Fully Oriented Crystalline and Amorphous for PE and PS in the Literature.

Material	Δ^{oc}	Δ^{oa}
Polystyrene (PS)		-0.03 (18)
		-0.012 (53)
		-0.01246 (42)
Polyethylene (PE)	0.0572 (81)	0.030 (81)
	0.058 (6)	
	0.062 (46)	

the plane of film. Stein also derived the crystal contribution to the birefringence for an orthorhombic unit cell in terms of the biaxial orientation factors as

$$\Delta n_{13} = \frac{1}{2}\left\{\Delta n_{ac} f_a + \frac{f_{2a}(1-f_a)}{3} + \Delta n_{bc}\left[f_b + \frac{f_{2b}(1-f_b)}{3}\right]\right\}$$

$$\Delta n_{23} = \frac{2}{3}\left\{\Delta n_{ac}(1-f_a) f_{2a} + \Delta n_{bc}(1-f_a) f_{2b}\right\} \qquad 2.49$$

where f_a , f_b are uniaxial orientation factors for crystallographic a and b axes, respectively.

Nomura et al.(58) defined two orientation functions. The first of these is the same function as Hermans-Stein uniaxial orientation function but the second function which differs from Stein's mentioned above is defined by

$$f_{22}^{I} = \overline{\sin^2\phi \cos^2\delta} \qquad 2.50$$

White and Spruiell (90) proposed biaxial orientation factors based upon the anisotropy of the polarizability tensors. They use the angles between the chain and crystallographic axes ,and the machine and transverse directions rather than Euler's angles. For the chain orientation they obtain

$$f_1^B = 2\overline{\cos^2\phi_{c1}} + \overline{\cos^2\phi_{c2}} - 1$$

$$f_2^B = 2\overline{\cos^2\phi_{c2}} + \overline{\cos^2\phi_{c1}} - 1 \qquad 2.51$$

where subscript 'c' is chain direction while subscripts 1 and 2 refer to the reference directions (eg. machine and transverse directions, respectively). For the case of an orthorhombic crystal these orientation factors take the form where all three crystallographic axes are considered.

a-axis

$$f_1^B = 2\overline{\cos^2\phi_{a1}} + \overline{\cos^2\phi_{a2}} - 1$$
$$f_2^B = 2\overline{\cos^2\phi_{a2}} + \overline{\cos^2\phi_{a1}} - 1 \qquad 2.52$$

b-axis

$$f_1^B = 2\overline{\cos^2\phi_{b1}} + \overline{\cos^2\phi_{b2}} - 1$$
$$f_2^B = 2\overline{\cos^2\phi_{b2}} + \overline{\cos^2\phi_{b1}} - 1 \qquad 2.53$$

c-axis

$$f_1^B = 2\overline{\cos^2\phi_{c1}} + \overline{\cos^2\phi_{c2}} - 1$$
$$f_2^B = 2\overline{\cos^2\phi_{c2}} + \overline{\cos^2\phi_{c1}} - 1 \qquad 2.54$$

where subscript 'a', 'b'and 'c' refer to the crystallographic axis a, b and c. Only four are independent since

$$\overline{\cos^2\phi_{a1}} + \overline{\cos^2\phi_{b1}} + \overline{\cos^2\phi_{c1}} = 1$$
$$\overline{\cos^2\phi_{b1}} + \overline{\cos^2\phi_{b2}} + \overline{\cos^2\phi_{b3}} = 1 \qquad 2.55$$

These orientation factors have the range of values from 1 to -1 as shown in Table 2.2, and Figure 2.4. The special cases of isotropy (orientation factors zero), three different types of uniaxial orientation, and planar orientation are considered. Note that in the uniaxial case the orientation factors reduce to the well known Hermans' orientation factor. For planar orientations f_1^B and f_2^B may vary from 0 to 1. As macromolecules tend toward orientation parallel to the film normal f_1^B and f_2^B become negative. Their orientation distribution function triangle diagram proposed is shown in Figure 2.5.

They also derived the total birefringences Δn_{13} and Δn_{23} for amorphous polymers as

$$\Delta n_{13} = \Delta^{oa} f_1^B$$
$$\Delta n_{23} = \Delta^{oa} f_2^B \qquad 2.56$$

Table 2.2 White and Spruiell's Biaxial Orientation for Different Types of Orientation in a Film*.

Orientation	f_1^B	f_2^B
Isotropic	0	0
Uniaxial Machine Direction	$\frac{3\cos^2\phi_{c1}-1}{2}$	0
Chains Parallel to MD	+1	0
Uniaxial Transverse Direction	0	$\frac{3\cos^2\phi_{c2}-1}{2}$
Chains Parallel to TD	0	+1
Equal Biaxial (Planar or Non-Planar) (Same as Uniaxial Normal Direction)	$\frac{1-3\cos^2\phi_{c3}}{2}$	$\frac{1-3\cos^2\phi_{c3}}{2}$
Chains Parallel to ND	-1	-1
Planar	$\cos^2\phi_{c1}$	$\cos^2\phi_{c2}$
Planar Equal Biaxial	+1/2	+1/2
Planar Equidirection (Random about ND)	+1/2	+1/2

*$\cos^2\phi_{c1} + \cos^2\phi_{c2} + \cos^2\phi_{c3} = 1.0$

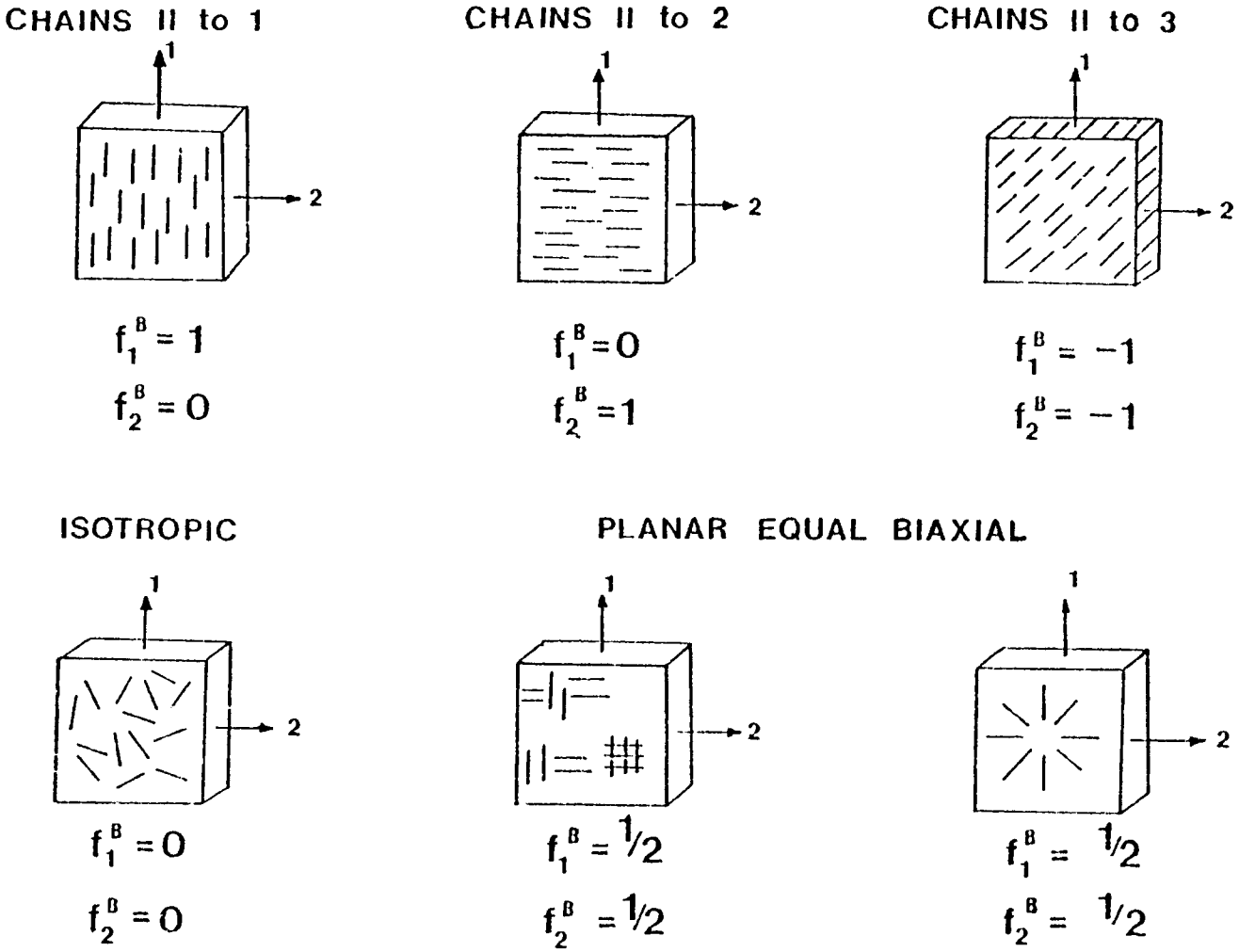

Figure 2.4 Different states of orientation in films and White and Spruiell's biaxial orientation factors.

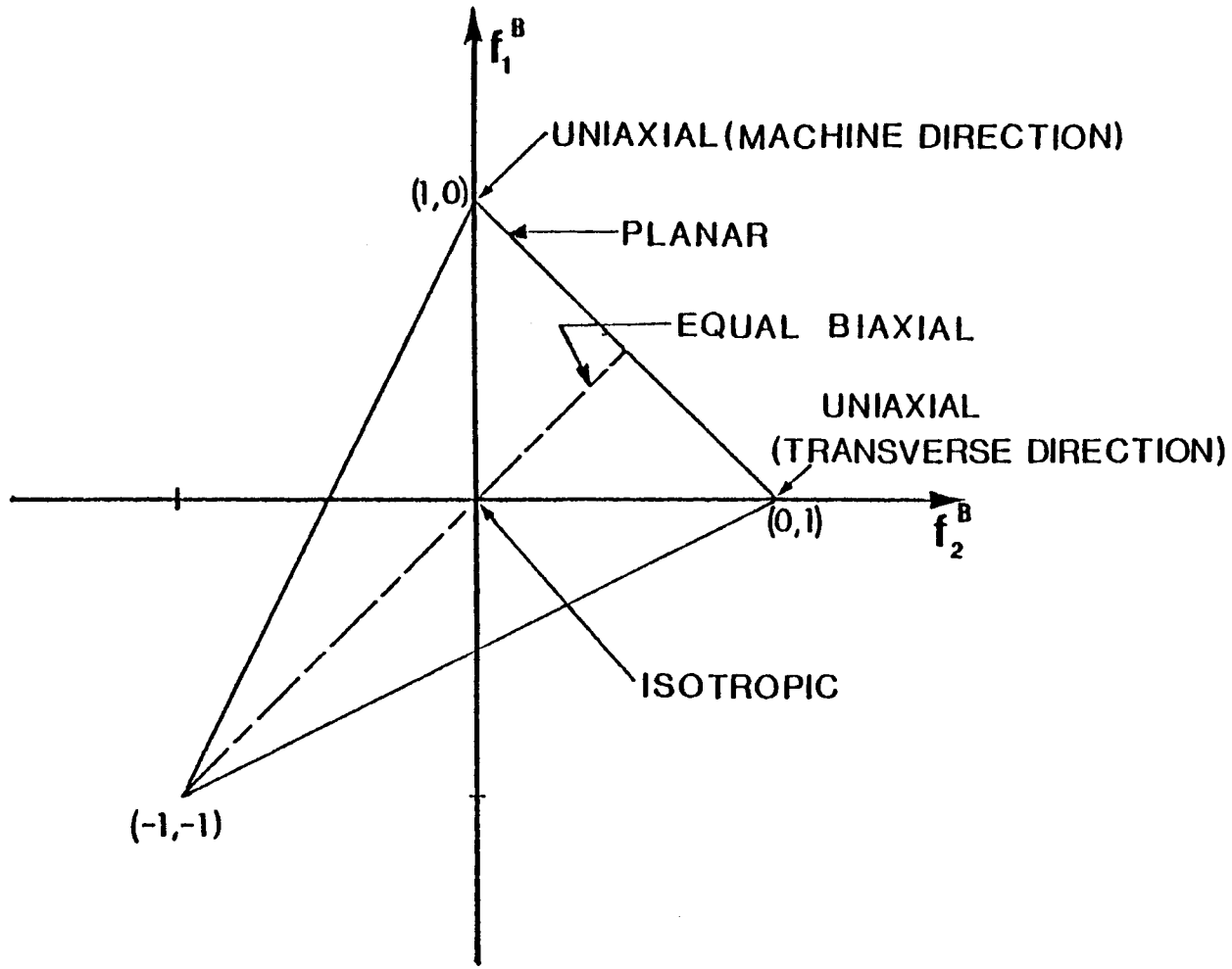

Figure 2.5 Graphical representation of orientation, the orientation triangle diagram (White and Spruiell).

For two-phase semicrystalline polymers

$$\Delta n_{13} = X\left[\Delta^{oc}_{ca}\ f^{B}_{1c} + \Delta^{oc}_{ba}\ f^{B}_{1b}\right] + (1-X)\left[\Delta^{oa}\ f^{B}_{1}\right] + \Delta n_{form}$$
$$\Delta n_{23} = X\left[\Delta^{oc}_{ca}\ f^{B}_{2c} + \Delta^{oc}_{ba}\ f^{B}_{2b}\right] + (1-X)\left[\Delta^{oa}\ f^{B}_{2}\right] + \Delta n_{form} \qquad 2.57$$

where X = volume fraction crystallinity, Δ^{oa} = intrinsic crystallite birefringence ($\Delta^{oc}_{ca} = n_c - n_a$, $\Delta^{oc}_{ba} = n_b - n_a$), Δ^{oa} = intrinsic amorphous birefringence and Δn_{form} = form birefringence.

Other methods for the representation of orientation functions in terms of spherical harmonic functions are the Legendre polynomials by means of Eulerilan angles θ, ψ, and ϕ. This has been done by Muller (54), Roe and Krigbaum (73, 74), Roe (74,75), Nomura et al. (58~61) and McBrierty and Ward (48).

The basic idea is the expansion of the orientation distribution in terms of Legendre polynomials given by (75)

$$\mathcal{W}(\xi,\psi,\phi) = \sum_{\ell=0}^{\infty}\sum_{m=-\ell}^{\ell}\sum_{n=-\ell}^{\ell} \mathcal{W}_{\ell mn}\ Z_{\ell mn}(\xi)\, e^{-im\psi} e^{-in\phi} \qquad 2.58$$

where $\mathcal{W}(\xi,\psi,\phi)$ is the orientation distribution function of all crystallites on the sample in which

$$\xi = \cos\theta \qquad 2.59$$

and

$$\int_0^{2\pi}\int_0^{2\pi}\int_{-1}^{1} \mathcal{W}(\xi,\psi,\phi)\, d\xi\, d\psi\, d\phi = 1 \qquad 2.60$$

For the special case of uniaxial orientation, the expansion in Legendre polynomials gives (48)

$$\rho(\phi) = \sum_{n=0}^{\infty} (n+\tfrac{1}{2})\ \overline{P_n(\cos\theta)}\ P_n\cos\theta \qquad 2.61$$

where $\rho(\phi)$ is the distribution function with

$$\overline{P_n(\cos\phi)} = \int_0^{\pi} \rho(\phi)\ P_n\cos(\phi)\sin\phi\, d\phi \qquad 2.62$$

i.e.

$$P_2(\cos\phi) = 1/2(3\cos^2\phi - 1)$$
$$P_4(\cos\phi) = 1/8(35\cos^4\phi - 30\cos^2\phi + 3) \qquad 2.63$$

This method has been applied by McBrierty and Ward (48) to NMR absorption curve and by Roe and Krigbaum (73, 74) to inverse pole transformation on stereographic charts.

2.8 EXPERIMENTAL METHODS FOR INVESTIGATION OF CRYSTALLINE ORIENTATION AND MORPHOLOGY

The most useful methods of investigating the structure and morphology of crystalline polymer film are diffraction techniques. Wide angle x-ray scattering (WAXS) yields crystallographic structure and orientation, and small angle x-ray scattering (SAXS) gives information on the order of a large scale ($\sim$100A). Light scattering yields information on the spherulitic structure. Polarized light can be used on thin films to determine birefringence which yields information on orientation. Surface characteristics can be studied by transmission electron microscope (TEM) and scanning electron microscope (SEM).

WAXS patterns are important in the characterization of polymer structure. Crystallinity can be determined from the relative intensities of the amorphous and crystalline contributions. From the azimutal intensity of the (Debye) rings a pinhole pattern one can calculate the amount of the molecullar orientation present in the crystalline polymer.

The pole figure is one of the important tools to interprete crystalline orientation and morphology in both quantitative and qualitative way. It gives the distribution in space of a given crystal plane normal, which is called a pole, or poles of a given set of planes. The experimental schematic of a goniometer for orienting a sample in the x-ray beam and its corresponding spherical coordinates ϕ and α are shown in Figure 2.6 and Figure 2.7 respectively.

Experimental values of $\overline{\cos^2\phi}$ needed for the computation of orientation functions as outlined in the preceeding section can be determined by averaging $\overline{\cos^2\phi}$ over the entire surface of the coordinate sphere. If ϕ is the angle between a chosen crystallographic direction and a reference direction, this average is expressed mathematically by the following equation (92).

$$\overline{\cos^2\phi} = \frac{\int_0^{\pi}\int_0^{2\pi} I(\phi,\alpha)\cos^2\phi\sin\phi\,d\alpha\,d\phi}{\int_0^{\pi}\int_0^{2\pi} I(\phi,\alpha)\sin\phi\,d\alpha\,d\phi} \qquad 2.64$$

where $I(\phi,\alpha)$ is the x-ray intensity diffracted from planes perpendicular to the chosen crystallographic direction. This intensity is proportional to the pole concentration representing the relative amount of crystalline material having plane normals in the direction ϕ , α. Note that we may write

$$I(\phi) = \int_0^{2\pi} I(\phi,\alpha)\,d\alpha \qquad 2.65$$

then

$$\overline{\cos^2\phi} = \frac{\int_0^{\pi} I(\phi)\cos^2\phi\sin^2\phi\,d\phi}{\int_0^{\pi} I(\phi)\sin\phi\,d\phi} \qquad 2.66$$

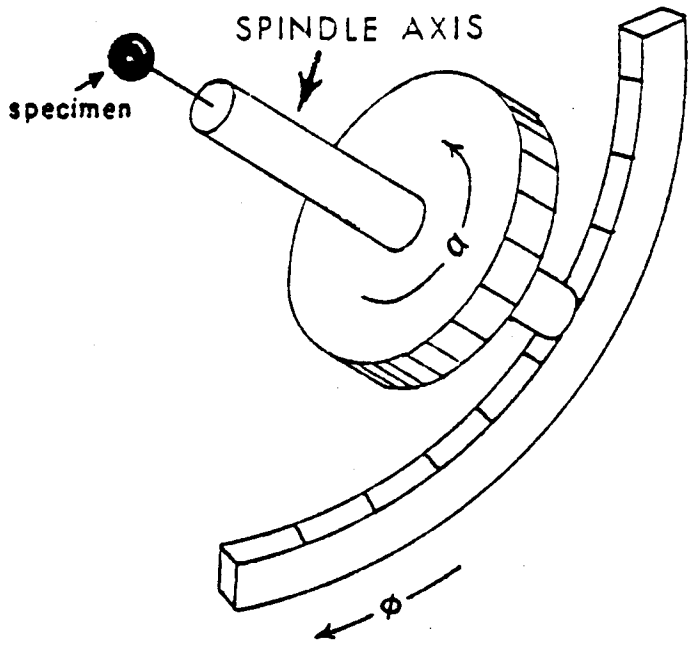

Figure 2.6 Experimental schematic of a goniometer for orienting a sample in the x-ray beam.

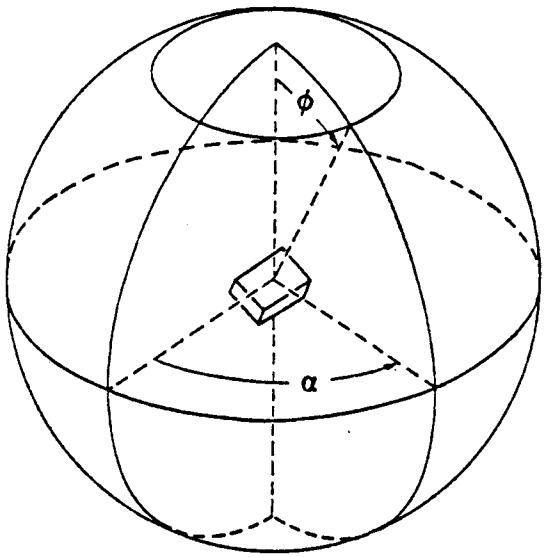

Figure 2.7 Position of plane normal by spherical coordinates.

2.9 ORIENTATION DEVELOPMENT IN VITRIFYING MELTS

Various investigators studying polyethylene terephthalate (PET) (19, 20, 93), polystyrene (22, 45, 62, 88) and high impact polystyrene (63) have shown that the frozen-in birefringence is determined by the orientation present in the melt. Studies of melt spun vitrified polystyrene filaments sheared and uniaxially stretched have been reported by various investigators. Oda, White, and Clark (62) show that the birefringence in the filaments is proportional to the difference in principal stress in the samples at the point of vitrification and that the coefficient is the melt phase stress-optical coefficient. The reported values of the stress-optical coefficient, C , for polystyrene are 4.1×10^{-10} cm²/dyne by Wales (88), 4.95×10^{-10} cm² /dyne by Han and Drexler (22), 6.1×10^{-10} cm²/dyne by Matsumoto and Bogue and 4.5×10^{-10} cm² /dyne by Oda, White and Clark, and for polyethylene terephthalate are 7.8×10^{-10} cm²/dyne by Hamana (19) and 6.55×10^{-10} cm²/dyne by Yasuda et.al. (93). Omotoso, White and Fellers (63) find 'C' of high impact polystyrene to be 4.5×10^{-10} cm²/dyne which is the same as for polystyrene.

When Eq 2.31, page 14, was verified for vitrified polystyrene by Oda, White and Clark (62),they proposed Eq 2.31 as a general method of prediction of orientation distributions in fabricated polystyrene parts. This concept has been used to predict birefringence distributions injection molded parts by Dietz, White and Clark (13) and Janeschitz-Kriegl (29).

White and Dietz (89) have specifically proposed applying this approach to tubular film extrusion. According to them, the two principal birefringences of the film at various positions along the tube may be taken as

$$\Delta n_{12}=\frac{C}{2\pi r h\cos\theta}\left[F_L\left(1+\frac{R_H}{R_M}\right)-\Delta P\left[2\pi r R_H\cos\theta+\pi(R_L^2-r^2)\right]\left(1+\frac{R_H}{R_M}\right)\right]$$
$$\Delta n_{13}=\frac{C}{2\pi r h\cos\theta}\left[F_L-\pi\Delta P\left(R_L^2-r^2\right)\right] \qquad 2.67$$

where $\Delta n_{12} = n_1 - n_2$, $\Delta n_{13} = n_1 - n_3$ in whch two of principal axes of the refractive index ellipsoid are in the '1' and '2' direction, and the third is perpendicular to the sheet. Here it is assumed that the two principal stresses are

$$\sigma_{11}=\frac{F_L-\pi\Delta P(R_L^2-r^2)}{2\pi r h\cos\theta}$$
$$\sigma_{22}=\frac{R_H}{R_M}\left(\frac{2\pi r R_M\cos\theta+\pi\Delta P(R_L^2-r^2)-F_L}{2\pi r h\cos\theta}\right) \qquad 2.68$$

At the point of vitrification

$$\Delta n_{12}\rightarrow C\left(\frac{F_L}{2\pi R_L h}-\frac{R_L\Delta P}{h}\right)\rightarrow C(\sigma_{11}-\sigma_{22})$$
$$\Delta n_{13}\rightarrow C\frac{F_L}{2\pi R_L h}\rightarrow C\sigma_{11} \qquad 2.69$$

For the equal biaxially oriented film

$$\Delta n_{12}=0 \quad , \quad \Delta P=\frac{F_L}{2\pi R_L^2} \qquad 2.70$$

For the uniaxially oriented film

$$\Delta n_{12} = \Delta n_{13} \quad , \quad \Delta P = 0 \qquad 2.71$$

Note that the birefringences are presumed to be those that are frozen into the film, but the take-up forces F_L and the internal pressure ΔP are measured on the running film line and hence represent the forces needed to deform the melt.

2.10 STRUCTURE DEVELOPMENT IN MELT SPINNING CRYSTALLINE POLYMER

The crystalline morphology and orientation of melt spun fiber has been studied as a function of processing condition by Keller (31), Ziabicki and Kedzierska (95), Kitao, Ohya, Furukawa and Yamashita (34) and by Spruiell and White and their co-workers (9, 55, 77).

On-line studies of structure development during melt spinning have been reported for high density polethylene by Katayama, Amano and Nakamura (30) and by Dees and Spruiell (9), using wide angle x-ray diffraction and birefringence (Katayama et al.). Polypropylene has been investigated in similar experiments by Katayama et al. (30), Nadella, Henson, Spruiell and White (55) and by Ishizuka and Koyama (28). The rate of crystallization was observed and found to increase rapidly with applied stress.

Crystalline orientation development was determined by these and other researchers and interpreted in terms of row structure models, i.e. a lamellar growth normal to the stress direction. Slight tendencies toward a-axis orientation were interpreted by Keller and Machin (33) and Dees and Spriuell (9) to be due to twisting of lamellae as they grow radially outward from the row nuclei. Tennessee investigators have also interpreted these structural changes in terms

of Hermans-Stein orientation factors (9, 55, 77). Basically increasing draw down was found to first orient the b-axis perpendicular to the fiber axis, c-axis orientation increases more slowly. At low draw down HDPE and LDPE some tendency to a-axis orientation is first observed but at higher draw downs increasing c-axis orientation is found. Polypropylene shows a lesser tendency to this type of a-axis orientation but shows striking development of bimodal orientation. SAXS measurements showed a 100 A repeat distance (32). Transmission electron microscope observations of surface replicas showed lamellar structure (35), this has led to the view that melt spun fibers consist of folded chain "row nucleated" lamellae which grow with their b-axis in the radial direction of the fiber (see figure on page 99). The lamellae tilt or twist about their b-axis especially for the case of polyethylene. Nadella et.al. (55) have shown the orientation factors in polypropylene depend upon spinning stress levels rather than kinematic variables.

2.11 STRUCTURE DEVELOPMENT STUDIES FOR TUBULAR FILM EXTRUSION

Film structural study of polyethylene related to blown film processing conditions (i.e. various blow-up ratios) was carried out by Holmes and Palmer with flat-plate x-ray diffraction and birefringence (27). They proposed row orientation in which the b-axis was oriented in the plane perpendicular to the extrusion direction and the a- and c-axes were randomly distributed with cylindrical symmetry about b-axis.

Lindenmeyer and Lustig (38) investigated crystallite orientation in HDPE and LDPE film using WAXS and constructed pole figures. At low blow ratio the orientation of the HDPE and LDPE were approximately the same. When the blow ratio was increased the LDPE film showed b-axis perpendicular to the film and a- and c-axes uniformly distributed in the plane of the film.

Clark and Garber (8) argued using TEM studies that polyoxymethylene blown film showed nucleating fibrils aligned in the extrusion direction with twisted bundles of lamellae oriented normal to the fibrils. They essentially observed row structure and void formation with increasing elongation percentage.

Nagasawa et al. (56) have made on line studies of birefringence in the tubular film extrusion of polymer melts under a blow-up ratio of 1. They also made extensive electron microscopic investigations of the film. They interpreted their results in terms of models similar to the shish kebab row structures of the type developed by Keller (31). They do not consider the infuluence of process variables other than tensile draw down.

Rohn (76) found for poly(butene-1) blown films that the applied stress on a polymer melt is directly proportional to the degree of orientation. He first showed the correlation between tensile break elongation and birefringence. Hence his measurements were tensile break elongation to get the degree of orientation, and the elongational viscosity of melts by tensile tester.

Recently Maddams and Preedy (41) have presented a series of papers about the orientation of HDPE blown film. They used pole figures to

characterize the orientation. Two types of orientation are described. One is a- and c-axes inclined at an angle to the plane of the film which was developed by Keller and Machin (33), the other type is c-axis distribution substantially along the machine direction and a- and b-axes rotated around c-axis which found in cold drawn polyethylene (49, 50). These types of orientation depend upon the blow-up ratio, draw down and cooling condition and sample. Some HDPE samples (MI = 12~13 and MI = 7.9) show always former type orientation and the latter type formed readily in the case of one HDPE samples (MI = 7.5) by slower cooling condition. They carried out extensive measurement for films from the latter sample (MI = 7.5). They conclude that under very low-stress conditions there was almost pure a-axis orientation; with very high stress there was substantial c-axis orientation, both with reference to the machine direction. Commercial blowing conditions gave rather high stress and the a-axis was inclined at 60° to 70° to the machine direction in the sheet-normal-direction plane. Also they found that a high draw down ratio and a low extrusion temperature were most effective in promoting high-stress crystallization. But they do not seem to have made any measurements of the actual stresses involved. Their representation of the a-axis orientation is shown in Figure 2.8.

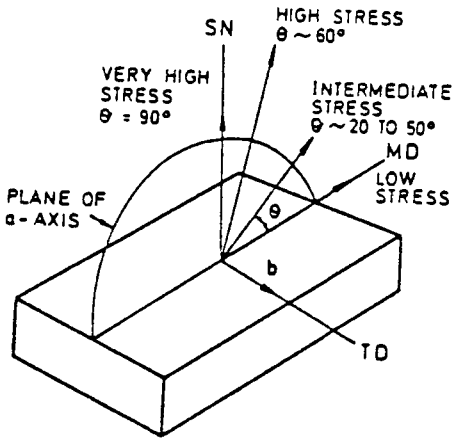

Figure 2.8 Representation of the a-axis orientation as a function of stress during the film blowing process (Maddams and Preedy 1978).

CHAPTER 3

MATERIAL AND EXPERIMENTAL PROCEDURES

3.1 MATERIALS

The polymers used in these experiments were a commercial polystyrene, Dow Styron 678U (MI = 12.0), similar to the polymer rheologically characterized in a series of studies from our laboratories (39, 83), and a commercial high density polyethylene, Chemplex® Polyethylene 6009 (MI = 0.98, density = 0.960). Extrusion temperatures were 180° C for polystyrene and 200° C for HDPE.

3.2 FILM EXTRUSION APPARATUS AND OPERATING PROCEDURE

The polystyrene and high density polyethylene films were produced using a 3/4 inch Rainville screw extruder with an annular blown film die (inside diameter = 1.496cm and outside diameter = 1.605cm). A sketch of the die is given in Figure 3.1.

The axial tension F_L of the film during processing was measured with a Tensitron web tension sensor. The pressure within the bubble was measured with a manometer through a tube connected to the die. The extrusion rate was measured by weighing the product for a predetermined time interval during steady state operation. A picture of the apparatus is shown in Figure 3.2.

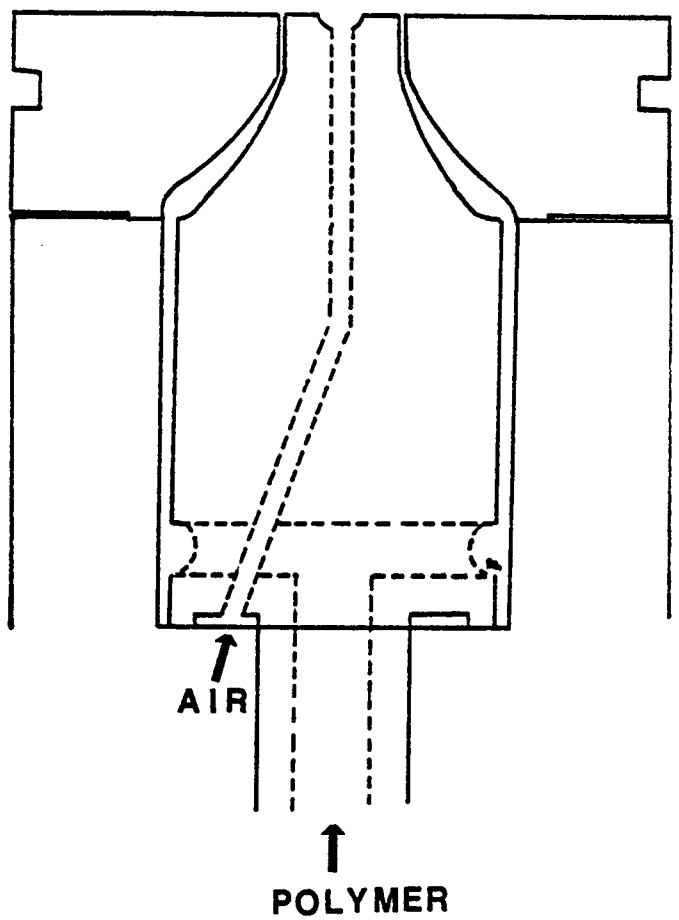

Figure 3.1 Schematic of the blown film die.

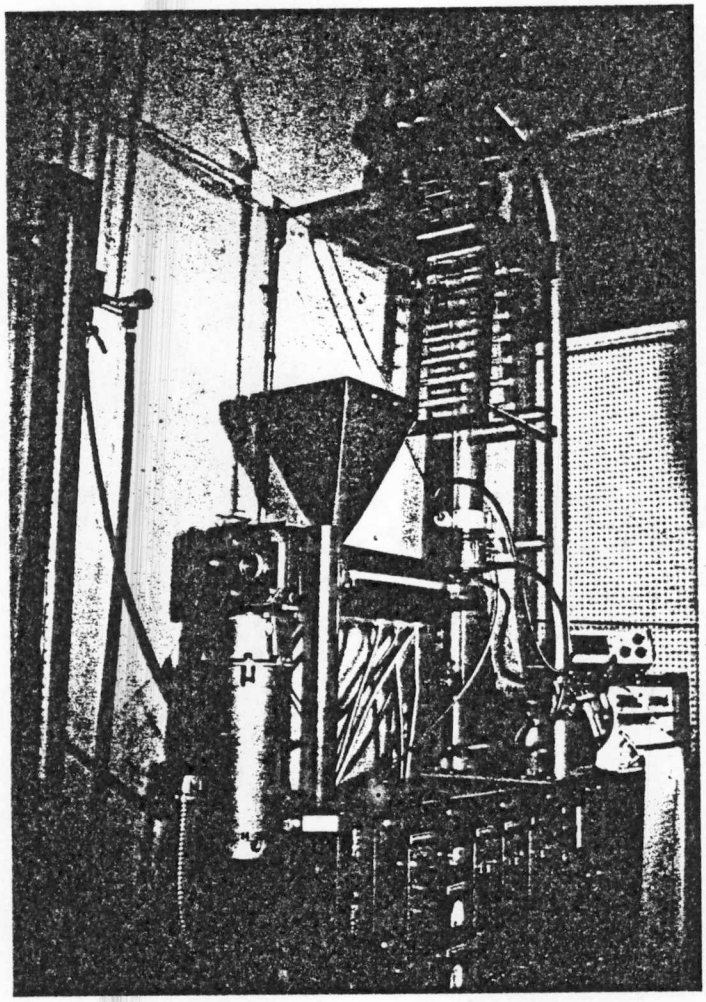

Figure 3.2 A blown film apparatus.

Two series of films were produced. The first series of samples was approximately uniaxial. The films in this series had drawdown ratios (v_L/v_o) in the range 46 to 130, labeled U1-U7, for PS and 5.2 to 16.4, labeled 1-3, for HDPE. A second series of films were made with an approximately constant blow-up ratio (B) of 2.5. These films had draw ratios in the range 33 to 60, labeled 1-5, for PS and 3.4 to 10.6, labeled 4-6, for HDPE. One film of each type was produced with blow-up ratio 6.2, labeled 'Bi' for PS and 7.94, labeled '8', for HDPE with equal biaxial extension according to Eq 2.20, page 10. One more HDPE film was made with B = 5 and v_L/v_o = 4.7, labeled '7'. Detailed summaries of the film prepared are presented in Table 3.1 for PS and Table 3.2 for HDPE.

3.3 CHARACTERIZATION OF THE BLOWN FILM

A. BIREFRINGENCE MEASUREMENTS

Both "in-plane" and "out-of-plane" birefringences were measured. The "in-plane" birefringence represents the difference of index of refraction between the machine and transverse directions, Δn_{12}, and the "out-of-plane" birefringence represents the difference in index of refraction between the machine and thickness directions, Δn_{13}. This was accomplished using an instrument equivalent to that of Stein (78) which allows a sample to be rotated and tilted in the incident polarized light beam. The governing equation given by Stein for obtaining the "out-of-plane"birefringence is

$$\Delta n_{13} = \frac{\lambda_o}{d_o}\left[\frac{R_\phi\left(1-\sin^2\phi/n^2\right)^{\frac{1}{2}} - R_o}{\sin^2\phi/n^2}\right] \qquad 3.1$$

Table 3.1 Polystyrene Films Prepared by Tubular Film Process.

Sample	V_L/V_0	h (micrometers)	B	F_L(N)	Δp(Pa)	σ_{11}(MPa)	σ_{22}(MPa)
U1	46	76.4	0.6	3.04	0	1.32	0
U2	61	40.6	0.76	3.07	0	1.98	0
U3	74	38.1	0.8	3.82	0	2.50	0
U4	79	28.0	0.84	4.00	0	3.39	0
U5	103	20.1	0.88	4.18	0	4.71	0
U6	117	16.0	0.92	4.67	0	6.32	0
U7	130	11.4	0.92	4.88	0	9.25	0
1	33	17.3	2.5	2.70	270	1.21	0.31
2	39	14.0	2.6	2.67	270	1.43	0.41
3	46	11.4	2.6	2.62	270	1.76	0.50
4	52	10.2	2.5	2.58	270	2.01	0.53
5	59	5.3	2.2	2.61	270	4.45	0.89
Bi	6.2	13.0	6.0	1.29	72	0.33	0.25

Table 3.2 HDPE Films Prepared by Tubular Film Process.

Sample		V_L/V_o	h(micrometers)	B	F_L(N)	Δp(Pa)	σ_{11}(MPa)	σ_{22}(MPa)
Uni	1	5.2	228	0.31	1.5	0	0.42	0
	2	10.0	148	0.23	1.3	0	0.62	0
	3	16.4	74.0	0.22	1.0	0	1.1	0
	4	3.4	44.5	2.2	1.5	160	0.34	0.066
	5	6.5	25.4	2.2	1.4	160	0.51	0.11
	6	10.6	13.3	2.3	1.2	160	0.80	0.22
	7	5.04	15.1	4.7	1.1 ± 0.3	63	0.32 ± 0.09	0.15
Bi:	8	7.94	5.1	9.8	1.2 ± 0.5	45	0.48 ± 0.20	0.68

where n is the average index of refraction of the film, λ_o is wave length of the light used in vacuum, d_o is the thickness of the film, R_o is the retardation of the film for normal incidence expressed in units of number of waves, and R_ϕ is the retardation of the film tilted through the angle ϕ. Example of the original data sheets used for polystyrene is shown in Table 3.3. The equipment is shown in Figure 3.3.

B. DENSITY DETERMINATION

The density of polyethylene was determined at 23° C using a distilled water-isopropyl alcohol density gradient column with a range of 0.9200 - 0.9700 g/cm^3. The samples were allowed to seek their level of displacement for approximately 8 hours.

The crystalline fraction was obtained through

$$X = \frac{\rho_c}{\rho} \frac{\rho - \rho_a}{\rho_c - \rho_a} \qquad 3.2$$

where X is the crystalline fraction, ρ_c is the crystalline density of polyethylene (ρ_c = 1.002), ρ_a is the amorphous density of PE (ρ_a = 0.855) and ρ is sample density measured.

C. SMALL ANGLE X-RAY SCATTERING (SAXS) PATTERNS

SAXS patterns were obtained using a modified Kiessig Camera with pinhole collimation. The camera was mounted on a Rigaku General Electric rotating anode x-ray generator. Air scattering was reduced by evacuating the camera with a mechanical pump. The sample to film distance was 40cm, the radiation was Cu-K_α and the range of the

Table 3.3 Original Data Sheet for Birefringence Measurement (PS).

Date		Temp.		Refractive Index of PS at 20° : $\bar{n}$=1.591	Thickness of Specimen : d_o= cm
		Humid.	%RH		
Specimen	PS (grade)	Uni( ) Bi ( )	σ_{11}= dynes/cm²	ΔP=	Y_L/Y_0= B= No.
Source of Light : white light, λ=565 mμ			Babinet Compensator		Rotation Axis =TD : TD ∥ ⊥ Comp.

φ°	Original ∥	Original ⊥	Original mean	Wave # ×1.031×10⁻⁵	Γ (cm)	$\frac{1}{\left(1-\frac{\sin^2\phi}{\bar{n}^2}\right)^{\frac{1}{2}}}$	d(cm)	$\Delta n_o = \Gamma/d$	$\Delta n_o - \Delta n_i$	$\frac{\sin^2\phi}{\bar{n}^2}$	Δn
0°						1.0000					
								$\Delta n_{12}^{\parallel}$			
20°						1.0240				0.04621	
25°						1.0373				0.07056	
30°						1.0534				0.09876	
35°						1.0721				0.1300	
40°						1.0932				0.1632	
45°						1.1162				0.1975	
										total	
										mean Δn_{31}	

Δn_{12}=-
Δn_{13}=-
$\Delta n_{32}=\Delta n_{12}-\Delta n_{13}$=

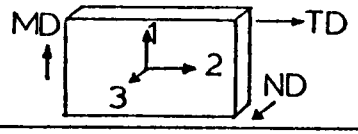

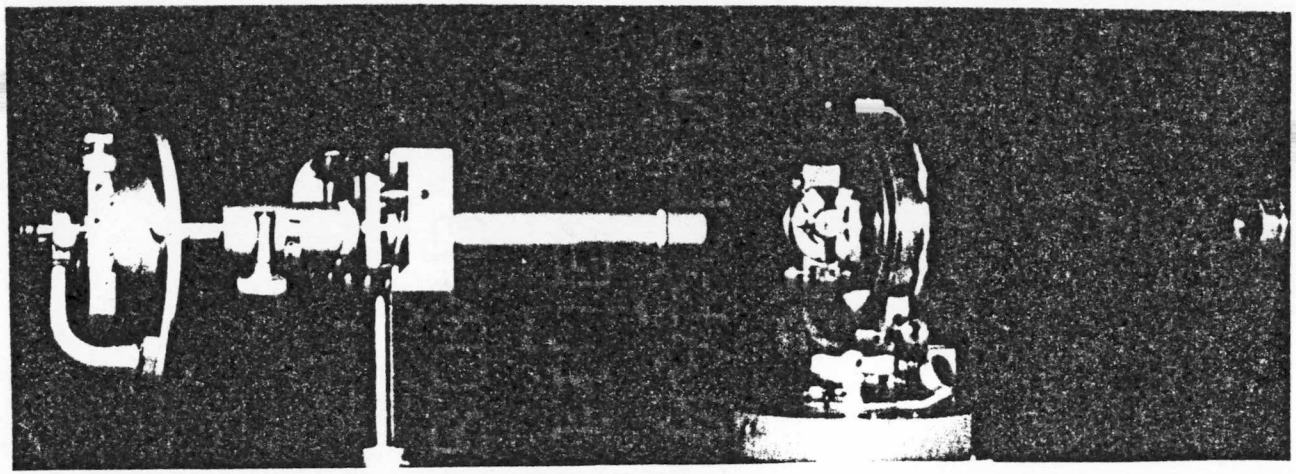

Figure 3.3 Polarizing microscope with a babinet compensator and rotating sample holder.

exposure times was from 2 hours to 10 hours.

D. X-RAY POLE FIGURE DETERMINATIONS

X-RAY DIFFRACTION EQUIPMENT; A General Electric manufactured x-ray diffractometer equipped with a single crystal orienter was used. The radiation used was crystal-monochromated Cu-Kα of wave length 1.542 Angstroms. The x-ray unit was operated at 40KV and 15MA. With the diffractometer set at a fixed angle, 2θ, for diffraction from a chosen set of diffraction planes, the sample could be tilted and rotated by the single crystal orienter in order to determine the function I(α , ϕ) needed for pole figure plotting or measurement of $\overline{\cos^2\phi}$ function.

SAMPLE PREPARATION AND INTENSITY CORRECTION; Sheets of the polyethylene blown film were carefully stacked parallel to the machine direction in a clamp. Epoxy glue was applied to the trimmed edges to hold the films together. During curing the films were pressed flat by a thick glass plate for several hours. Smaller samples used for x-ray diffraction were then cut from these original "sandwiches." These x-ray samples were about 1.5mm width each side. This sample was mounted on a polystyrene rod (see Figure 3.4) and placed in the single crystal orienter.

After the sample was aligned, 2θ scans were made at different α, ϕ angles for the purpose of determining the intensity correction and optimun setting 2θ value for the particular reflection for which the pole figure is to be determined. Here α and ϕ are the circumferential and radial angles of the pole with respect to Cartesian reference

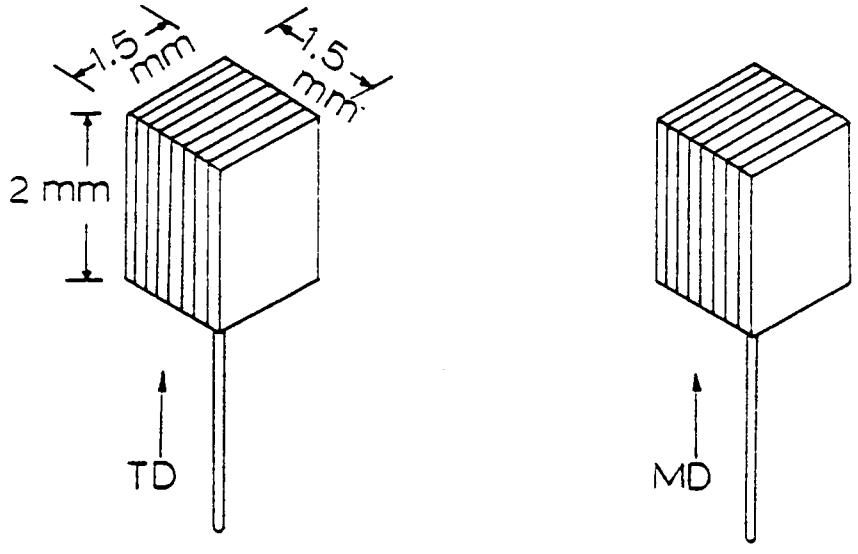

Figure 3.4 Samples used on the single crystal orienter with film packs.

coordinates (see figure on page 55).

The amorphous,(110) and (200) intensity data were corrected for overlap by the method of Nichols (57), and Aggarwal and Tilley (1), using several 2θ scans obtain at different α, ϕ angles.

The following assumptions were used

1. The back ground is linear between 2θ values of 14.36° and 26.00°.

2. The amorphous scattering has its maximum at $2\theta = 19.5^\circ$ and the maximum of diffracted x-ray intensity from (200) planes is at $2\theta = 23.65^\circ$.

3. The peaks are symmetrical about their respective maxima.

These assumptions allowed small correction for back ground and peak overlap to be determined and subtracted from the data for each reflection.

DATA RECORDING AND POLE FIGURE PLOTTING; The data recording was accomplished automatically using a digital equipment; PDP-15 computer, with appropriate programs programed by Prof. J. E. Spruiell. The detailed method for pole figure data acquisition involved an incremental (step) circular scan in which radial angle, ϕ, was set and circumferencial angle, α, was changed incrementally from 0° to 360°. This process was repeated for different radial angle, ϕ. The circular scan method is completely automated through an interface between the single crystal orienter and PDP-15 computer. Data recorded on Dec-tape and Dec-writer gave $\overline{\cos^2\phi}$ values at the same time. These data were then transfered to the disc of the DEC-10 of the university computer

system for plotting. The pole figure is plotted on the Textronix screen as well as on the plotter beside the Textronix terminal by the appropriate programs (see Appendix of reference 12).

E. EVALUATION OF ORIENTATION FUNCTIONS

The polyethylene crystal is orthorhombic with a = 7.41A, b = 4.94A and chain axis, c = 2.55A (82). This cell is shown in Figure 3.5 and its important poles are illustrated in Figure 3.6.

As mentioned in Chapter 2, four of the six cosine square averages, $\overline{\cos^2\phi_{a1}}$ $\overline{\cos^2\phi_{a2}}$ $\overline{\cos^2\phi_{b1}}$ $\overline{\cos^2\phi_{b2}}$ for polyethylene, must be measured.

Both $\overline{\cos^2\phi_{a1}}$ and $\overline{\cos^2\phi_{a2}}$ are obtained from the 200 pole figure through

$$\overline{\cos^2\phi_{a1}} = \frac{\sum_{\phi=0^\circ}^{180^\circ} I_{200}(\phi_1)\ \cos^2\phi_{200,1}\ \sin\phi_{200,1}}{\sum_{\phi=0^\circ}^{180^\circ} I_{200}(\phi_1)\ \sin\phi_{200,1}} \qquad 3.3$$

$$\overline{\cos^2\phi_{a2}} = \frac{\sum_{\phi=0^\circ}^{180^\circ} I_{200}(\phi_2)\ \cos^2\phi_{200,2}\ \sin\phi_{200,2}}{\sum_{\phi=0^\circ}^{180^\circ} I_{200}(\phi_2)\ \sin\phi_{200,2}}$$

where

$$I_{200}(\phi_1) = \sum_{a=0^\circ}^{360^\circ} I_{200}(\phi_1, a_1) \qquad 3.4$$

and

$$I_{200}(\phi_2) = \sum_{a=0^\circ}^{360^\circ} I_{200}(\phi_2, a_2)$$

In the same manner, $\overline{\cos^2\phi_{b1}}$ and $\overline{\cos^2\phi_{b2}}$ can be measured from the 020 pole distribution.

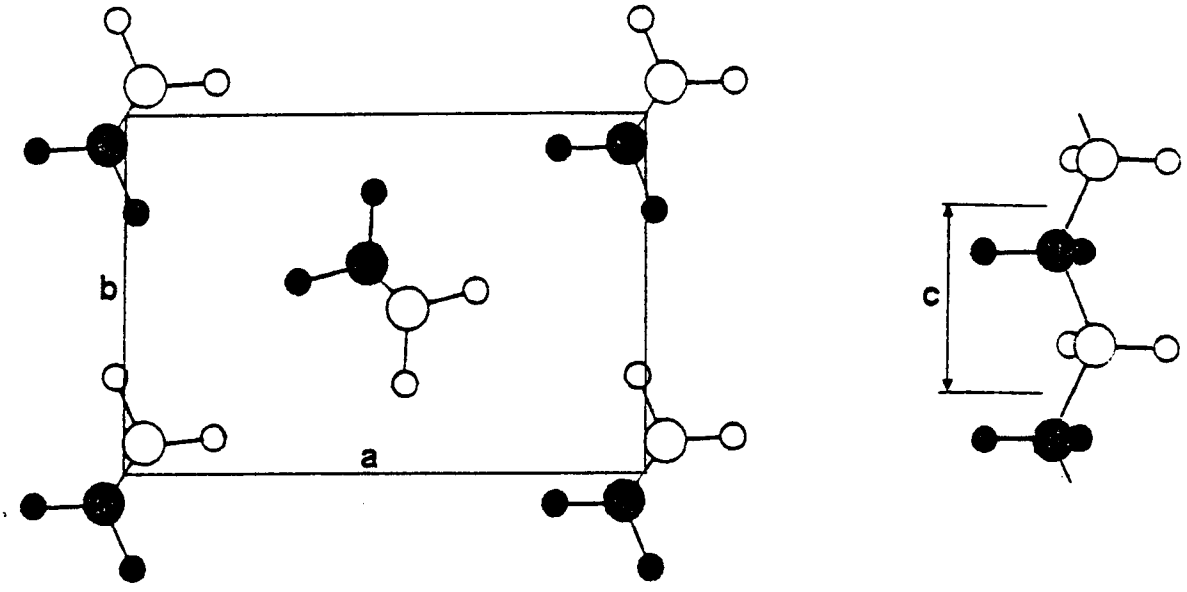

Figure 3.5 Projections of polyethylene unit cell.

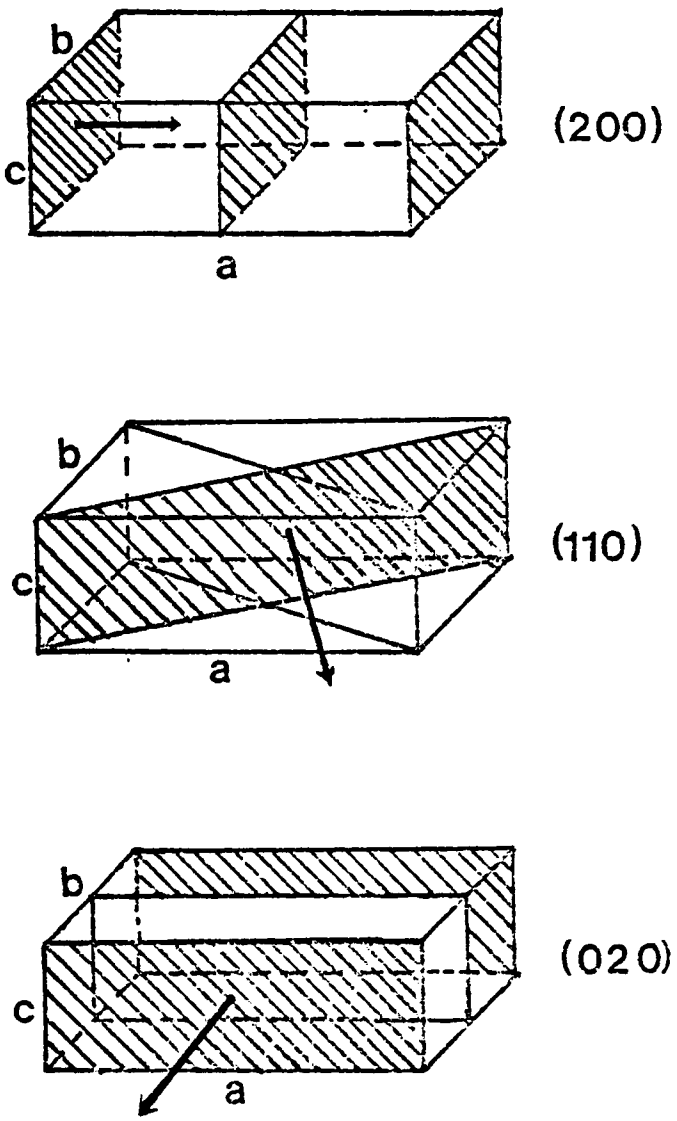

Figure 3.6 Graphical representation of 200, 110, and 020 poles of polyethylene.

Since the intensity of (020) is much weaker than that of (200) or (110), it is often preferable to obtain data from the 110 reflection rather than the 020 reflection. Following Wilchinsky's treatment, this leads to the following formula for evaluating $\overline{\cos^2\phi_{b1}}$ and $\overline{\cos^2\phi_{b2}}$ from the 200 and 110 pole distributions:

$$\overline{\cos^2\phi_{b1}} = \frac{\overline{\cos^2\phi_{110,1}} - 0.308\ \overline{\cos^2\phi_{a,1}}}{0.692} \qquad 3.5$$

$$\overline{\cos^2\phi_{b2}} = \frac{\overline{\cos^2\phi_{110,2}} - 0.308\ \overline{\cos^2\phi_{a,2}}}{0.692}$$

It was convenient to have two samples for the evaluation of cosine square averages. One sample had α-angle rotation axis as the transverse direction and gave $\overline{\cos^2\phi_{a2}}$ or $\overline{\cos^2\phi_{b2}}$ directly depending on the 2θ value for the reflecting plane. The other samples had α-angle rotation axis as the machine direction and gave $\overline{\cos^2\phi_{a1}}$ or $\overline{\cos^2\phi_{b1}}$ directly depending on 2θ value (see Figure 3.7).

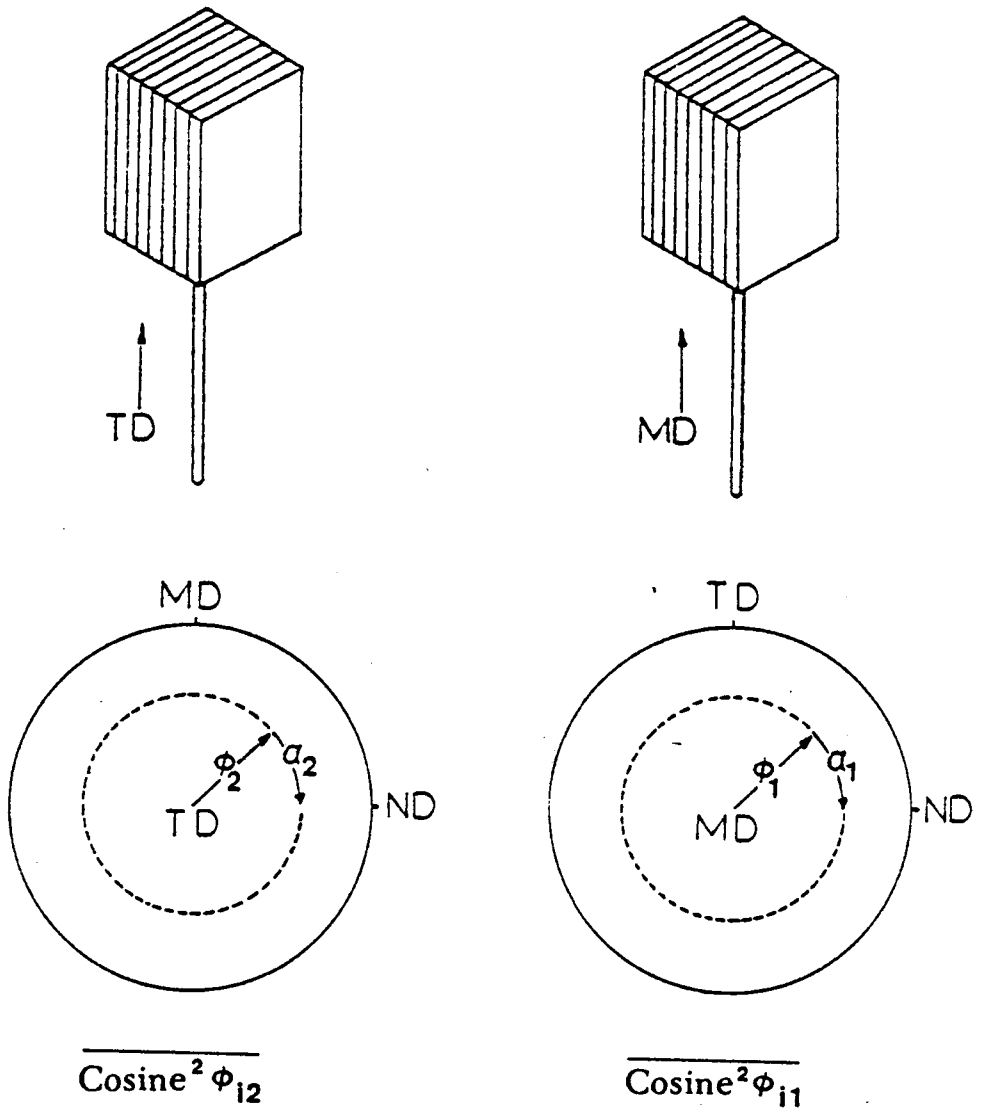

Figure 3.7 Experimental determination of $\overline{\cos^2\phi_{i2}}$ and $\overline{\cos^2\phi_{i1}}$.

CHAPTER 4

EXPERIMENTAL RESULTS AND DISCUSSION

4.1 AMORPHOUS POLYMER (POLYSTYRENE)

A. RESULTS

Here again '1', '2' and '3' are the machine direction, the transverse or circumferential direction and the normal or thickness direction respectively, and $\Delta n_{ij} = n_i - n_j$.

Figures 4.1 and 4.2 are plots of the birefringences Δn_{12}, Δn_{13} and Δn_{23} as a function of drawdown ratio v_L / v_o for the uniaxial and constant blow-up ratio series samples.

For the approximately uniaxial case

$$\Delta n_{13} \sim \Delta n_{12} < 0 \qquad 4.1$$

and

$$\Delta n_{23} \sim 0 \qquad 4.2$$

with the magnitude of Δn_{13} increasing with drawdown.

Data for the constant blow-up ratio series (B~2.5) are labeled 1 through 5 in Figure 4.2. Here

$$\Delta n_{12} < 0 \qquad \Delta n_{13} < 0 \qquad \Delta n_{23} < 0 \qquad 4.3$$

$$|\Delta n_{13}| > |\Delta n_{23}| \text{ or } |\Delta n_{12}| \qquad 4.4$$

Birefringences Δn_{12} and Δn_{13} increase with drawdown ratio.

For the biaxial film

$$|\Delta n_{12}| \sim 0.25 \times 10^{-3} \qquad \Delta n_{13} \sim \Delta n_{23} \qquad 4.5$$

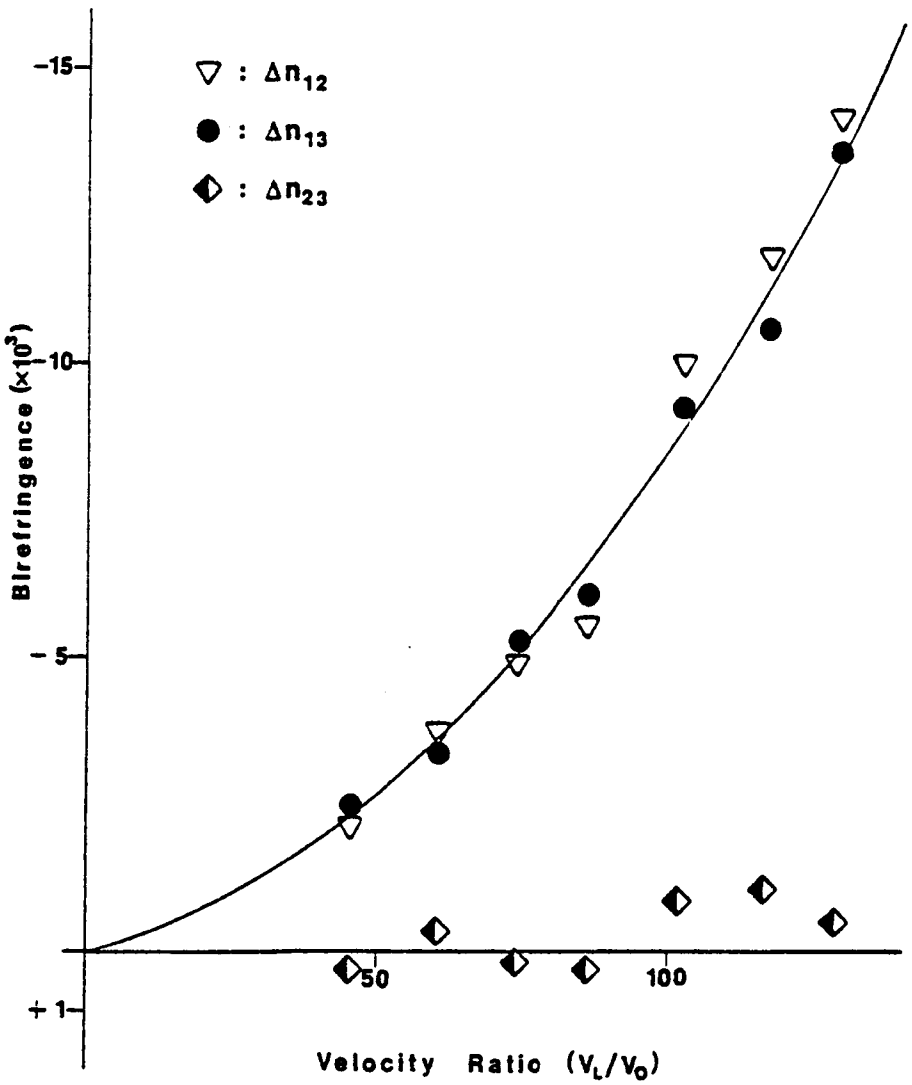

Figure 4.1 Birefringence of polystyrene tubular film as a function of drawdown condition-uniaxial.

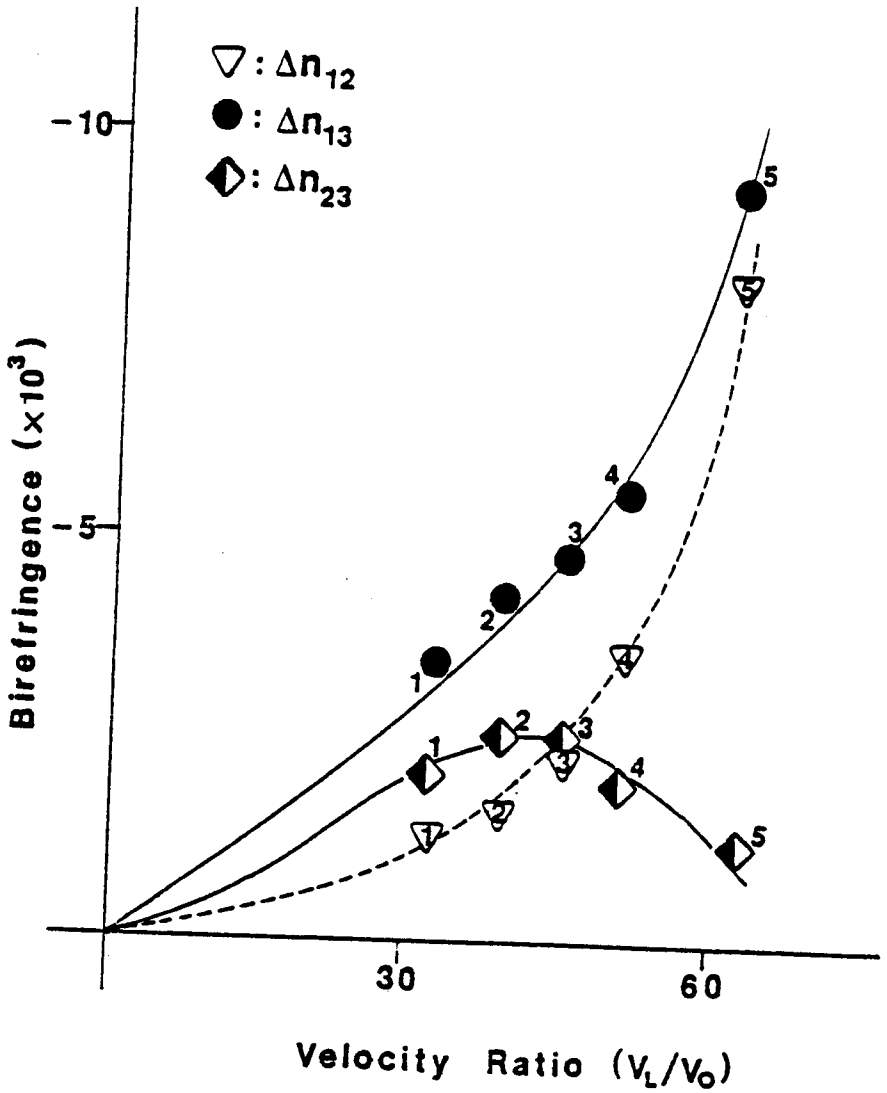

Figure 4.2 Birefringence of polystyrene tubular film as a function of drawdown for B~2.5.

Following the procedure of Oda, White and Clark the birefringences Δn_{ij} are plotted as a function of $\sigma_i - \sigma_j$, the difference in principal stresses at the line of vitrification in Figure 4.3. The principal stresses σ_1, σ_2 and σ_3 at this line in tubular film extrusion are σ_{11} and σ_{22} given by Eq 2.69, page 33, and σ_{33} taken as zero.

The Δn_{ij} and $(\sigma_i - \sigma_j)$ data correlate in a reasonably linear manner and the data agree rather well with the results of Oda et.al. which are also shown in Figure 4.3. This is equivalent to agreement with the Rheo-Optical Law (Eq 2.31, page 14) in the melt.

B. DISCUSSION

The birefringence Δn_{12} and Δn_{13} data of Figure 4.1 and 4.2 can be used to compute orientation factors, f_1^B and f_2^B. For the approximately uniaxial case of Figure 4.1,

$$f_1^B > 0 \qquad f_2^B \sim 0 \tag{4.6}$$

with f_1^B increasing with drawdown ratio, v_L / v_O. From Figure 4.4, the data at constant blow-up ratio gives

$$f_1^B > 0 \qquad f_2^B > 0 \tag{4.7}$$

f_1^B increases with drawdown, but f_2^B decreases slightly. For the equal biaxial film

$$f_1^B = f_2^B \sim 0.01 \tag{4.8}$$

These results for the orientation factors are plotted in Figure 4.4 as f_1^B versus f_2^B. For such a plot all states of orientation lie within an isosceles triangle as discussed by White and Spruiell (90). Because of the relatively modest orientations generated in the

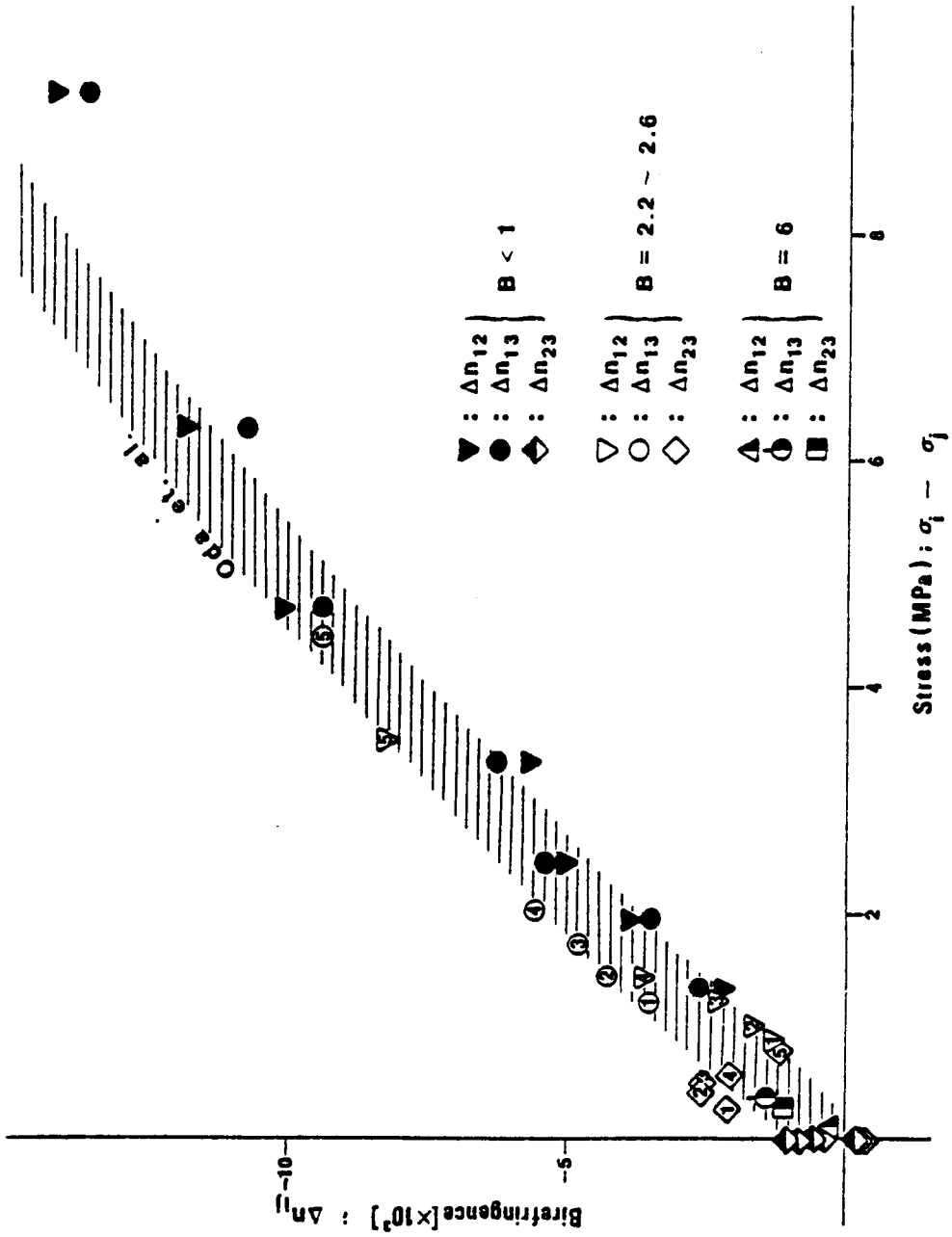

Figure 4.3 Birefringence of polystyrene films as a function of applied stress at vitrification for tubular film extrusion. Comparison with Oda, White, and Clark correlation.

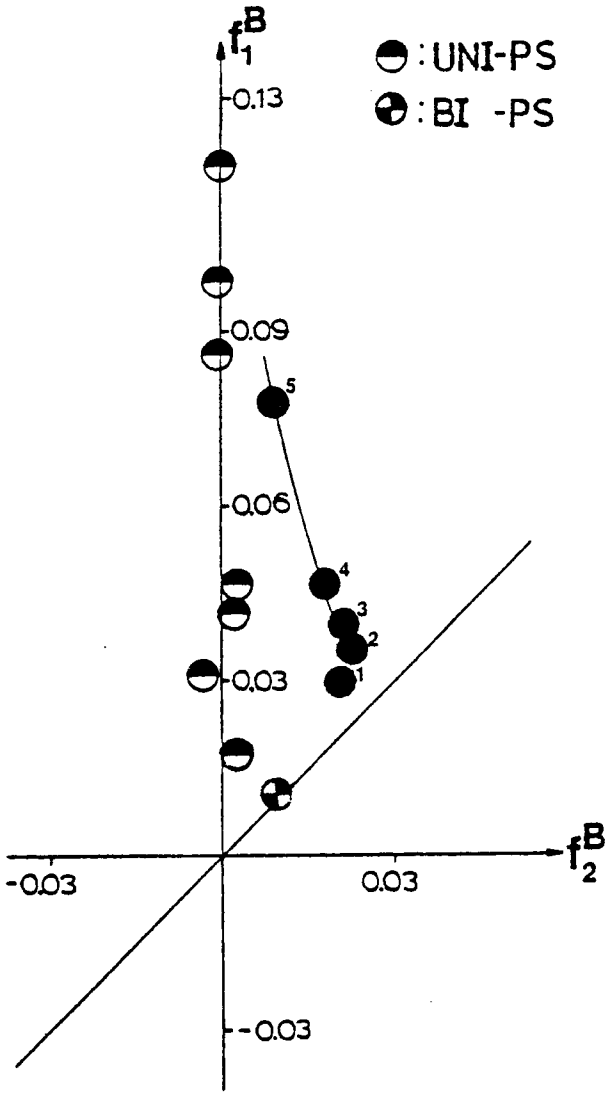

Figure 4.4 Representation of biaxial orientation factors of extruded polystyrene tubular film on a triangular diagram.

polystyrene blown films, only the region near the origin of f_1^B versus f_2^B space is shown. Uniaxial states lie along the coordinate axes while states of equal biaxial orientation lie along a line at 45° to either coordinate axis. As expected the data for the uniaxial films lie along the f_1^B axis. All of the data lie in the upper quadrant indicating that the chain orientation in the samples is intermediate between random (isotropic) and planar (chains parallel to film). For a blow-up ratio of ~ 2.5, the data progresses with increasing drawdown from a position near the equal biaxial orientation line to a position representing nearly uniaxial orientation.

It is striking that the equal biaxial film has rather low orientation levels. This is despite the high blow-up ratio. In order to achieve biaxial orientation, the blow-up ratio must equal the drawdown ratio. This severely limits the drawdown and the level of stresses which can be developed.

The agreement between these data, White and Dietz prediction (89), Eq 2.69, page 33, and Oda et.al.'s (62) correlation is of great importance. It allows apriori predictions of birefringence from process conditions for tubular film extrusion of polystyrene. Presumably, the approach could be readily extended to blown films of other amorphous polymers; it would be necessary only to know the stress-optical coefficient and the intrinsic birefringence of the polymer. Perhaps more significantly it shows the validity of this approach in multiaxial extension and encourages its use to interpret other multiaxial processing operations such as blow molding or thermoforming.

4.2 SEMI-CRYSTALLINE POLYMER (HDPE)

A. RESULTS

The birefringences and densities measured on the polyethylene film samples are listed in Table 4.1. The Δn_{12}, Δn_{13} and Δn_{23} are plotted as a function of drawdown ratio (v_L / v_0) for the uniaxial and constant blow-up ratio series samples in Figure 4.5 and Figure 4.6.

For the approximately uniaxial case

$$\Delta n_{13} \sim \Delta n_{12} > 0 \qquad 4.9$$

and

$$\Delta n_{23} \sim 0 \qquad 4.10$$

with the magnitude of Δn_{13} increasing with drawdown. Except for the change in sign of the birefringence due to the change in sign of the chain polarizabilities, this behavior is similar in qualitative appearance to that of polystyrene.

In Figure 4.6 the constant blow-up ratio series samples show

$$\Delta n_{13} > \Delta n_{12} > \Delta n_{23} > 0 \qquad 4.11$$

with all birefringences increasing monotonically with drawdown ratio.

In the case of the biaxial film

$$\Delta n_{12} \sim 1.9 \times 10^{-3} \qquad 4.12$$

and

$$\Delta n_{13} (10 \times 10^{-3}) \sim \Delta n_{23} (8.2 \times 10^{-3}) \qquad 4.13$$

Note that Δn_{12} is comparatively small but not zero; for the pure biaxial case $\Delta n_{12} = 0$.

As described in Chapter 2 crystalline orientation of the HDPE films was studied by preparing pole figures by WAXS techniques.

Table 4.1 Birefringences, Measured Densities, Calculated Crystalline Fraction and Amorphous Orientation Factors of HDPE Blown Films.

Sample	$\Delta n_{12}(\times 10^3)$	$\Delta n_{13}(\times 10^3)$	$\Delta n_{23}(\times 10^3)$	ρ	X	f_2^B	f_1^B
Uni 1	1.51	1.93	0.42	0.957	0.726	-0.400	-0.487
Uni 2	9.85	10.5	0.66	0.957	0.726	-0.367	-0.504
Uni 3	18.1	19.2	1.10	0.956	0.720	0.066	0.232
4	3.97	5.21	1.24	0.955	0.714	-0.335	-0.473
5	8.78	11.0	2.22	0.954	0.707	-0.270	-0.427
6	11.9	16.5	4.62	0.953	0.701	-0.432	-0.454
7	5.81	9.66	3.85	0.955	0.714	-0.145	-0.423
Bi: 8	1.87	10.0	8.15	0.953	0.701	-0.034	-0.014

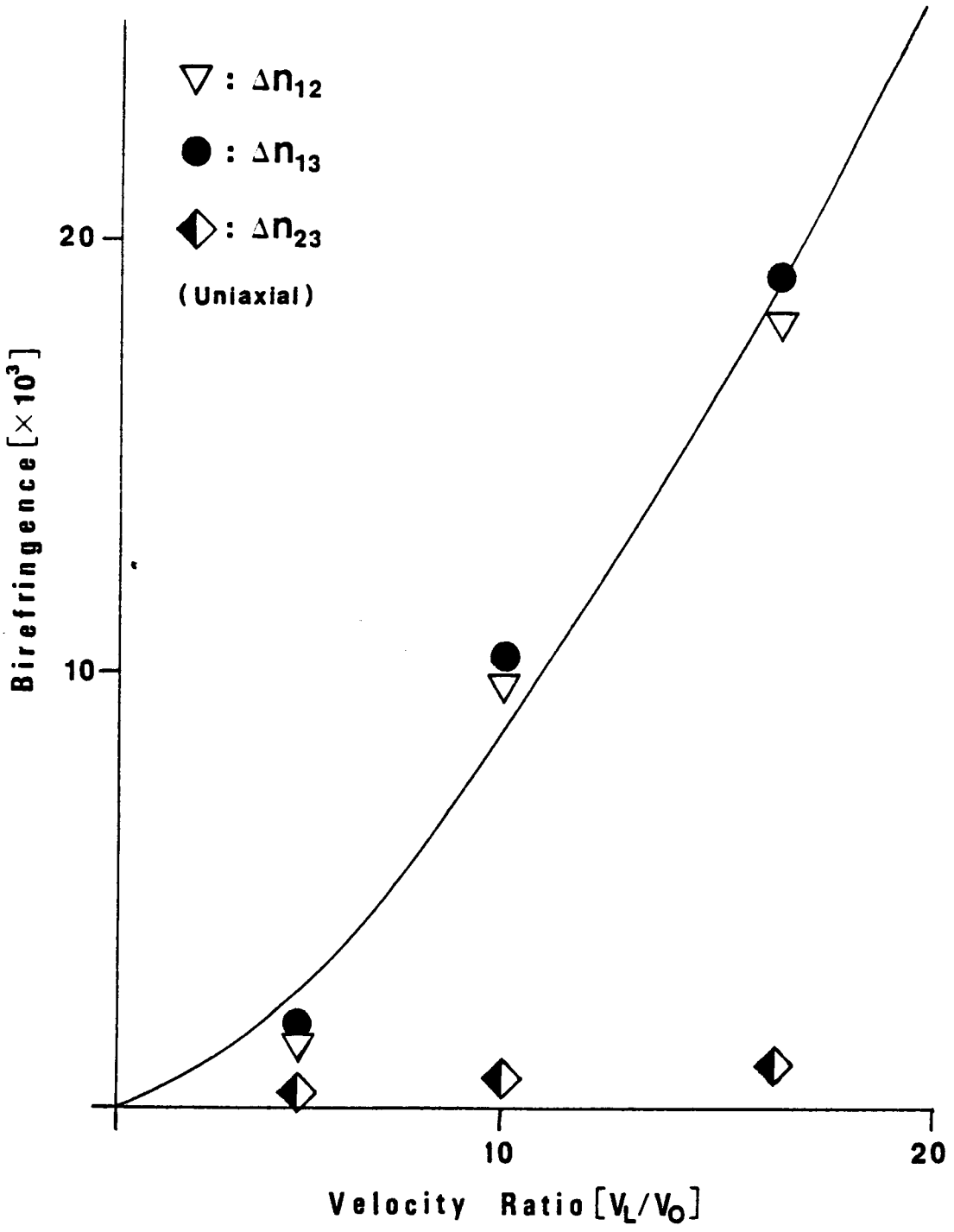

Figure 4.5 Birefringence of HDPE tubular film as a function of drawdown condition-uniaxial.

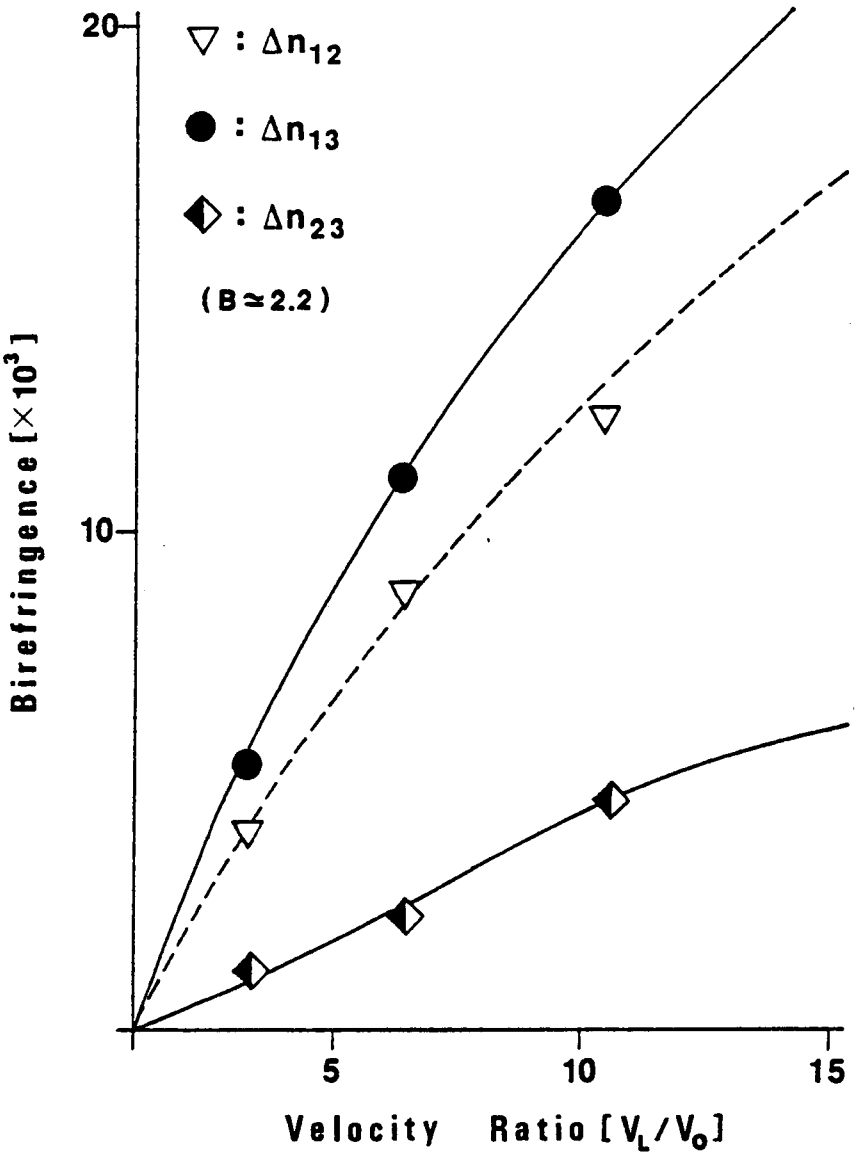

Figure 4.6 Birefringence of HDPE tubular film as a function of drawdown condition for B~2.2.

Examples of the 200 and 020 pole distributions (pole figures) are presented for four cases in Figure 4.7 through 4.14. The figures present the results for samples 1, 3, 6 and 8, respectively. Samples 1 and 3 are approximately uniaxial cases corresponding to the lowest drawdown, sample 1, and the highest drawdown, sample 3. Sample 6 corresponds to the highest drawdown sample with a blow-up ratio of 2.2 while sample 8 is the most nearly biaxial case. The pole figures for the remaining samples (2, 4, 5, 7) and 110 pole figures of samples 1, 3, 6 and 8 are presented in the Appendix.

For the approximately uniaxial case, samples 1-3, sample 1 from the lowest drawdown ($v_L/v_0 = 5.2$) clearly shows a tendency for a-axis orientation along the machine direction (see 200 pole figure, Figure 4.7). The b-axes of this sample are almost perpendicular to MD and are randomly disposed in the TD-ND plane (see 020 pole figure, Figure 4.8). With increasing drawdown, samples 2 and 3, the a-axes are almost uniformly distributed around the machine direction but exhibit maxima at about 47° (sample 2) to 61° (sample 3) away from the machine direction. The b-axes remain nearly 90° to MD but become slightly concentrated in the transverse direction for sample 3. The 110 pole figure for each sample corroborates the other two. The 110 poles are found in a belt at an angle of about 60° to the machine direction. Although the distribution is nearly random about MD, the highest contour lines show a tendency to concentrate slightly in the transverse direction with increasing drawdown. Since the 110 pole lies in the ab plane at an angle of 57° from a, the location of these 110 maxima are consistent with the a-axis and b-axis distributions. Generally pole

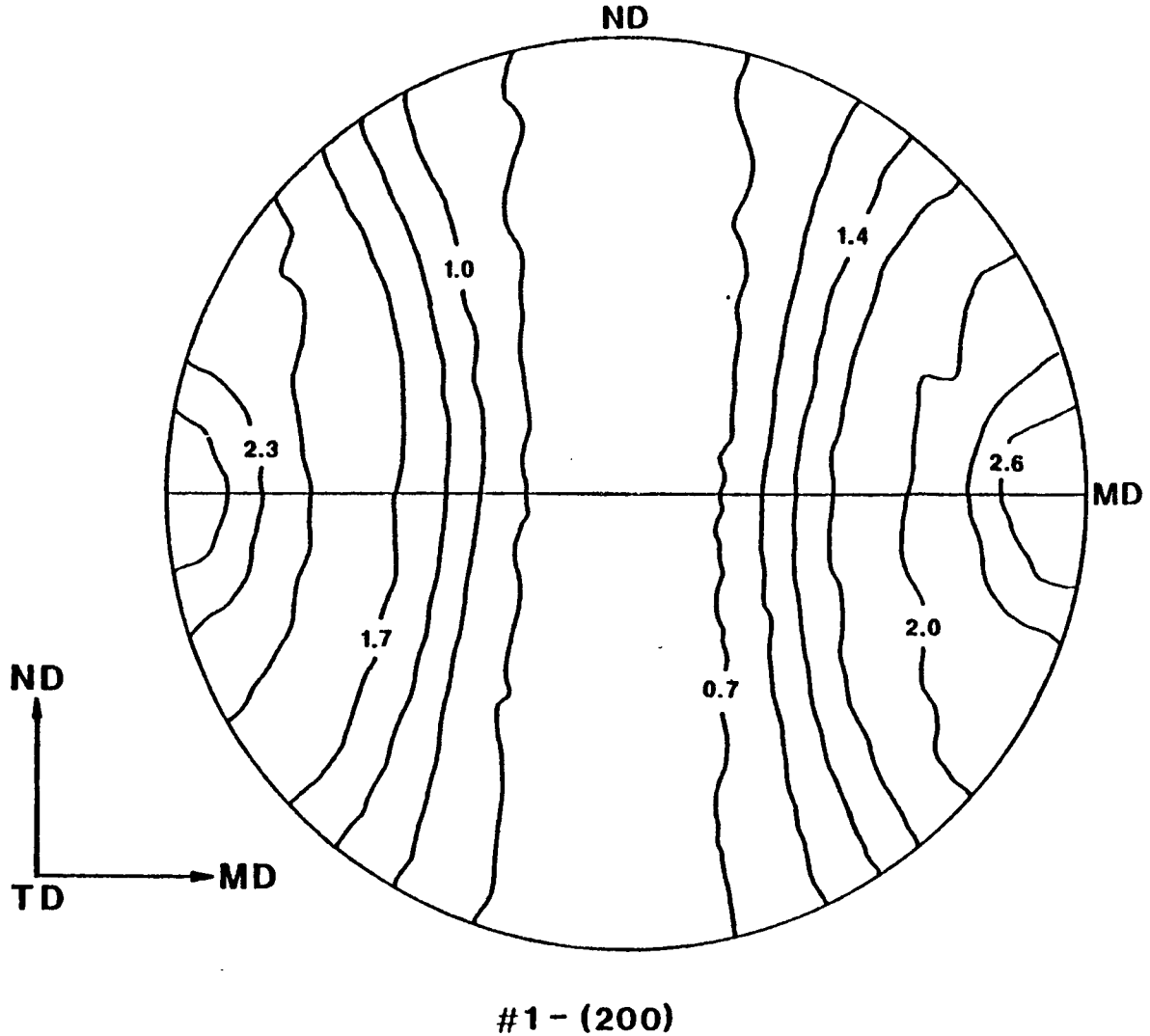

Figure 4.7 200 pole figure of sample 1.

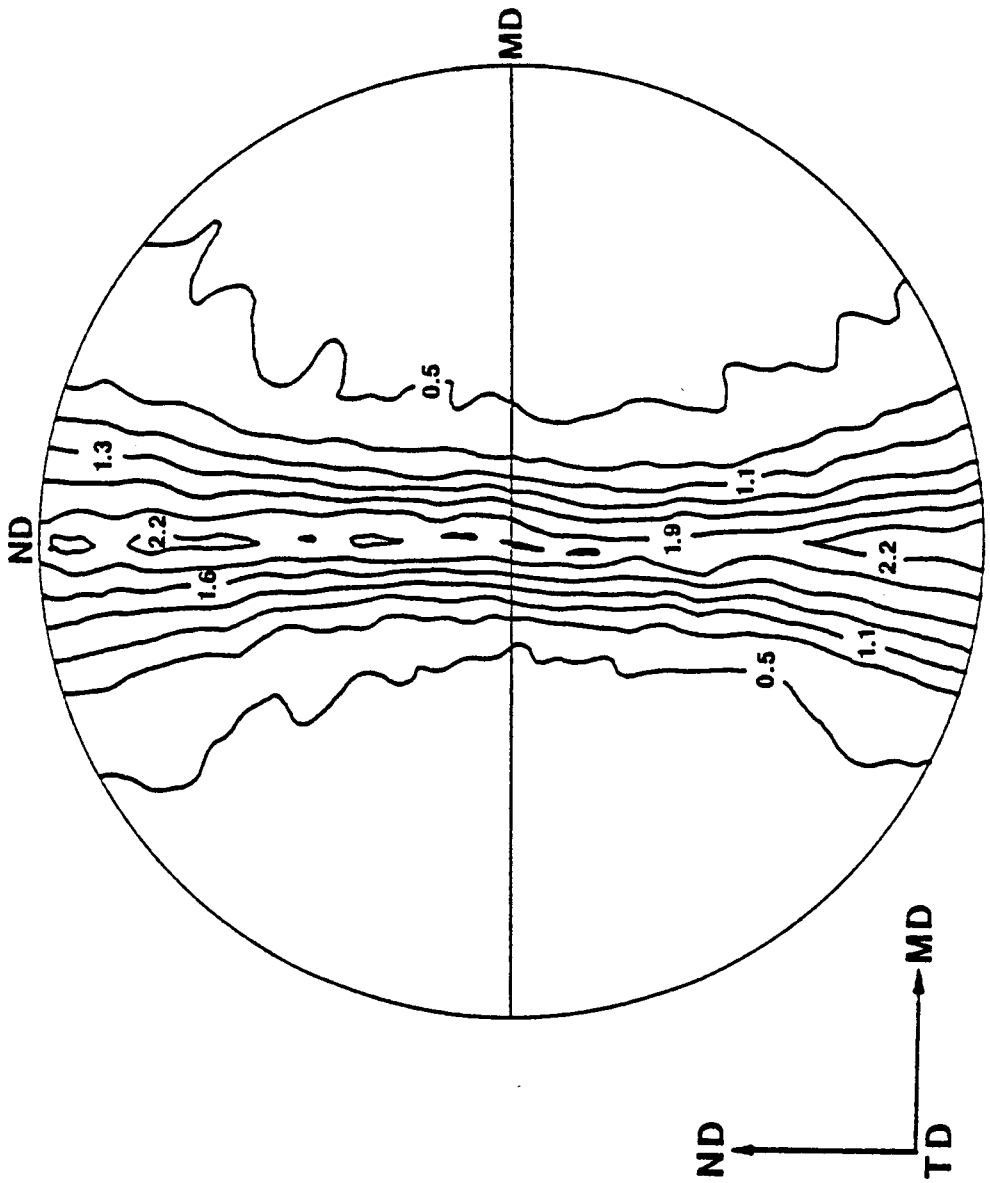

Figure 4.8 020 pole figure of sample 1.

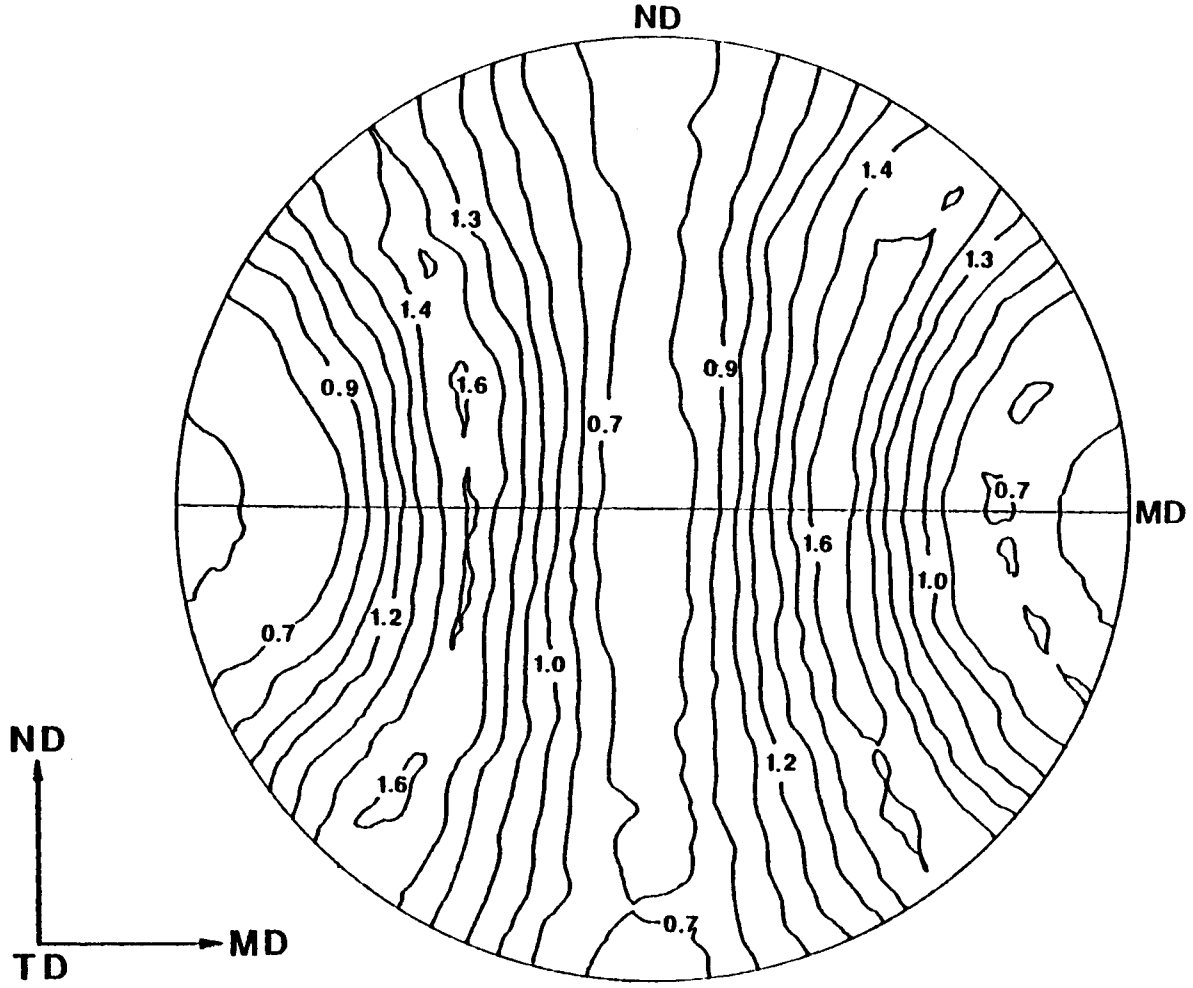

Figure 4.9 200 pole figure of sample 3.

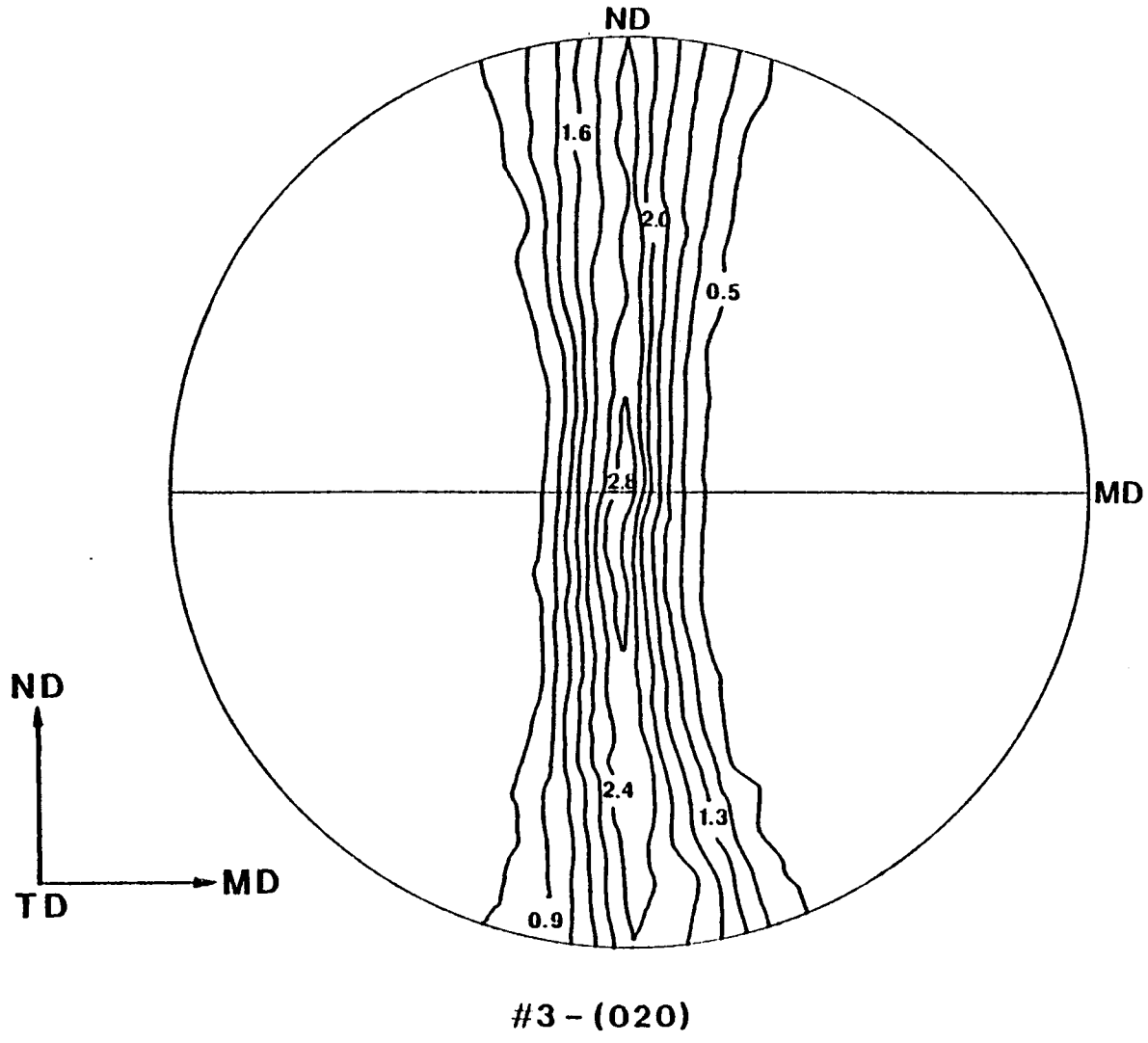

Figure 4.10 020 pole figure of sample 3.

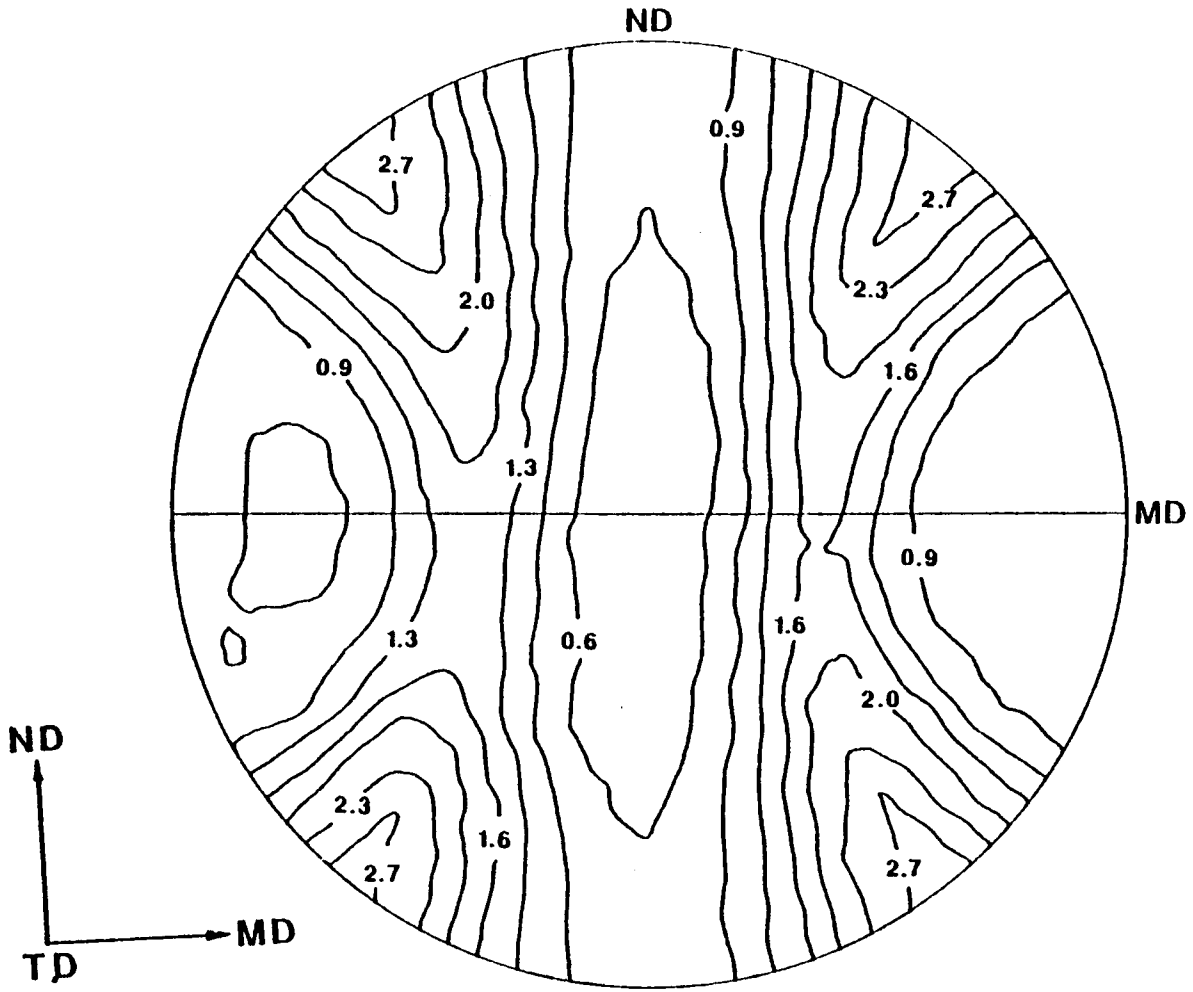

#6 - (200)

Figure 4.11 200 pole figure of sample 6.

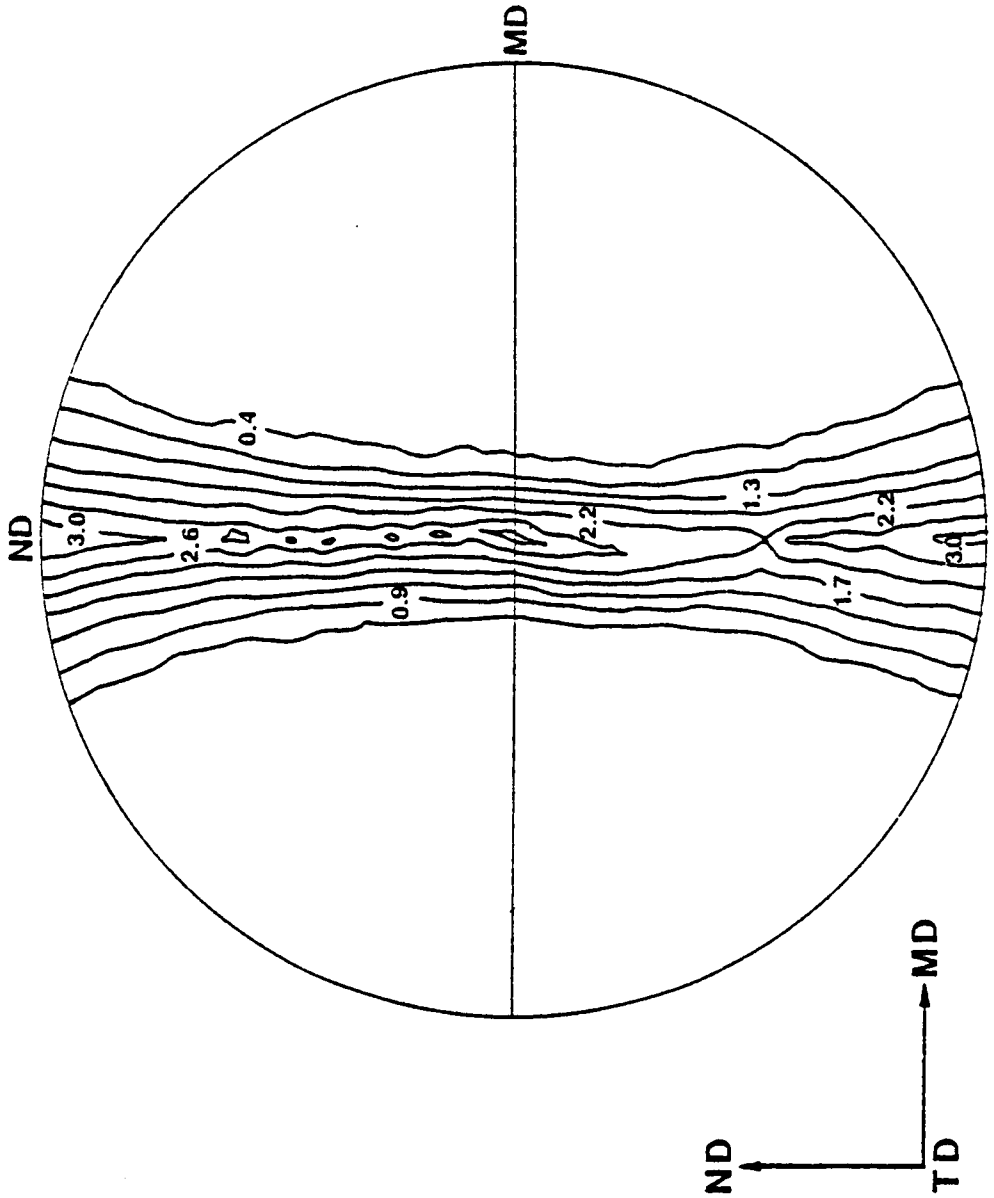

Figure 4.12 020 pole figure of sample 6.

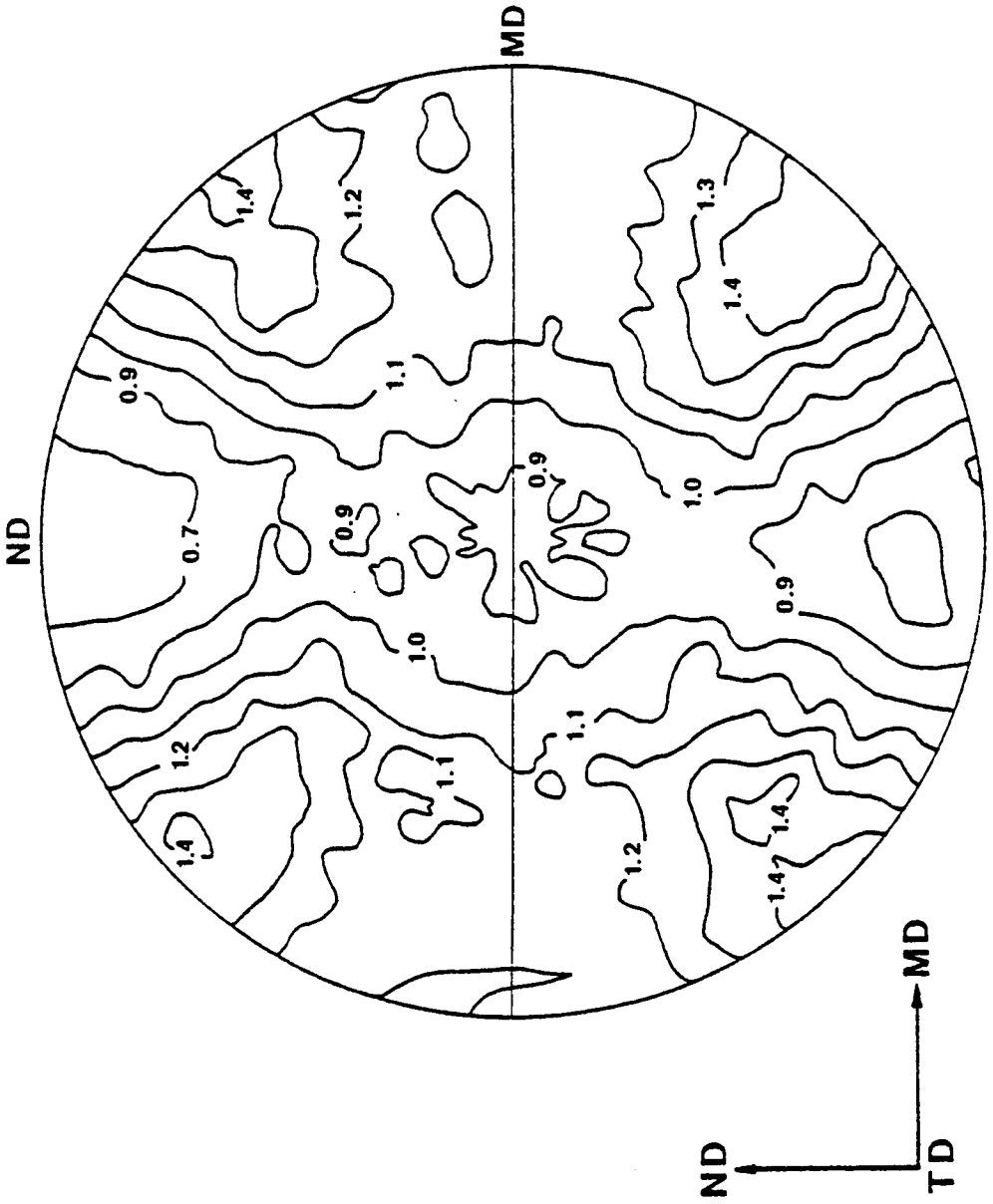

#8-(200)

Figure 4.13 200 pole figure of sample 8.

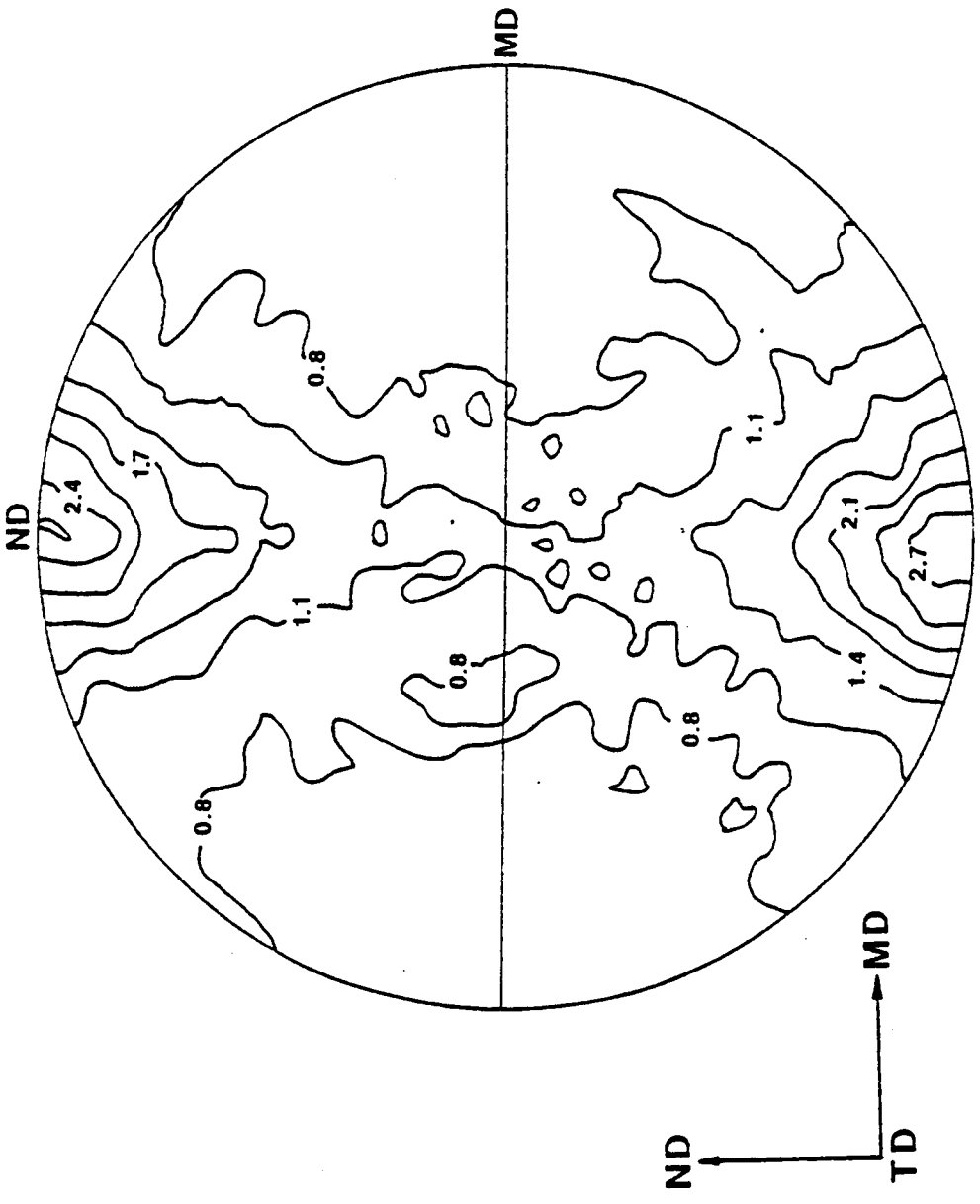

Figure 4.14 020 pole figure of sample 8.

figures for sample 1-3 indicate that these samples are very nearly uniaxially oriented along the machine direction.

The samples in the constant blow-up ratio series (B~2.2) are labeled 4 through 6. The b-axis distributions are almost the same as those of the uniaxial samples 1 to 3 except that the b-axes of sample 6 with the highest drawdown, are very slightly biased toward the normal direction while they are slightly concentrated toward TD in sample 3 (see 020 pole figures, Figure 4.10 and 4.12), the a-axis distribution shows slightly different behavior from that for the uniaxial case. The 200 pole figure of samples 4 through 6 show that the distributions of a-axes exhibit a maximum in each quadrant in the MD-ND plane. This maximum intensity concentration increases and a-axis uniaxiality about the machine direction decreases with increasing drawdown (4→5→6). The 110 pole figure of sample 6 also confirms this tendency (see Figure Appendix A.15).

The pole figures of sample 7 look almost the same as those of sample 5 but the b-axis distribution is similar to that of sample 4.

For the biaxial film, sample 8, the a-axis distribution also exhibits a maximum in the MD-ND plane in each quadrant, but it is much weaker than for sample 6 and there is greater intensity in areas of the pole figure that were very weak for sample 6. A striking feature of Figure 4.14 is that the b-axis distribution is concentrated in the direction normal to the film (020 pole figure).

Figure 4.15 shows the effect of processing conditions on small angle x-ray scattering (SAXS) patterns taken with the beam normal to the film plane.

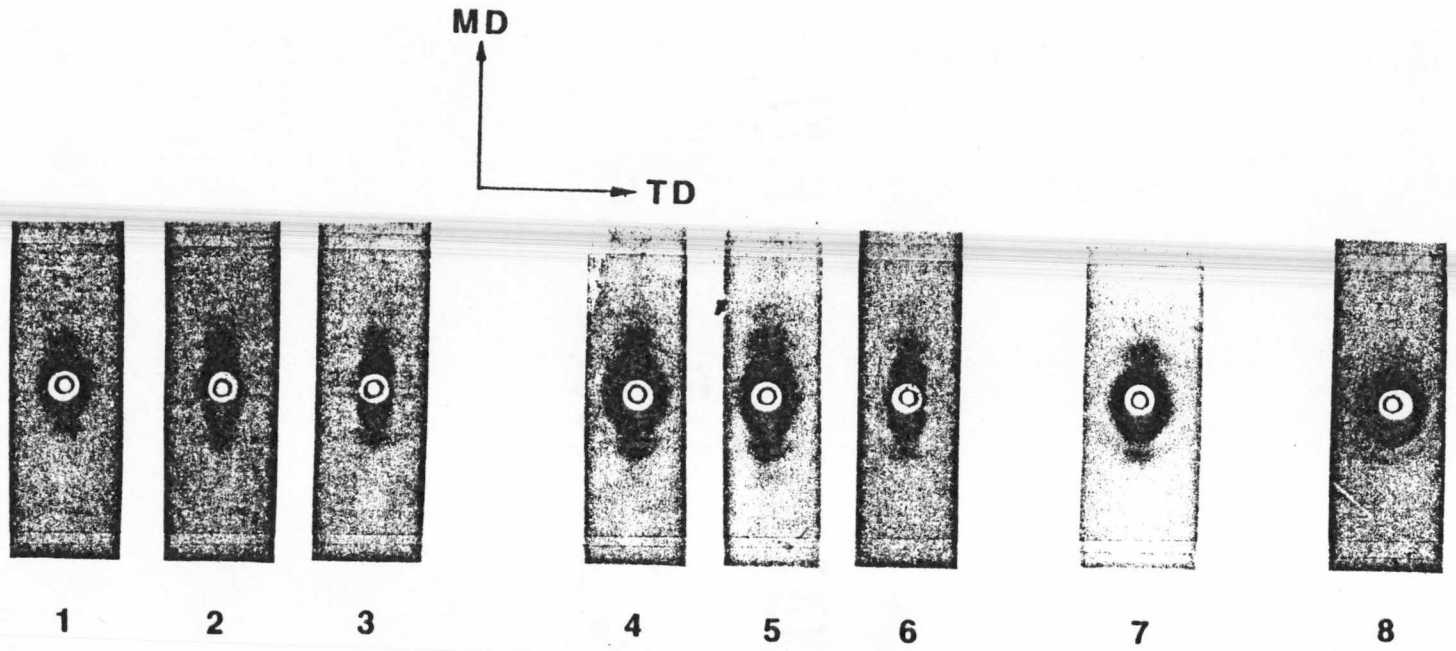

Figure 4.15 The effect of processing conditions on SAXS patterns taken with the beam normal to the film plane.

For the uniaxial case 1-3, the SAXS patterns of sample 1 at low drawdown exhibit a continuous ring with a maximum on the meridian which gradually changes to a definite two point pattern with increasing drawdown.

For the constant blow-up ratio series (B~2.2), sample 4-6, the SAXS patterns are nearly the same as those of uniaxial case but a little more dispersed around the beam stop, especially for the lower drawdown ratio samples 4 and 5. The SAXS pattern of sample 7 is similar to that of sample 4.

For the biaxial film, sample 8, the SAXS pattern exhibits two nearly uniform rings around the beam stop (first and second order maxima). The second order ring is difficult to observe on the reproduction in Figure 4.15 but is easily seen on the original pattern. In order to ascertain whether the lamellar orientation distribution in this sample is isotropic or has biaxial symmetry, two additional SAXS patterns were made with the beam along either the TD or the MD directions. These patterns are shown in Figure 4.16. These results exhibit two point patterns representing a periodicity along the MD (Figure 4.16a) and along the TD (Figure 4.16b). In the original patterns two orders of these intensity maxima are readily observed. In addition to the two point patterns intense diffuse streaks along the equator are also observed in these patterns. It is believed that these streaks result from the void scattering associated with laminating many films together in order to obtain samples for these patterns. In each pattern the diffuse streaks occur along a direction normal to the film surface as would be expected from this source. These streaks are thus

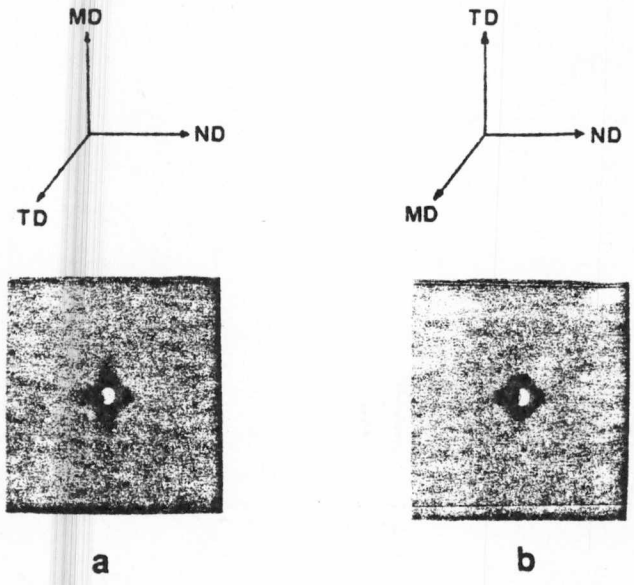

Figure 4.16 SAXS patterns made with beam along the TD(a) and along the MD(b) for the biaxially oriented HDPE film.

believed to be artifacts that are unrelated to the internal structure of the films.

B. INTERPRETATION AND DISCUSSION

ORIENTATION REPRESENTATION; The crystalline orientation and birefringence results presented above may be interpreted quantitatively in terms of White and Spruiell's orientation factors.

The six cosine squared values, $\cos^2\phi_{a1}$ $\cos^2\phi_{a2}$ $\cos^2\phi_{b1}$ $\cos^2\phi_{b2}$ $\cos^2\phi_{c1}$ $\cos^2\phi_{c2}$, calculated from the pole figure data of each sample are listed in Table 4.2. These cosine squared values can be expressed in terms of White and Spruiell's biaxial orientation factors relative to each crystallographic axis through Eq 2.52 through 2.54, page 23. These are given in Table 4.3. These are also plotted as a function of drawdown ratio in Figure 4.17 and Figure 4.18.

For the uniaxial case 1 to 3

$$\begin{array}{llll} f^B_{a1} > 0 & & f^B_{a2} < 0 & \\ f^B_{b1} < 0 & & f^B_{b2} < 0 & \\ f^B_{c1} > 0 & & f^B_{c2} > 0 & \end{array} \qquad 4.14$$

and

$$\begin{array}{llll} f^B_{a1} \rightarrow 0 & & f^B_{a2} \rightarrow 0 & \\ f^B_{b1} \rightarrow -1/2 & & f^B_{b2} \rightarrow 0 & \\ f^B_{c1} \rightarrow +1/2 & & f^B_{c2} \rightarrow 0 & \end{array} \qquad 4.15$$

with increasing drawdown. The data at constant blow-up, sample 4 to 6, and sample 7 give

$$\begin{array}{llll} f^B_{a1} > 0 \text{ or } < 0 & & f^B_{a2} < 0 & \\ f^B_{b1} < 0 & & f^B_{b2} < 0 & \end{array} \qquad 4.16$$

Table 4.2 Cosine Squared Values of HDPE Blown Film.

Sample		$\overline{\cos^2\phi_{a2}}$	$\overline{\cos^2\phi_{a1}}$	$\overline{\cos^2\phi_{b2}}$	$\overline{\cos^2\phi_{b1}}$	$\overline{\cos^2\phi_{c2}}$	$\overline{\cos^2\phi_{c1}}$
Uni	1	0.232	0.483	0.414	0.119	0.345	0.398
	2	0.269	0.409	0.455	0.0551	0.276	0.536
	3	0.311	0.345	0.485	0.0504	0.204	0.604
	4	0.240	0.468	0.438	0.0815	0.322	0.451
	5	0.259	0.411	0.453	0.0533	0.288	0.536
	6	0.257	0.367	0.439	0.0320	0.304	0.601
	7	0.270	0.403	0.422	0.0908	0.308	0.507
Bi:	8	0.296	0.358	0.315	0.212	0.389	0.430

Table 4.3 Orientation Factors of HDPE Blown Film.

Sample		f_{a2}^B	f_{a1}^B	f_{b2}^B	f_{b1}^B	f_{c2}^B	f_{c1}^B
Uni	1	-0.0527	0.198	-0.0534	-0.348	0.0881	0.141
	2	-0.0530	0.0864	-0.0345	-0.435	0.0875	0.348
	3	-0.0327	0.0016	-0.0196	-0.415	0.0131	0.413
	4	-0.0523	0.175	-0.0421	-0.399	0.0944	0.224
	5	-0.0712	0.0805	-0.0409	-0.441	0.112	0.360
	6	-0.118	-0.0091	-0.0902	-0.497	0.209	0.506
	7	-0.0573	0.0751	-0.0652	-0.396	0.123	0.321
Bi:	8	-0.0499	0.0119	-0.158	-0.261	0.208	0.249

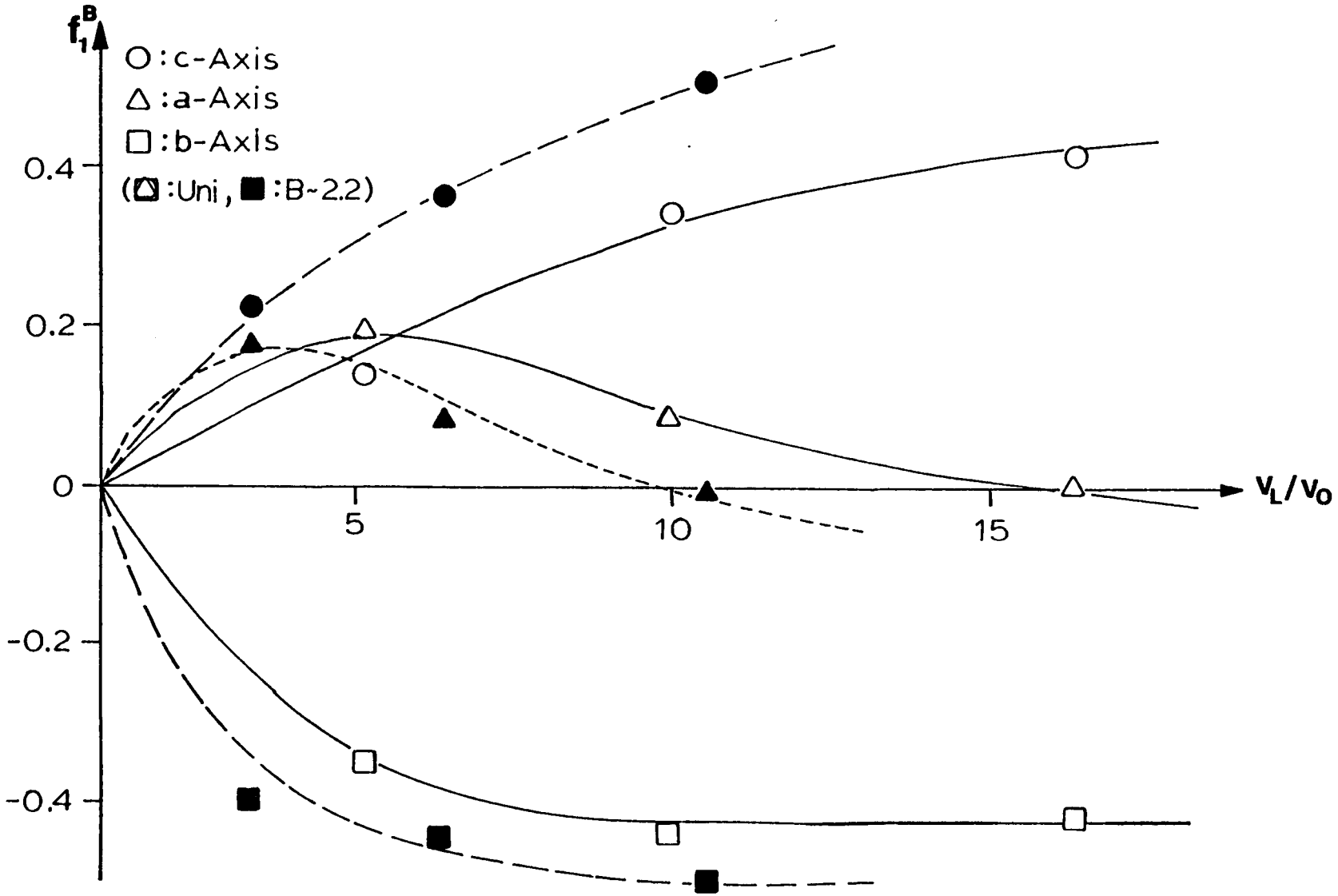

Figure 4.17 Crystalline orientation factor, f_1^B as a function of drawdown ratio.

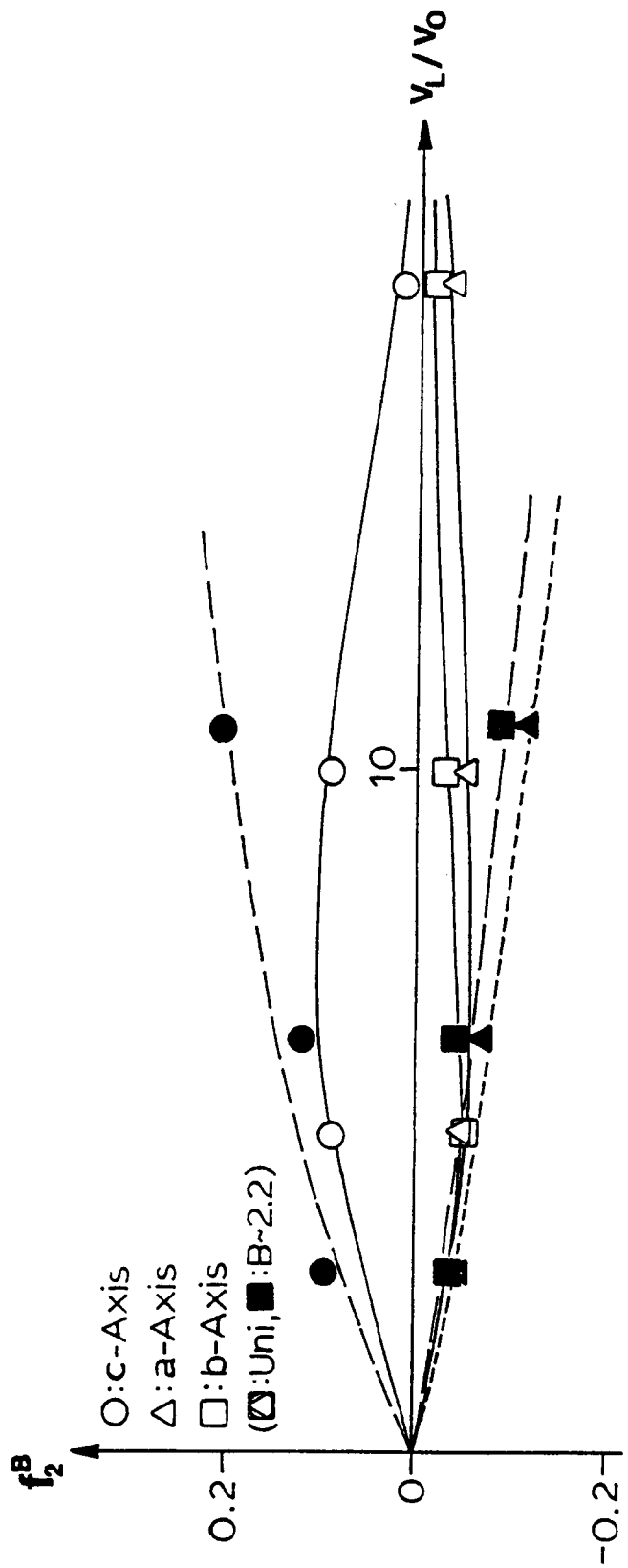

Figure 4.18 Crystalline orientation factor, f_2^B as a function of drawdown ratio.

$$f_{c1}^{B} > 0 \qquad f_{c2}^{B} > 0$$

with increasing drawdown. For the equal biaxial film

$$\begin{aligned} f_{a1}^{B} &\approx f_{a2}^{B} \sim -0.02 \\ f_{b1}^{B} &\approx f_{b2}^{B} \sim -0.2 \\ f_{c1}^{B} &\approx f_{c2}^{B} \sim +o.22 \end{aligned} \qquad 4.17$$

These orientation factors are plotted in Figure 4.19 as f_1^B versus f_2^B on the isosceles triangle diagram. The general trend for either uniaxial or constant blow-up series is toward increasing chain alignment with the machine direction. The fact that the f_{c2}^B values for sample 1 and 2 are greater than zero shows that there is some deviation from perfect uniaxiallity about the machine direction. However, the orientation factors of samples 1-3 approach the f_1^B axis with increasing drawdown showing a tendency toward more nearly uniaxial behavior. The orientation factors for the constant blow-up ratio series moves further from the f_1^B axis with drawdown. This trend is opposite that which would be expected on the basis of kinematic considerations alone and may be caused by oriented crystal growth resulting from the cooling condition. The data for sample 8 lies very near the line at 45° to either coordinate axis indicating that it is biaxially oriented. This sample shows low c-axis (chain axis) orientation levels in spite of the rather high blow-up condition. It is interesting that b-axes are more and more oriented normal to the machine direction with increasing blow-up ratio.

High density polyethylene is highly crystalline for a polymer but its crystallinity is only about 70 % (see Table 4.1, page 64). Therefore orientation in the amorphous regions may be considered. This

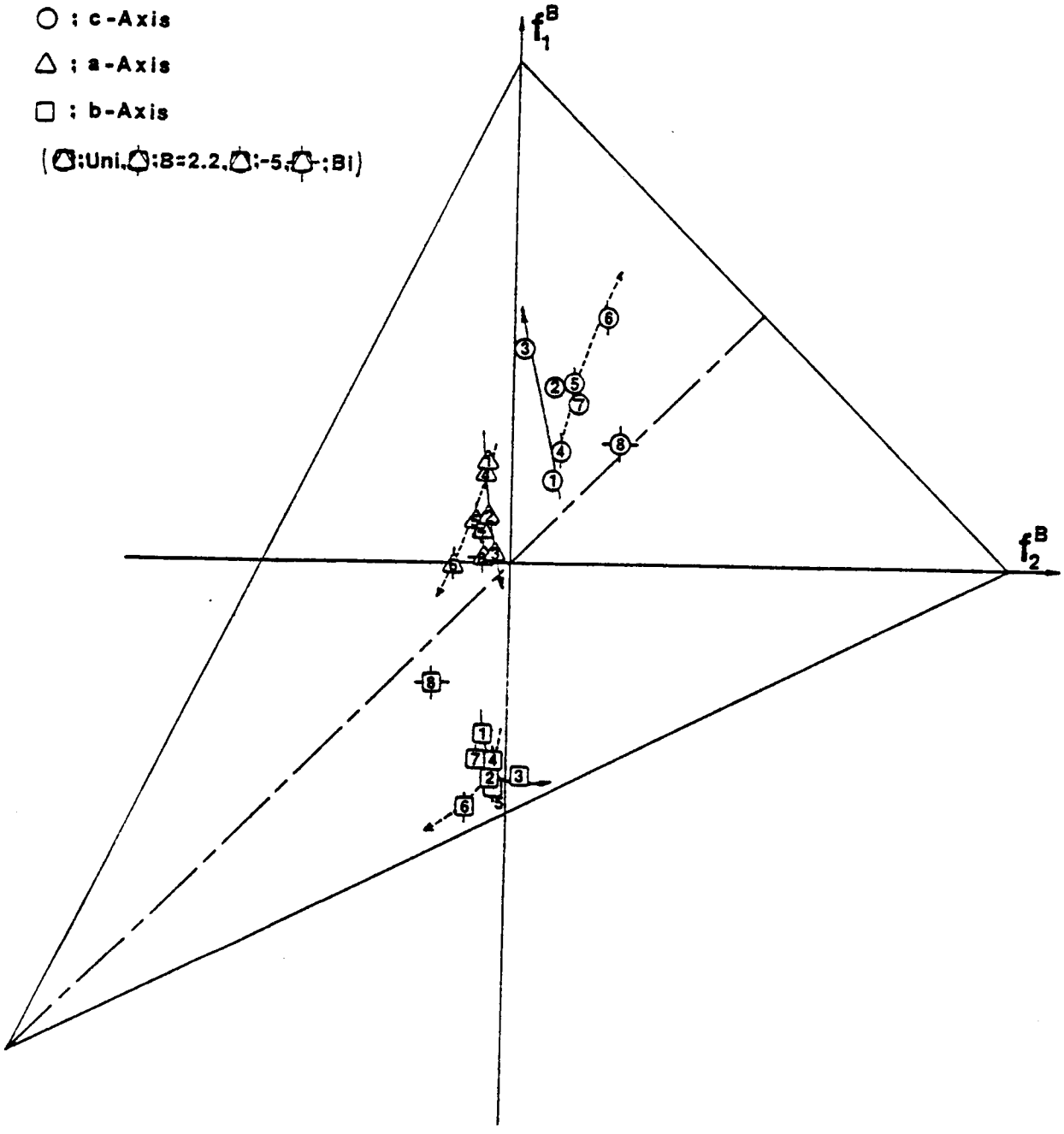

Figure 4.19 Representation of crystalline biaxial orientation factor of HDPE blown film on a triangular diagram.

amorphous orientation factor can be calculated from several measured or calculated results through Eq 2.55, page 23. A problem is that the final calculated value of amorphous orientation involves accumulated errors from each of the measured or calculated results. The results of such calculations must thus be viewed and interpreted with caution. Measured density, calculated crystalline fraction, measured birefringences and calculated amorphous orientation factors are given in Table 4.1. These amorphous orientation factors, f_1^B and f_2^B are plotted as a function of drawdown ratio in Figure 4.20 and Figure 4.21.

Sample 3 shows f_1^B and $f_2^B > 0$ and the others all have both f_1^B and $f_2^B < 0$. For biaxial sample $f_1^B \approx f_2^B \sim -0.03$.

These results are plotted on the isosceles triangle diagram as f_1^B versus f_2^B in Figure 4.22. Here again the biaxial state lies on 45° line and almost isotropic point. The others except sample 3 show that chains in the amorphous region tend to be perpendicular to the film surface.

BIREFRINGENCE AND ORIENTATION VERSUS STRESS; The Rheo-Optical Law (Eq 2.31, page 14) can be applied in the polymer melt. If the directions of flow are the same direction as the principal axes of the stress tensor, we may write for the amorphous orientation factors of the melt

$$f_1^{am} = \frac{\Delta n_{13}^a}{\Delta^{oa}} = \frac{C(\sigma_1 - \sigma_3)}{\Delta^{oa}} = \frac{C}{\Delta^{oa}}\ \sigma_1$$

$$f_2^{am} = \frac{\Delta n_{23}^a}{\Delta^{oa}} = \frac{C(\sigma_2 - \sigma_3)}{\Delta^{oa}} = \frac{C}{\Delta^{oa}}\ \sigma_2 \qquad 4.13$$

where Δn_{13}^a and Δn_{23}^a are the out-of-plane birefringences of the molten

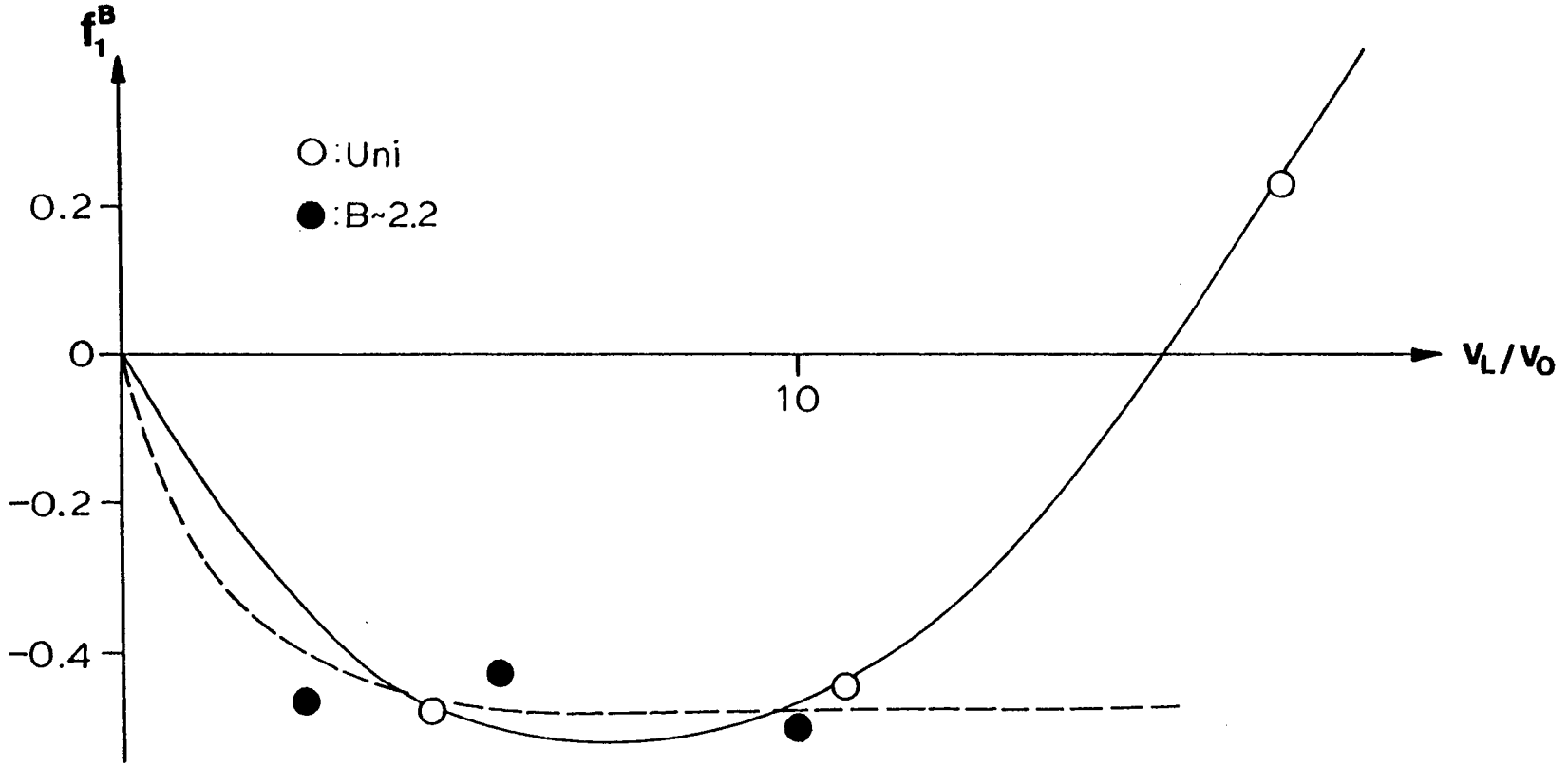

Figure 4.20 Amorphous orientation factor, f_1^B , as a function of drawdown ratio.

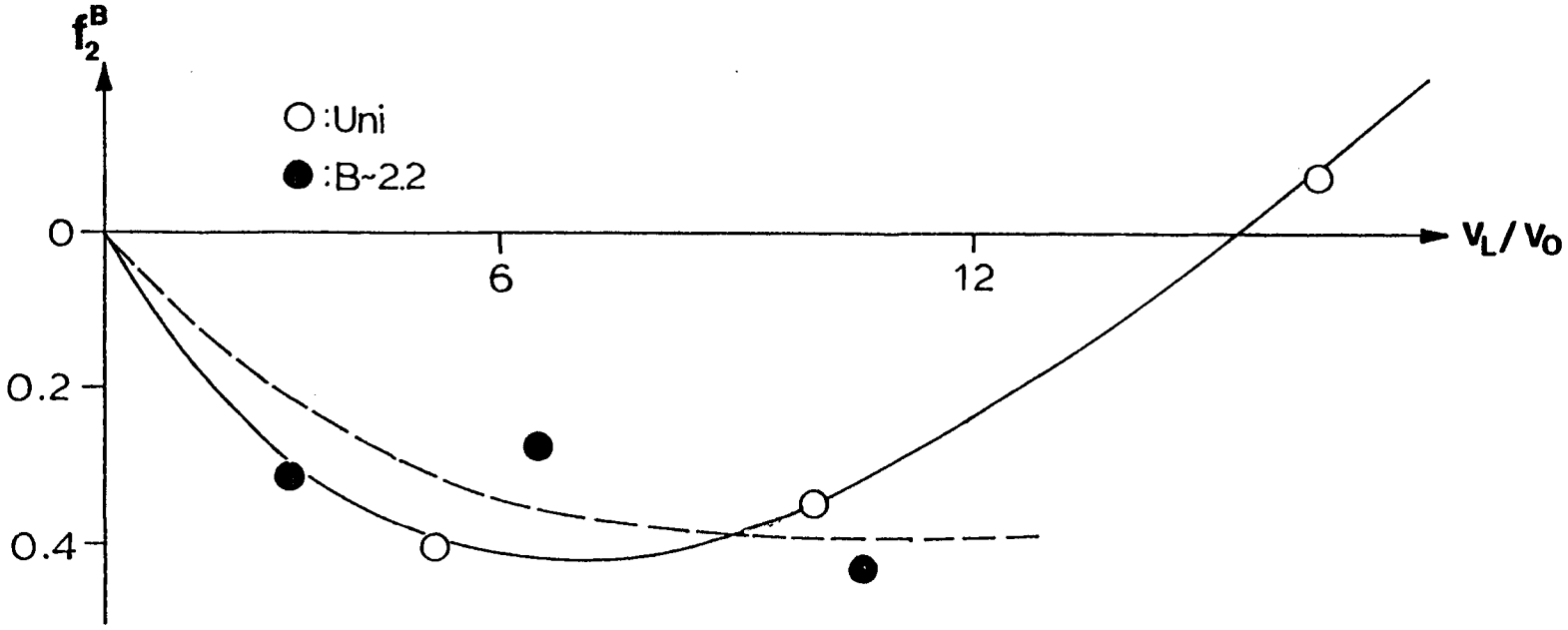

Figure 4.21 Amorphous orientation factor, f_2^B, as a function of drawdown ratio.

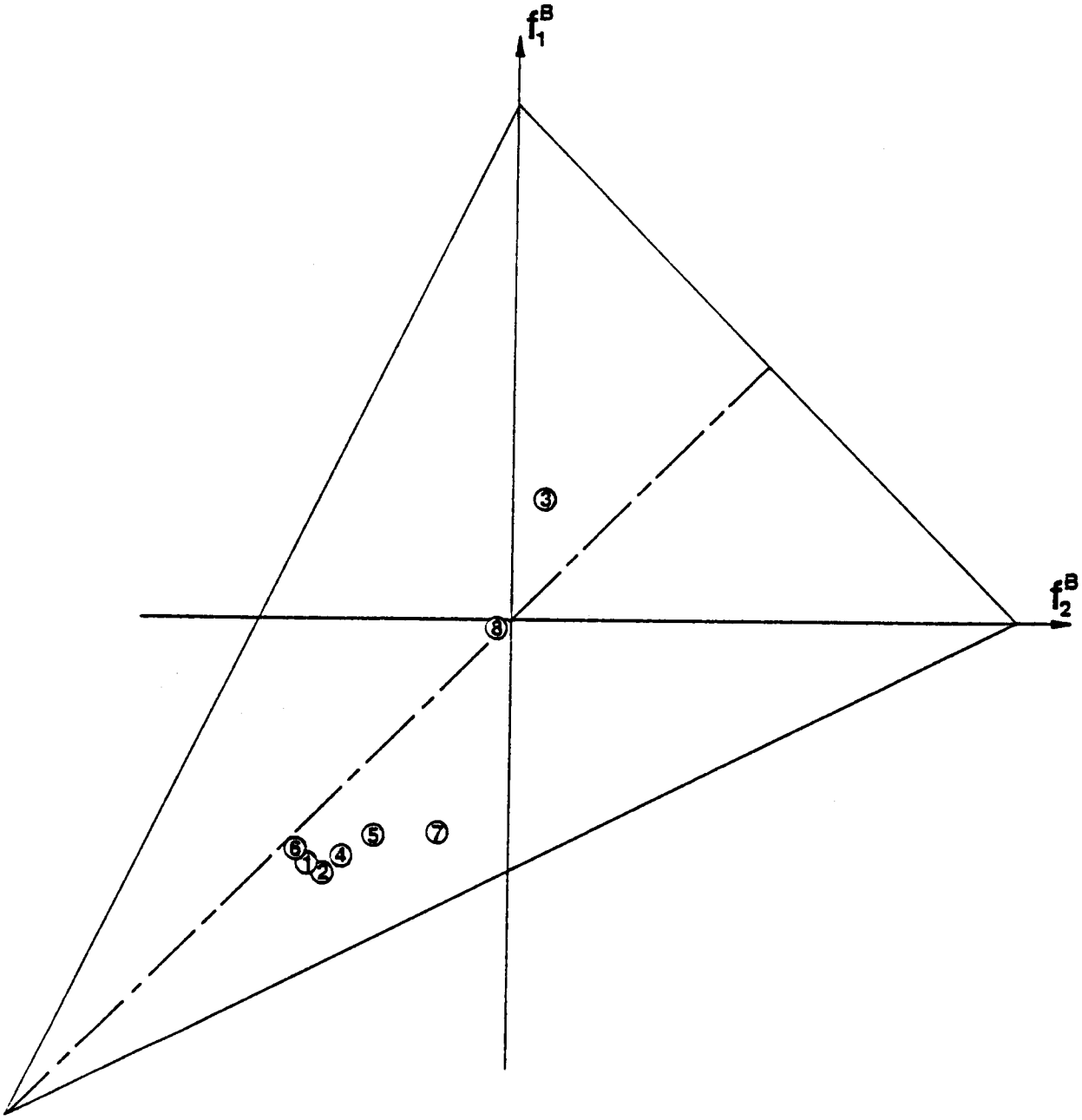

Figure 4.22 Representation of amorphous biaxial orientation factors of HDPE blown film on a triangular diagram.

sheet and the σ's are the principal stresses in the melt.

We may also write

$$f_1^{am} - f_2^{am} = \frac{\Delta n^a_{13} - \Delta n^a_{23}}{\Delta^{oa}}$$

$$= \frac{\Delta n^a_{12}}{\Delta^{oa}} = \frac{C}{\Delta^{oa}} (\sigma_1 - \sigma_2) \qquad 4.19$$

The orientation in the melt just prior to crystallization should thus be determined by the stress state. When crystallization occurs there will be a discontinuous change in orientation due to oriented nucleation and growth processes. Unlike the vitrified amorphous polystyrene samples discussed in Chapter 2, the state of orientation in the solidified semi-crystalline polymer cannot be directly predicted from the stress state on the basis of equations 4.18 and 4.19. This can be demonstrated by plotting the experimental orientation factors versus the appropriate principal stress differences and comparing these to the curve predicted by equation 4.18. Such a plot is shown in Figure 4.23. Both the crystalline c-axis orientation factors determined from WAXS data and "apparent average chain axis orientation factors" determined by dividing the experimental birefringence results by the intrinsic birefringence of the crystalline phase are shown. The latter differ from the former because of the contribution of the amorphous phase to the measured birefringence and the fact that the intrinsic birefringence of the crystalline phase is used. Although there is considerable scatter, a strong correlation of the measured orientation factors with principal stress difference is observed. However, the slope of this relation is much higher than is predicted by

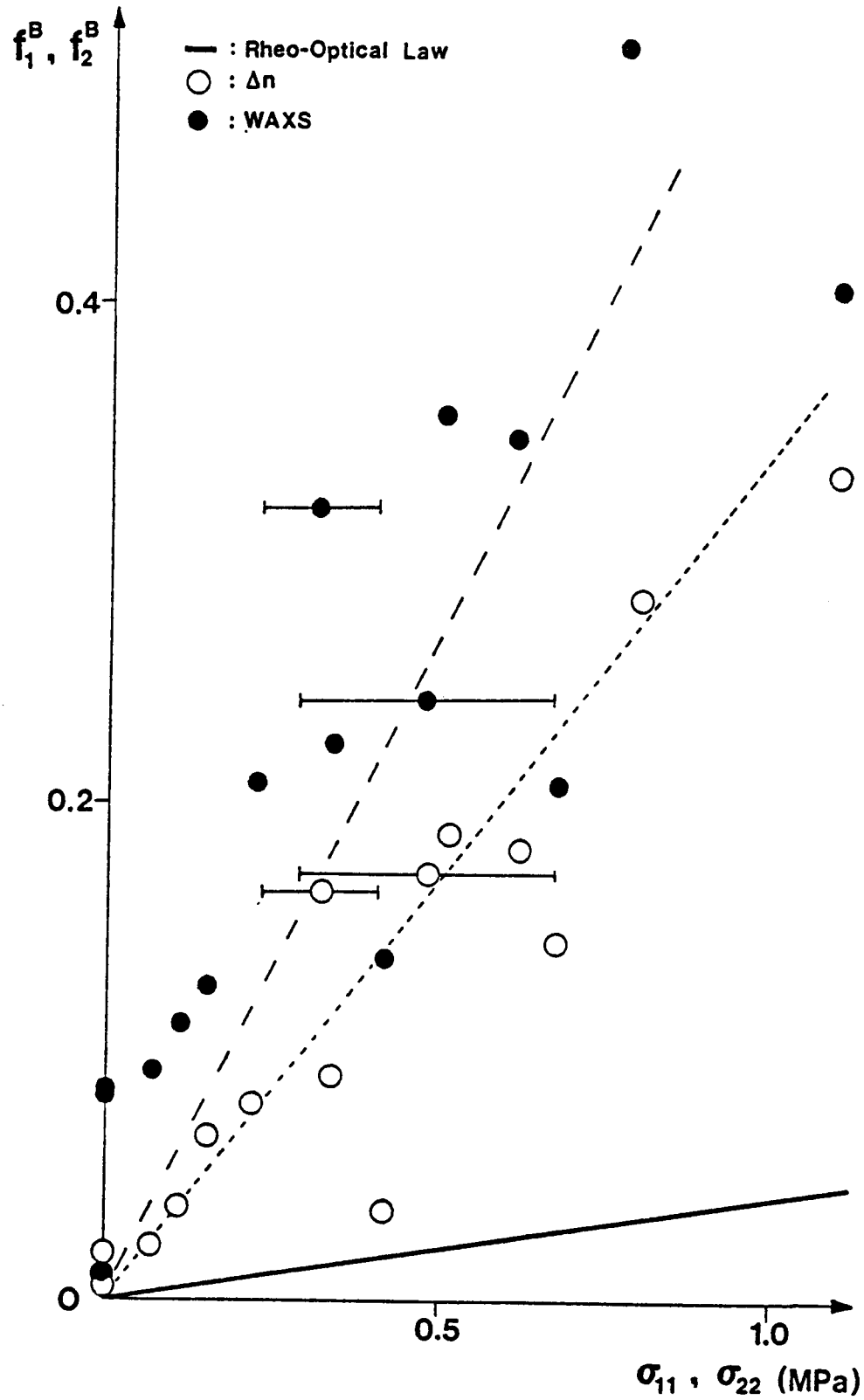

Figure 4.23 C-axis orientation factors from WAXS, birefringence and Rheo-Optical Law as a function of applied stress.

equation 4.18 (compare to lower curve in Figure 4.23). An equivalent way to present this result is to plot the experimental room temperature birefringences of the films versus $\sigma_i - \sigma_j$; that is Δn_{12} versus $\sigma_{11} - \sigma_{22}$, Δn_{13} versus σ_{11}, Δn_{23} versus σ_{22} as in Figure 4.24. Data obtained by Dees and Spruiell (9) for HDPE melt spun fiber are also coplotted in Figure 4.24 and show a high correlation with the present results for film. Although an approximately linear relationship is observed between Δn_{ij} and $\sigma_i - \sigma_j$, the slope of this curve for semi-crystalline polyethylene is much greater than the stress-optical coefficient, c, for the melt.

In spite of the fact, demonstrated above, that the state of orientation cannot be predicted from equations 4.18 and 4.19 for semi-crystalline polymers, Nadella et al. (55) have presented evidence that for the uniaxial case of fiber spinning the orientation and crystalline morphology of a given polymer are determined by the melt stress just prior to crystallization independent of secondary variables such as melt extrusion temperature, take-up velocity, etc. In effect this argument states that (for the uniaxial case) the a, b and c-axis orientation factors are each functions of the uniaxial stress, σ_{11}, and the nature of crystallization induced orientation changes for the particular polymer. The nature and sensitivity of a given polymer to orientation and morphology changes associated with oriented crystallization must at present be determined for each polymer by experiment. Symbolically, we may write

$$f_a = F_a(\sigma_{11}, \text{polymer}) \qquad 4.20a$$

$$f_b = F_a(\sigma_{11}, \text{polymer}) \qquad 4.20b$$

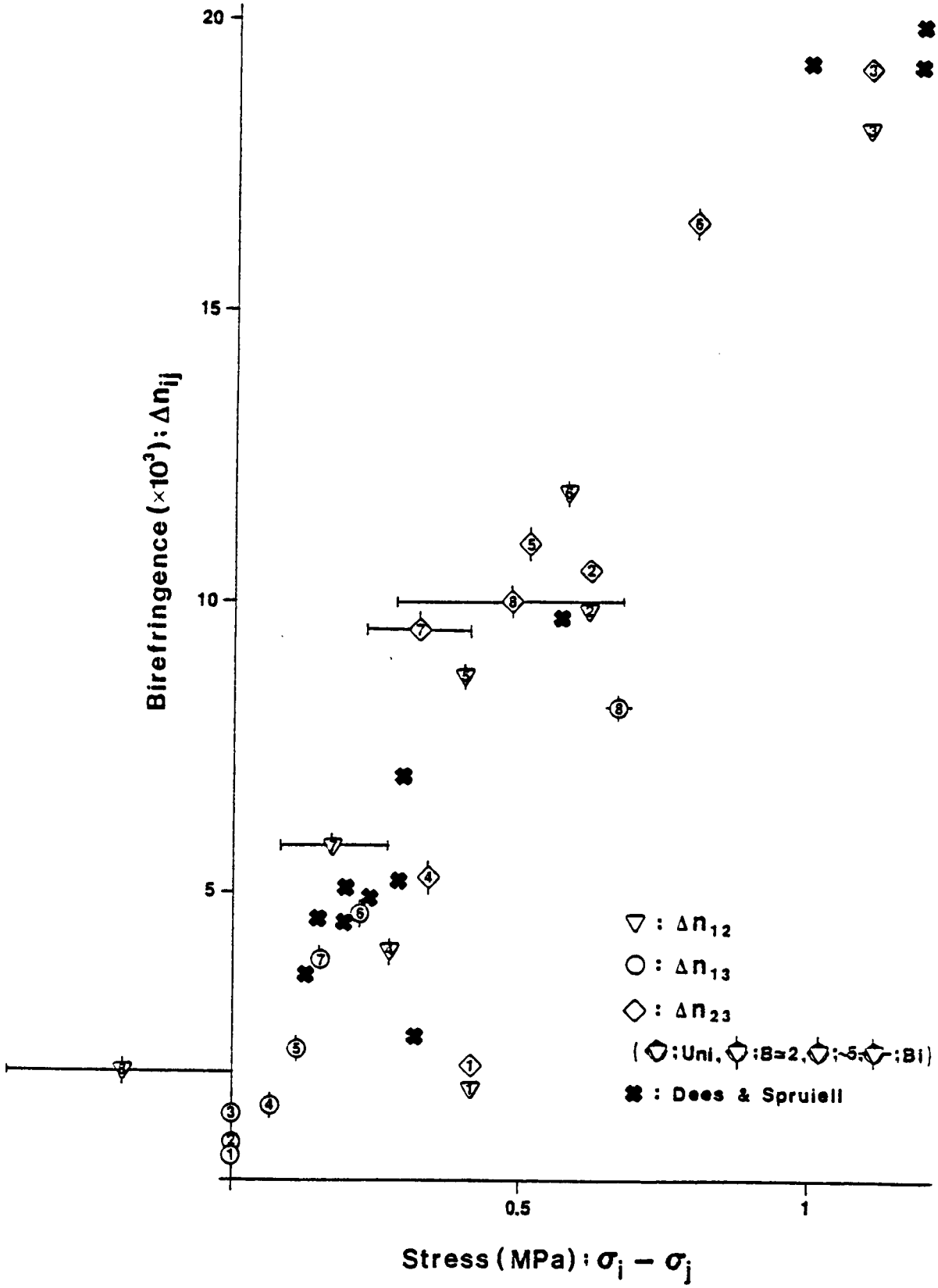

Figure 4.24 Birefringences of, HDPE blown film and melt spun fiber by Dees and Spruiell as a function of applied stresses difference.

$$f_c = F_c(\sigma_{11}, \text{polymer}) \qquad 4.20c$$

In order to extend this idea to the multiaxially oriented thin sheet samples we might presume that

$$f_{i1}^B = G_i(\sigma_{11} - \sigma_{33}, \text{polymer}) \qquad 4.21a$$

$$f_{i2}^B = G_i(\sigma_{22} - \sigma_{33}, \text{polymer}) \qquad 4.21b$$

$$f_{i1}^B - f_{i2}^B = H_i(\sigma_{11} - \sigma_{22}, \text{polymer}) \qquad 4.21c$$

where i = a, b or c. On examination of this hypothesis in the light of the experimental data, it appears that equations 4.21a and 4.21b do not have general validity. However, a plot of the difference, $f_{i1}^B - f_{i2}^B$ versus $\sigma_{11} - \sigma_{22}$ does give a master plot on which the uniaxial data of Dees and Spruiell can also be superimposed as shown in Figure 4.25. This striking result is not yet fully understood, but it appears to imply that the state of stress during crystallization determines at least certain features of the orientation distribution function that are measured by the difference in orientation factors, $f_{i1}^B - f_{i2}^B$. In the uniaxial (fiber) case, we have the special case that σ_{22} and f_{i2}^B are zero, and, hence, f_{i1}^B (or f_i) are uniquely determined by σ_{11} as previously found by Nadella et al.

In the same manner data for difference in amorphous orientation factors, $f_1^B - f_2^B$, both computed from the Rheo-Optical Law and calculated from Eq 2.57, page 27, using experimental crystalline orientation factors, measured birefriengence and crystallinity are plotted against principal stress difference, $\sigma_{11} - \sigma_{22}$ in Figure 4.26. The amorphous orientation predicted on the basis of the Rheo-Optical Law shows very low orientation level with positive sign. However, amorphous orientations of semi-crystalline HDPE which contain 30%

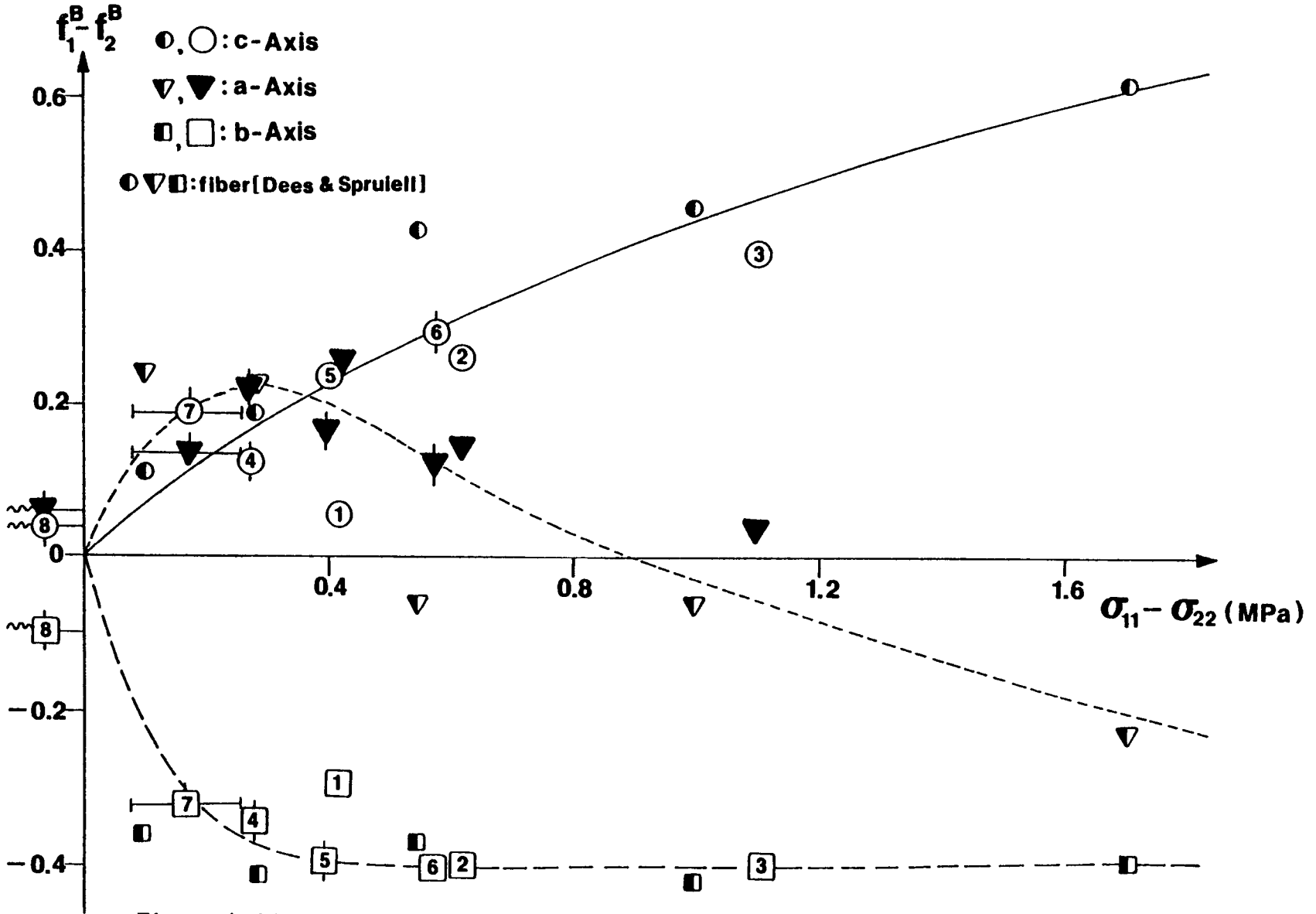

Figure 4.25 Differences in crystalline orientation factors along MD and TD, $f_1^B - f_2^B$, versus principal stress difference, $\sigma_{11} - \sigma_{22}$, with data for crystalline orientation factors of HDPE fiber as a function of take-up tension (Dees and Spruiell).

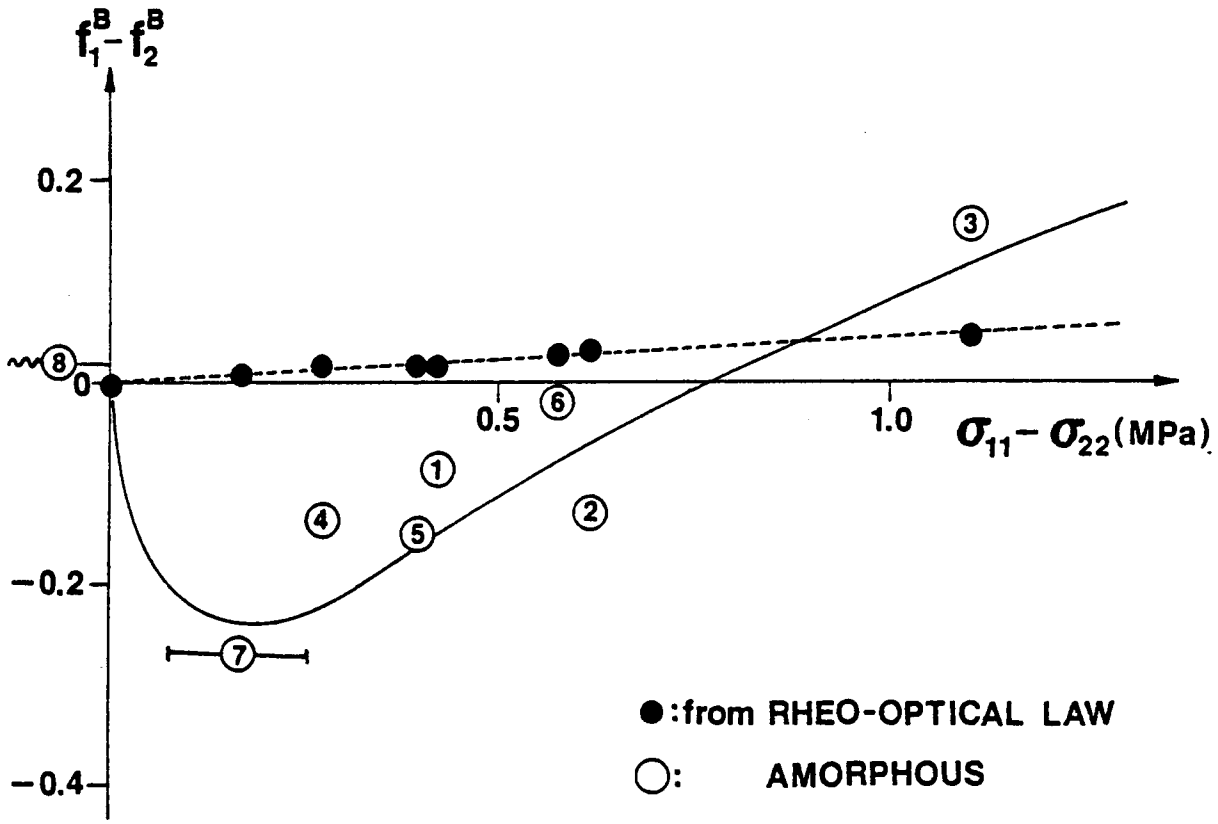

Figure 4.26 Differences in amorphous orientation factors along MD and TD, $f_1^B - f_2^B$, versus principal stress difference, $\sigma_{11} - \sigma_{22}$.

amorphous region predicted on the basis of the Rheo-Optical Law shows that the chains in the amorphous region are aligned rapidly along the transverse direction at first, then degree of orientation along the machine direction increases slowly (see the solid line in Figure 4.26). This may be due to the amorphous orientation containing a contribution from chain folds and only occurring in localized small regions which are constrained by the crystalline phase. The same tendency was observed by Matsumoto et al. for uniaxially stretched polypropylene (44) and poly(ethyleneterephtalate) films (43).

MORPHOLOGY OF POLYETHYLENE BLOWN FILM; The SAXS patterns of our samples, except sample 8, (see Figure 4.15, page 77) and the orientation data indicate that samples 1-7 exhibit more or less the row structures first described by Keller and Machin (33) for melt-extruded polyethylene films. The characteristic features of these row structures are lamellae stacked approximately along the machine direction together with orientations in which the b-axes become perpendicular to the machine direction while the c-axes gradually become more aligned along the machine direction, and the a-axis orientation factor increases at first but it then decreases. These latter changes in orientation accompany increasing drawdown stresses in the machine direction. The Keller-Machin model of row structure is illustrated for the strictly uniaxial case in Figure 4.27. Notice that at low stresses the lamellae are assumed to twist about the b-axes which are growing perpendicular to the MD. As stress increases this twisting is suppressed and the a-axes are assumed to gradually become

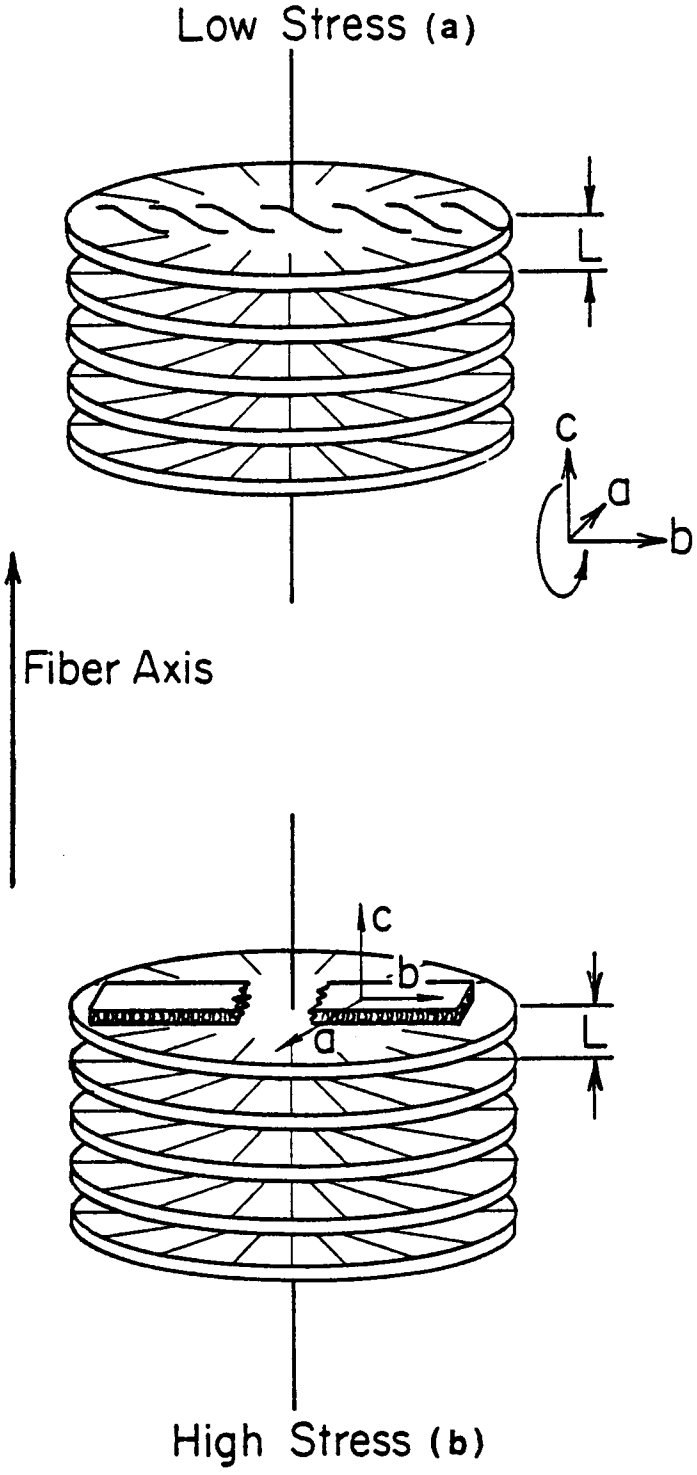

Figure 4.27 Row nucleated structures formed in filaments crystallized under stress.

more nearly perpendicular to MD.

Pole figures consistent with the ideal row structures illustrated in Figure 4.27 are shown schematically in Figure 4.28. It is to be noted that the twisted lamellae structure of Figure 4.27a produces a 200 pole figure which exhibits a slight maximum at the MD. The pole figures shown schematically in Figure 4.28a are equivalent to those shown for sample 1, Figures 4.7 and 4.8, pages 68 and 69. The "high stress" case shown schematically as Figure 4.28b is not achieved in any of the films produced in this research. The pole figures of samples 2 and 3 (see Figure 4.9 and 4.10, pages 70 and 71) would seem to be intermediate between the two cases shown in Figure 4.28.

The samples with constant blow-up ratio, 4-6, exhibit what appears to be a slightly modified form of the row structure. The SAXS patterns still indicate that the lamellae are stacked primarily along the machine direction in a fashion nearly equivalent to that for samples 1-3. But in this form, the orientation distribution is no longer uniaxial but exhibits a tendency for the a-axes to concentrate somewhat in the MD-ND plane.

In the biaxial case, sample 8, the morphology appears to be approximately equivalent to two superimposed row structures. One component exhibits the usual lamellar arrangement in which the lamellae are stacked along the machine direction (see Figure 4.15, page 77, and the two point pattern of Figure 4.16a, page 78). The second component contains lamellae stacked along the transverse direction (Figure 4.15 and Figure 4.16b). Furthermore, the 020 pole figure (Figure 4.14, page 75) shows that the b-axes tend to lie perpendicular to both MD and TD

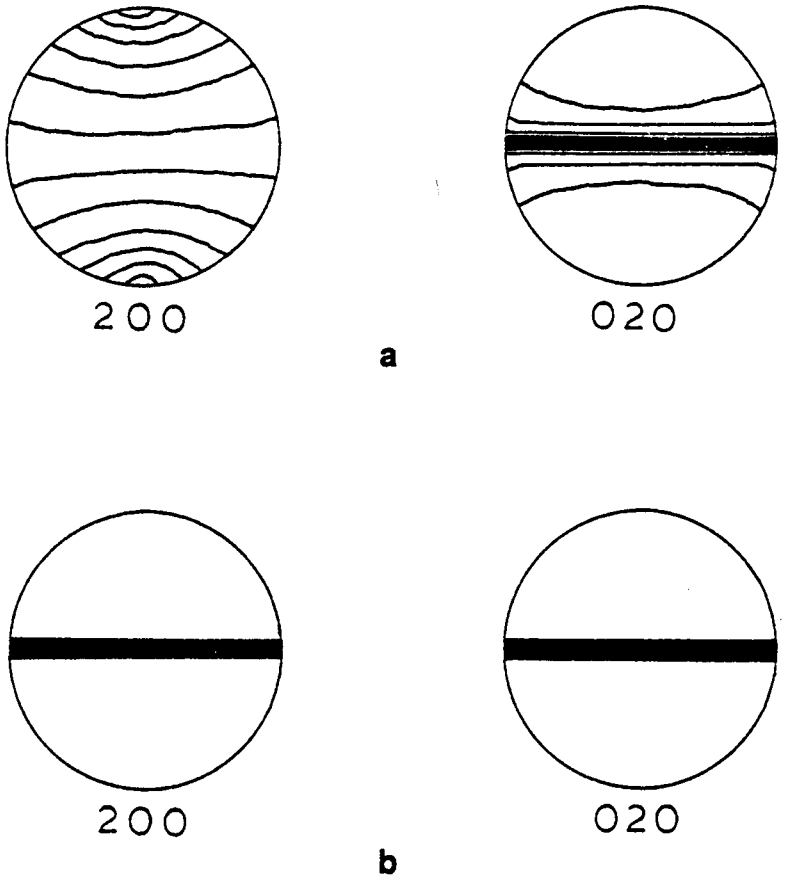

Figure 4.28 Schematic pole figures consistent with the ideal row structures.

(near ND) in this sample. It is not clear whether the morphology is some sort of lamellar "basketweave" or some form of duplex row structure with row nuclei aligned both along MD and along TD as illustrated in Figure 4.29. The SAXS patterns and orientation data appear to be consistent with either of these models. It might be possible to make a distinction between these two possibilities on the basis of replica transmission electron microscopy, but this has not yet been done.

Selected data from the literature for crystalline orientation in polyethylene were plotted in the orientation triangle diagram as shown in Figure 4.30 which were fully discussed by White and Spruiell (90). Almost all of the results from the literature show approximately uniaxial orientation along the machine direction rather than the transverse direction except Maddams and Preedy's (41) and Lindenmyer and Lustig's at the highest blow-up condition for LDPE (38). Some pole figures, such as pole figures for sample 1, 3 and 6, are similar to those reported by Maddams and Preedy (41).

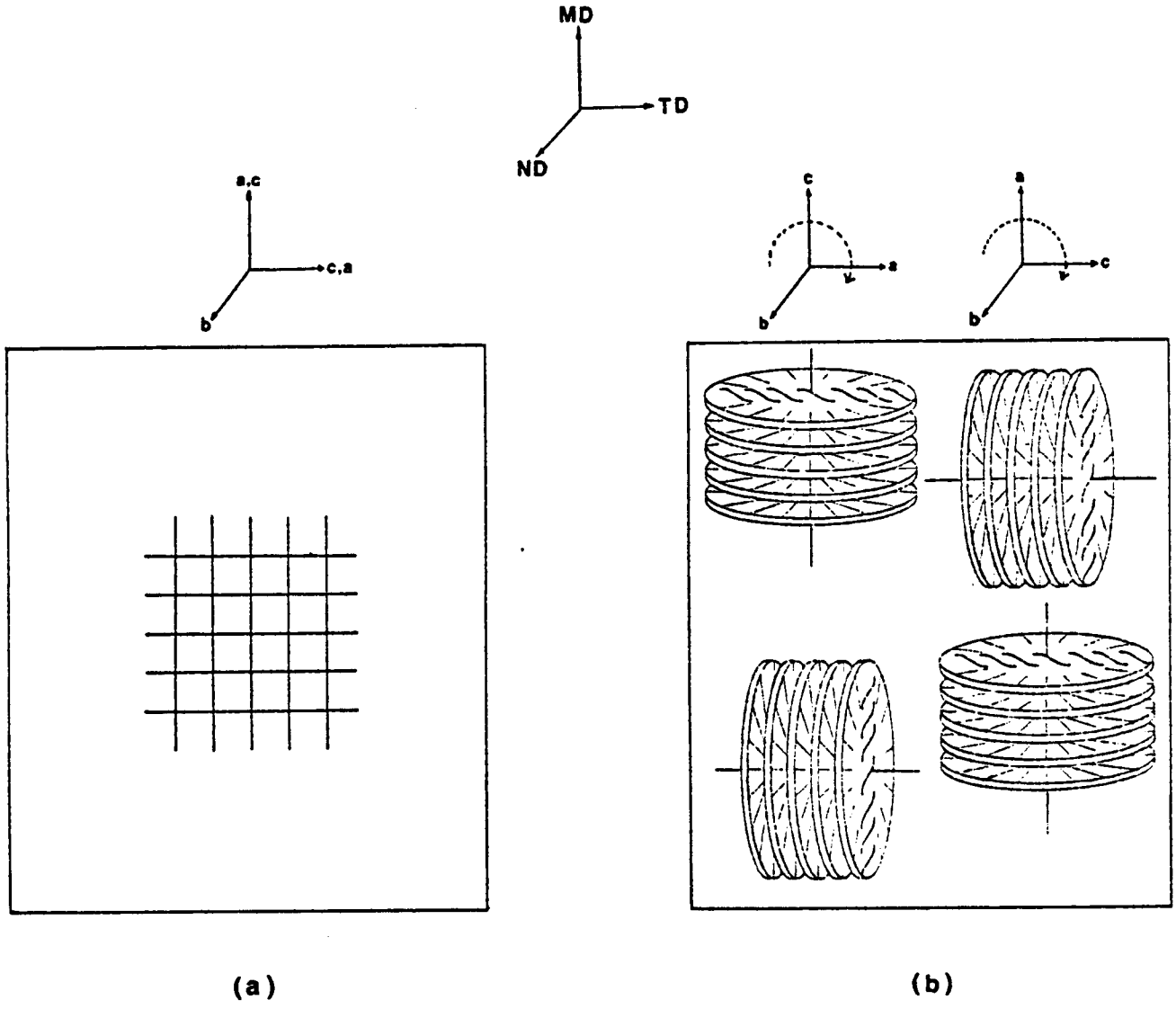

Figure 4.29 Possible morphologies for the biaxial sample; a:lamellar basketweave, b:duplex row structure.

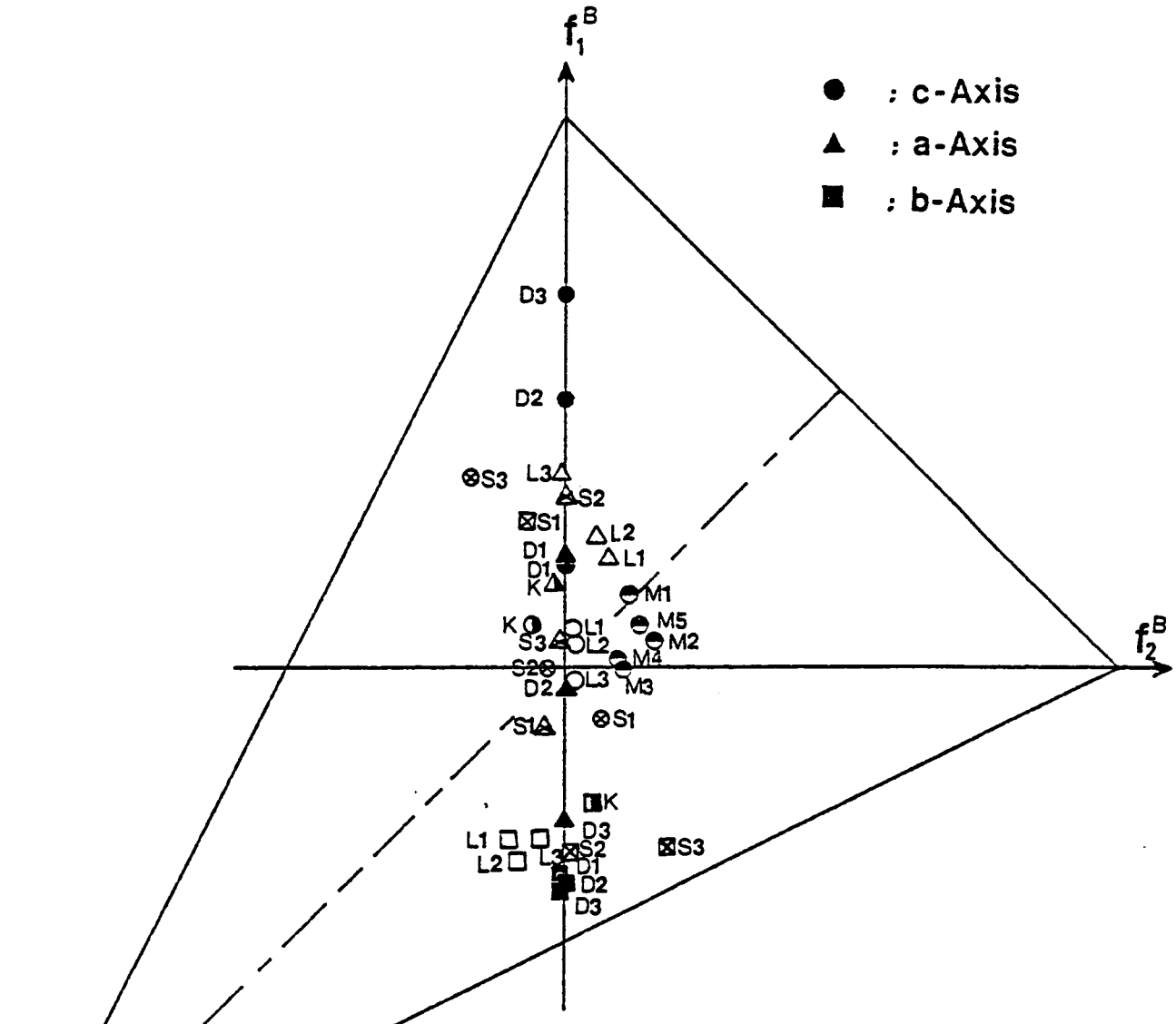

Label	Symbol	Material	Refernce	Comments
D	●	HDPE	Dees and Spruiell	melt spun fiber, samples PE01, PE02, and PE07
L	○	LDPE	Desper	blown film, samples 32A, 32B and 32 G
K	◑	HDPE	Kobayashi (quoted by Desper)	blown film
M	◒	HDPE	Maddams and Preedy	blown film, samples 1-5
S	⊗	PE	Desper and Stein	sample 1 unidirectionally crystallized, 2 and 3 cross-linked, low and high elongation, respectively.

Figure 4.30 Literature data for crystalline orientation of polyethylene samples (90).

CHAPTER 5

SUMMARY AND CONCLUSIONS

A series of approximately uniaxial and constant blow-up ratio samples and an equal biaxial sample for both polystrene and polyethylene were produced. Stress fields in the tubular film process were computed from the measured take-up tension and bubble pressure using the theory of Pearson and Petrie.

The in-plane and out-of-plane birefringence of the polystyrene film was found to depend upon the stresses at vitrification in the films. The values agreed quantitatively with the correlation of Oda, White and Clark, i.e. the birefringences were proportional to the differences in principal stresses (Rheo-Optical Law) with the same apparent stress-optical constant. The stress optical constant found was nominally equal to previously reported values of the stress optical constant of molten polystyrene.

The polyethylene films showed much higher levels of crystalline orientation than would be expected from the Rheo-Optical Law due to oriented nucleation and growth of crystals.

The results for White and Spruiell's biaxial orientation factors were plotted in an isosceles triangle diagram. Uniaxial states for both polystyrene and polyethylene lay along or close to the coordinate axis. A series of constant blow-up samples for polystyrene progressed with increasing drawdown from a position near the equal biaxial orientation line to a position representing nearly uniaxial orientation

while those for polyethylene moved further from uniaxial orientation with increasing drawdown. Films prepared according to the kinematic condition for equal biaxial orientation, namely $v_L / v_o = B$, exhibited nearly equal biaxial orientation. The data of both polystyrene and polyethylene lay close to the line at 45 to either coordinate axis but had rather low orientation levels in spite of the relatively high blow-up ratios, $B \cong 6 - 9$.

The orientatin for crystallizing polydethylene exhibited a bias in the direction with the highest stress, i.e. when the differences in orientation factors along the machine directin and transverse direction, $f_1^B - f_2^B$, were plotted against principal stress difference, $\sigma_{11} - \sigma_{22}$, these plots exhibit almost idendical features to that of the uniaxial case.

From WAXS and SAXS results the morphological changes of polyethylene with processing conditions are described. At low stress state, twisting of lamellae as they grow radially outward from the row nuclei first described by Keller was favored. This twisting decreased as the stress in the machine direction increased. A biaxially oriented sample exhibited a morphology which could be interpreted in terms of the superposition of two row structure components with one component having lamellae stacked along the machine direction and one component having lamellae stacked along the transverse direction.

LIST OF REFERENCES

LIST OF REFERENCES

1. Aggarwal, S. L. and G. P. Tilley, J. Polym. Sci., 18, 17 (1955).

2. Alexander, L. E., "X-Ray Diffaction Methods in Polymer, Science," Wiley, NY (1969).

3. Alfrey, T., SPE Trans., 5, 68 (1965).

4. Ast, W., Kunststoffe, 63, 427 (1973), ibid 64, 146 (1974).

5. Brewster, D., Phil. Trans. R. Soc., 106, 156 (1816).

6. Bryant, W. M. D., J. Polym. Sci., 2, 556 (1947).

7. Choi, K., J. L. White and J. E. Spruiell, J. Appl. Polym. Sci. (in press).

8. Clark, E. S. and C. A. Garber, Intern. J. Polym. Mat., 1, 31 (1971).

9. Dees, J. R. and J. E. Spruiell, J. Appl. Polym. Sci., 18, 1053 (1974).

10. Desper, C. R., J. Appl. Polym. Sci., 13, 169 (1969).

11. Desper, C. R. and R. S. Stein, J. Appl. Phys., 37, 3990 (1966).

12. Dhingra, V. K., M.S. Thesis, University of Tennessee, Knoxville (1979).

13. Dietz, W., J. L. White and E. S. Clark, Polym. Eng. Sci., 18, 273 (1978).

14. Dowd, L. E., SPE J. Bd., 28 (1972).

15. Drude, P., "Theory of Optics," Dover, NY (1900).

16. Farber, R. and J. M. Dealy, Polym. Eng. Sci., 14, 435 (1974).

17. Gross, S., "Modern Plastic Encyclopedia," McGraw-Hill (1969).

18. Gurnee, E. F., J. Appl. Phys., 25, 1232 (1954).

19. Hamana, I., "39 Kagakudojin," pp 128 (1969).

20. Hamana, I., M. Matsui and S. Kato, Meilland Textilber, 50, 382 (1969).

21. Han, C. D., "Rheology in Polymer Processing," Academic Press, NY (1976).

22. Han, C. D. and L. H. Drexler, J. Appl. Polym. Sci., 17, 2329 (1973).

23. Han, C. D. and J. Y. Park, J. Appl. Polym. Sci., 19, 3257 (1975).

24. Han, C. D. and J. Y. Park, J. Appl. Polym. Sci., 19, 3277 (1975).

25. Han, C. D. and R. Shetty, IEC Fund., 16, 49 (1977).

26. Hermans, P. H., J. J. Hermans, D. Vermaas and A. Weidinger, J. Polym. Sci., 3, 1 (1947).

27. Holmes, D. R. and R. P. Palmer, J. Polym. Sci., 31, 345 (1958).

28. Ishizuka, O. and K. Koyama, Sen-i-Gakkaishi, 32, T-43 (1976).

29. Janeschitz-Kriegl, H., Rheol. Acta, 16, 327 (1977).

30. Katayama, K., T. Amano and K. Nakamura, Kolloid Z. Z. Polym., 226, 125 (1968).

31. Keller, A., J. Polym. Sci., 15, 31 (1955).

32. Keller, A., Phil. Mag., 2, 1172 (1957).

33. Keller, A. and M. J. Machin, J. Macromol. Sci. Phys., B1(1), 41 (1967).

34. Kitao, T., S. Ohya, J. Furukawa and S. Yamashita, J. Polym. Sci., A2 11, 1091 (1973).

35. Kobayashi,K., in "Polymer Single Crystals," P. H. Geil, Ed., Interscience Publishers, NY, pp 456-475 (1963).

36. Krigbaum, W. R. and R. J. Roe, J. Chem. Phys., 41, 737 (1965).

37. Kuhn, W. and F. Grun, Kolloid Z., 101, 248 (1942).

38. Lindenmeyer, P. H. and S. Lustig, J. Appl. Polym. Sci., 9, 227 (1965).

39. Lobe, V. M. and J. L. White, Polym. Eng. Sci., 19, 617 (1979).

40. Lodge, A. S., Trans. Faraday Soc., 52, 120 (1956), "Elastic Liquids," Academic Press, NY (1964).

41. Maddams, W. F. and J. E. Preedy, J. Appl. Polym. Sci., 22, 2721 (1978), ibid 22, 2739 (1978), ibid 22, 2751 (1978).

42. Matsumoto, K. and I. Hirohiko, Sen-i-Gakkaish, 35, T-150 (1979).

43. Matsumoto, K., Y. Izumi and R. Imamura, Sen-i-Gakkaish, 29, T-377 (1973).

44. Matsumoto, K., K. Ishii, W. Kimura and R. Imamura, Sen-i-Gakkaishi, 27, 49 (1971).

45. Matsumoto, T. and D. C. Bogue, J. Polym. Sci. A2 15, 1663 (1977).

46. Matsumura, T. and H. Sasaki, Kobunshi Ronbunshu, Eng. Ed., 5, 9 (1976).

47. Maxwell, J. C., Phil Trans. Roy. Soc., 155 (1865).

48. McBrierty, V. J. and I. M. Ward, Brit. J. Appl. Phys., 1, 1529 (1968).

49. McRae, M. A. and W. F. Maddams, Makromol. Chem., 177, 473 (1976).

50. McRae, M. A., W. F. Maddams and J. E. Preedy, J. Mater. Sci., 11, 2036 (1976).

51. Menges, G. and W. predohl, Polym. Eng. Sci., 15, 394 (1975).

52. Middleman, S., "Fundamental of Polymer Processing," McGraw Hill, NY (1977).

53. Milagin, M. F., A. D. Gabarayeva and I. I. Shishkin, Polym. Sci. USSR, 12, 513 (1970).

54. Muller, F. H., Kolloid Z., 95, 138 (1941).

55. Nadella, H. P., H. M. Henson, J. E. Spruiell and J. L. White, J. Appl. Polym. Sci., 21, 3003 (1977).

56. Nagasawa, T., t. Matsumura, S. Hoshino and K. Kobayashi, Appl. Polym. Symp., 20, 275, 295 (1973).

57. Nichols, J. B., J. Appl. Phys. 25, 840 (1954).

58. Nomura, S. and H. Kawai, J. Polym. Sci., A2 8, 383 (1970).

59. Nomura, S., H. Kawai, I. Kimura and S. Kagiyama, J. Polym. Sci., 5, 479 (1967).

60. Nomura, S., H. Kawai, I. Kimura and M. Kagiyama, J. Polym. Sci., A2 8, 383 (1970).

61. Nomura, S., N. Nakamura and H. Kawai, J. Polym. Sci., A2, 9, 407 (1971).

62. Oda, K., J. L. White and E. S. Clark, Polym. Eng. Sci., 18, 53 (1978).

63. Omotoso, M., J. L. White and J. F. Fellers, J. Appl. Polym. Sci. (in press).

64. Page, L. and N. E. Adams, "Electrodynamics," Van Nostrand, NY (1940).

65. Park, J. Y., Ph.D. Thesis, Polytech. Inst. of NY (1975).

66. Pearson, J. R. A. and C. J. S. Petrie, J. Fluid Mech., 40, 1 (1970).

67. Pearson, J. R. A. and C. J. S. Petrie, J. Fluid Mech., 42, 609 (1970).

68. Pearson, J. R. A. and C. J. S. Petrie, Plastics and Polymers, 38, 85 (1970).

69. Petrie, C. J. S., Rheol. Acta, 12, 92 (1973).

70. Petrie, C. J. S., Plastics and Polymers, 42, 259 (1974).

71. Petrie, C. J. S., AICHE J., 21, 275 (1975).

72. Philippoff, W., J. Appl. Phys., 27, 984 (1956).

73. Roe, R. J. and W. R. Krigbaum, J. Chem. Phys., 40, 2608 (1964).

74. Roe, R. J. and W. R. Krigbaum, J. Appl. Phys., 35, 2215 (1964).

75. Roe, R. J., J. Appl. Phys., 36, 2024 (1965).

76. Rohn, C. L., J. Polym. Sci., C46, 161 (1974).

77. Spruiell, J. E. and J. L. White, Appl. Polym. Symp., 21, 121 (1975) and Polym. Eng. Sci., 15, 660 (1975).

78. Stein, R. S., J. Polym. Sci., 24, 383 (1957).

79. Stein, R. S., J. Polym. Sci., 31, 335 (1958).

80. Stein, R. S., J. Polym. Sci., 50, 339 (1961).

81. Stein, R. S. and F. H. Norris, J. Polym. Sci., 21, 381 (1956).

82. Swan, P. R., J. Polym. Sci., 56, 403 (1962).

83. Tanaka, H. and J. L. White, Polym. Eng. Sci., (in press).

84. Thomas, L. S. and K. J. Cleereman, SPE J., 28 (April), 61 (1972).

85. Till, P. H., J. Polym. Sci., 24, 301 (1957).

86. Treloar, L. R. G., Trans. Faraday Soc., 43, 277 (1947).

87. Wagner, M. H., Rheol. Acta, 15, 40 (1976).

88. Wales, J. L. S., Rheol. Acta, 8, 38 (1969).

89. White, J. L. and W. Dietz, J. Non-Newt. Fluid Mech., 4, 299 (1979).

90. White, J. L. and J. E. Spruiell, Polym. Eng. Sci. (in press).

91. Wilchinsky, Z. W., J. Appl. Phys. 30, 792 (1959).

92. Wilchinsky, Z. W., J. Appl. Polym. Sci., 7, 923 (1963).

93. Yasuda, H., H. Sugiyama and H. Yanagawa, Sen-i-Gakkaishi, 35, T-370 (1979).

94. Zeppenfeld, R., Kunststoffe, 61, 147 (1971).

95. Ziabicki, A. and K. Kedzierska, Kolloid Z., 171, 52 (1960), ibid 175, 14 (1961), J. Appl. Polym. Sci., 6, 111 (1962), ibid 6, 361 (1962).

APPENDIX

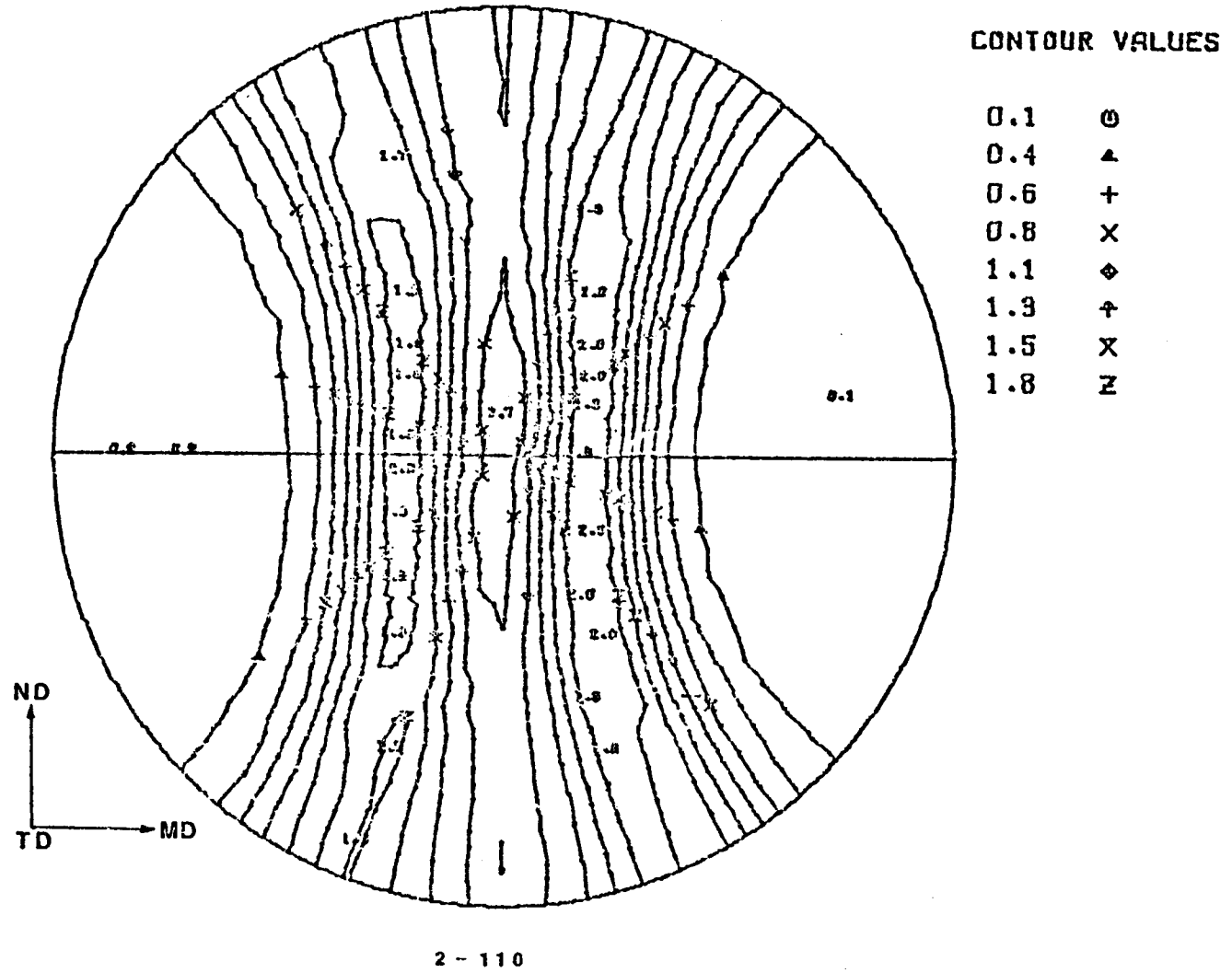

Figure A.1 110 pole figure of sample 2.

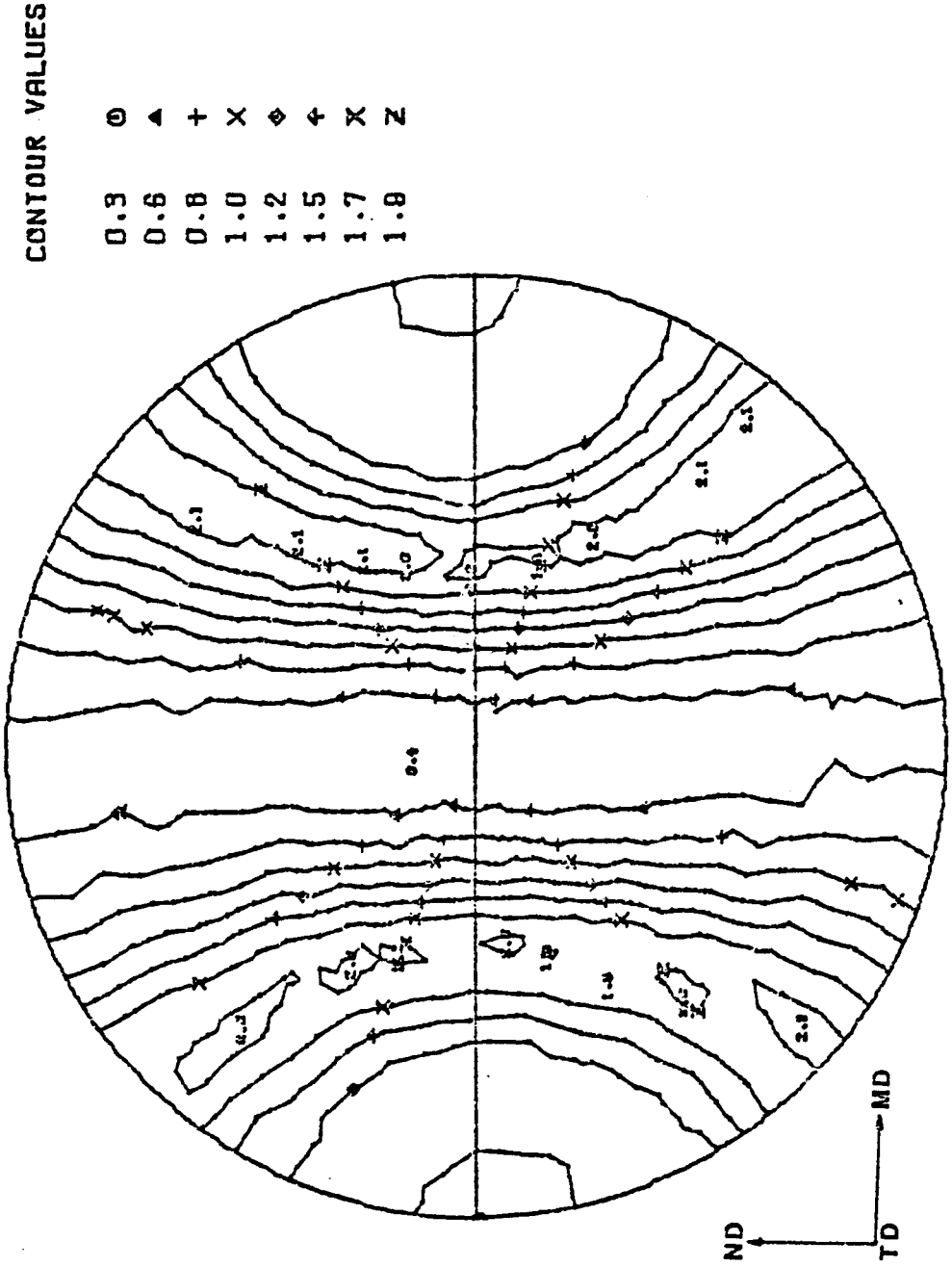

Figure A.2 200 pole figure of sample 2.

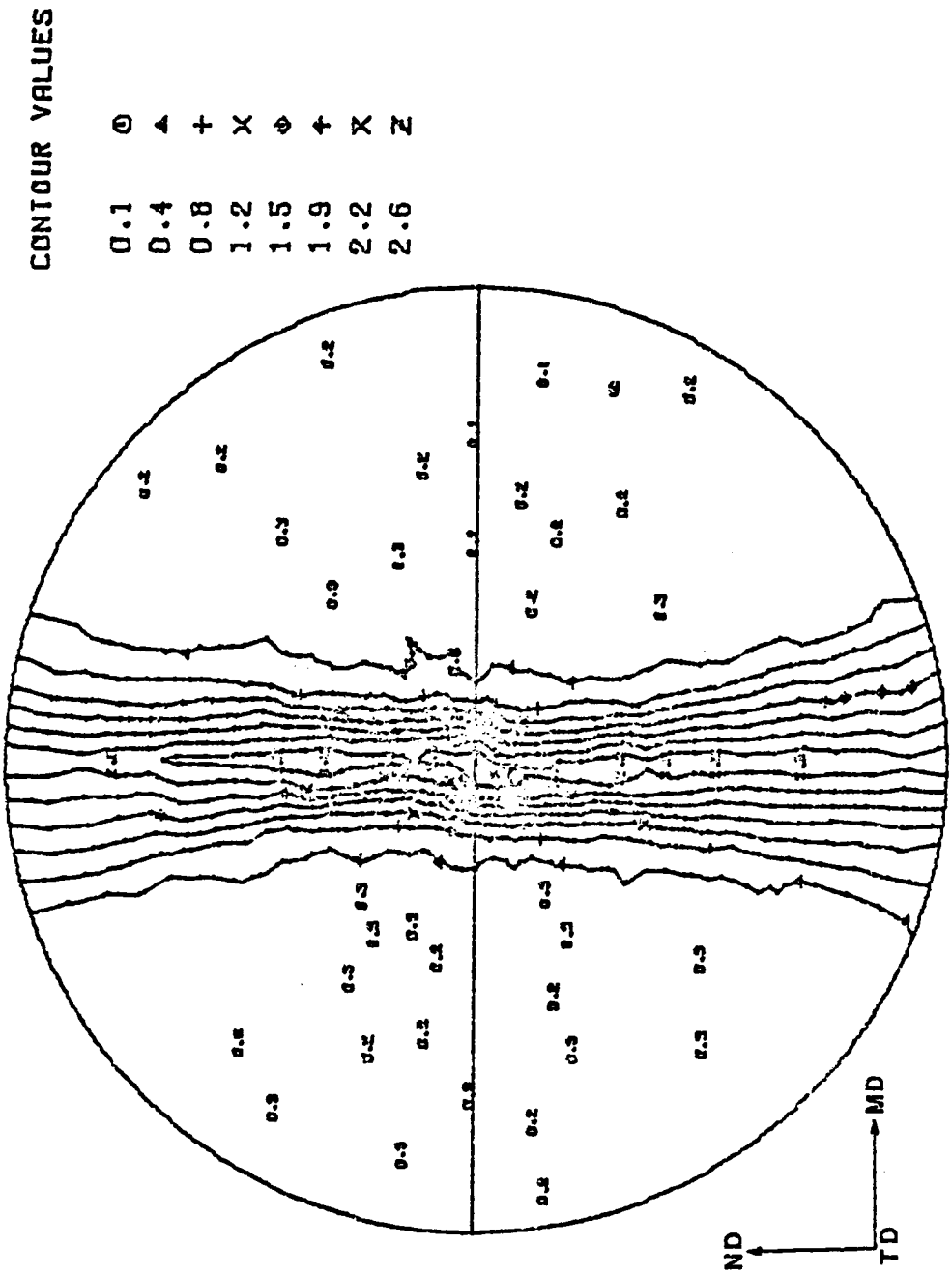

Figure A.3 020 pole figure of sample 2.

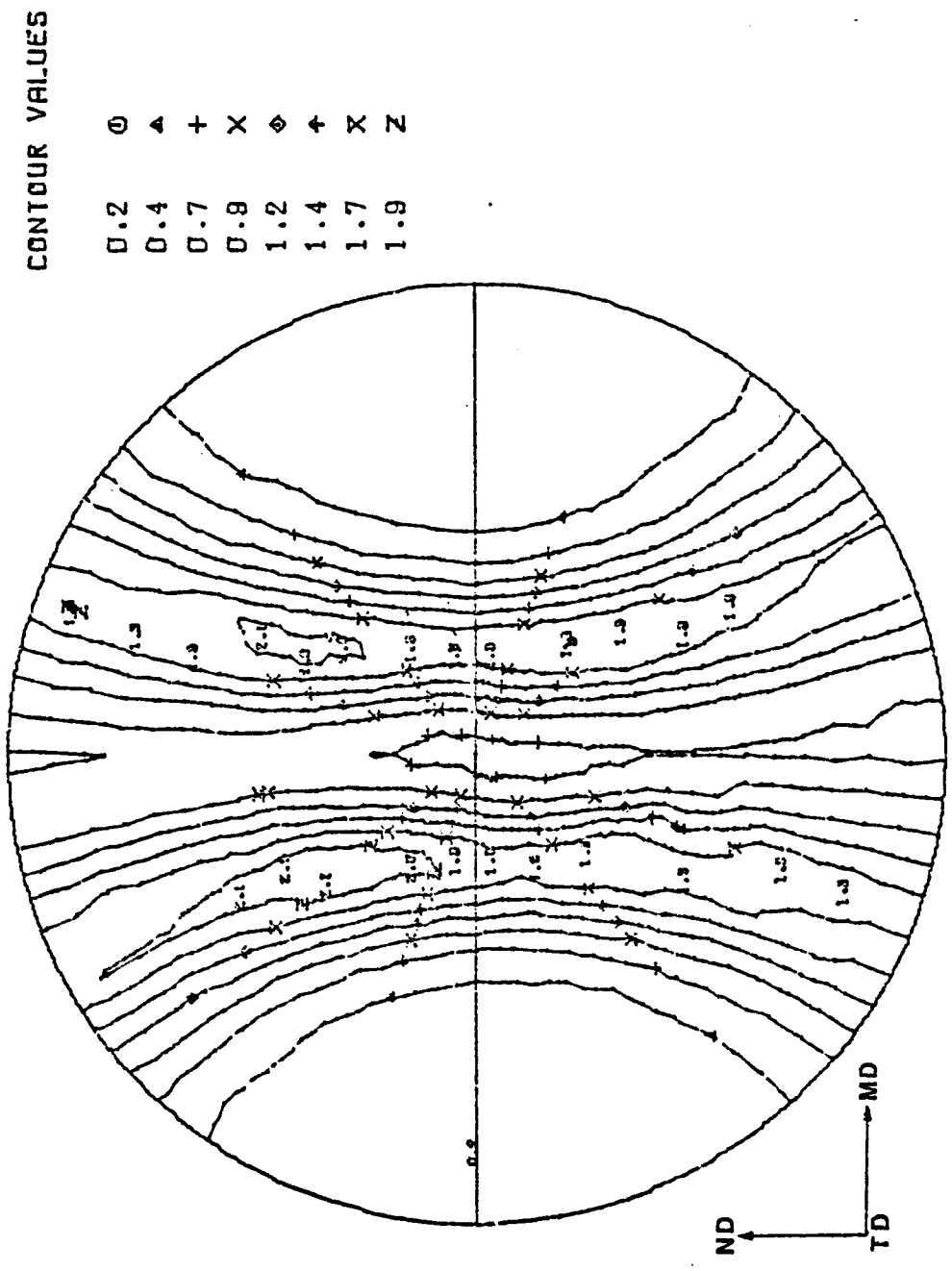

Figure A.4 110 pole figure of sample 4.

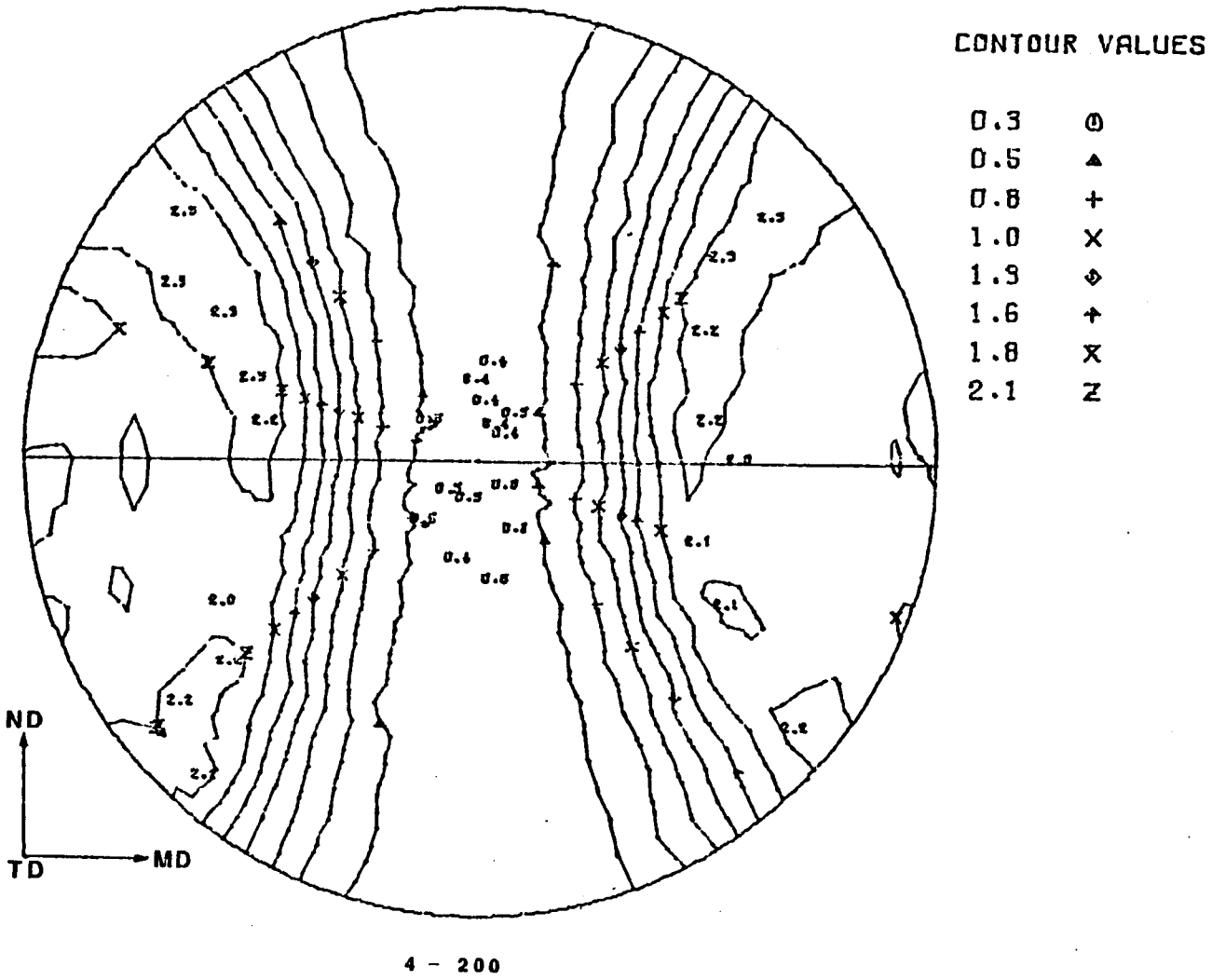

Figure A.5 200 pole figure of sample 4.

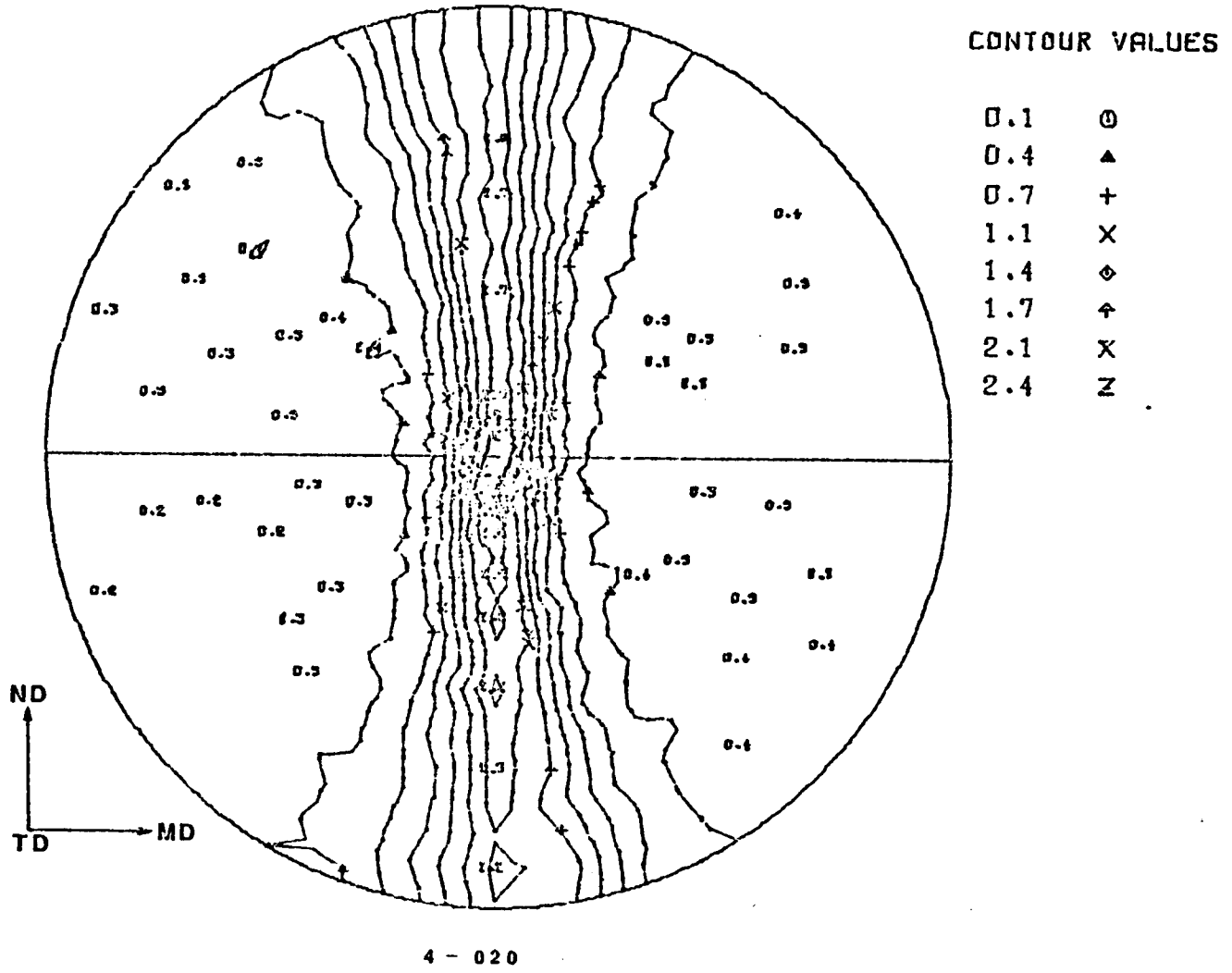

Figure A.6 020 pole figure of sample 4.

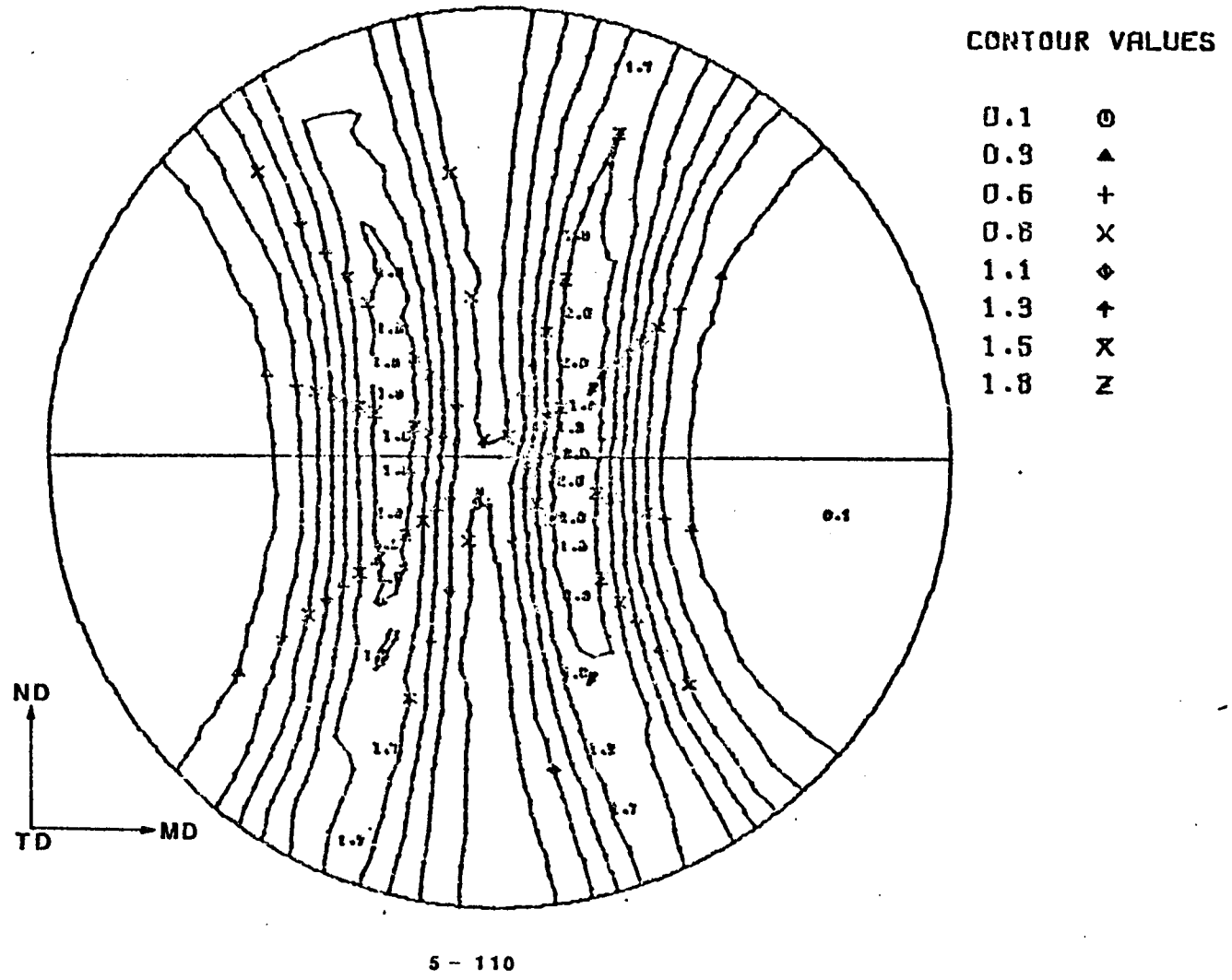

Figure A.7 110 pole figure of sample 5.

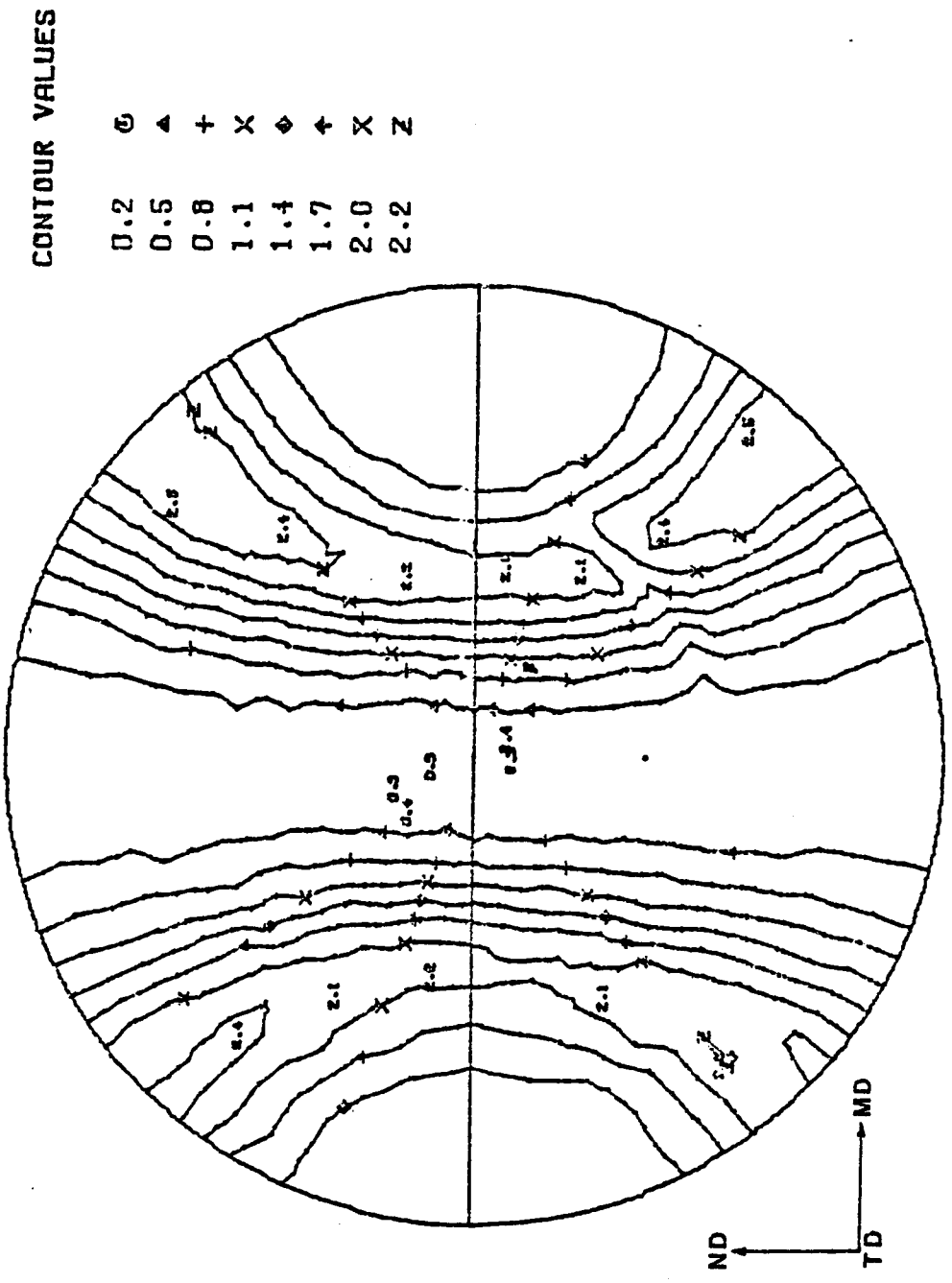

Figure A.8 200 pole figure of sample 5.

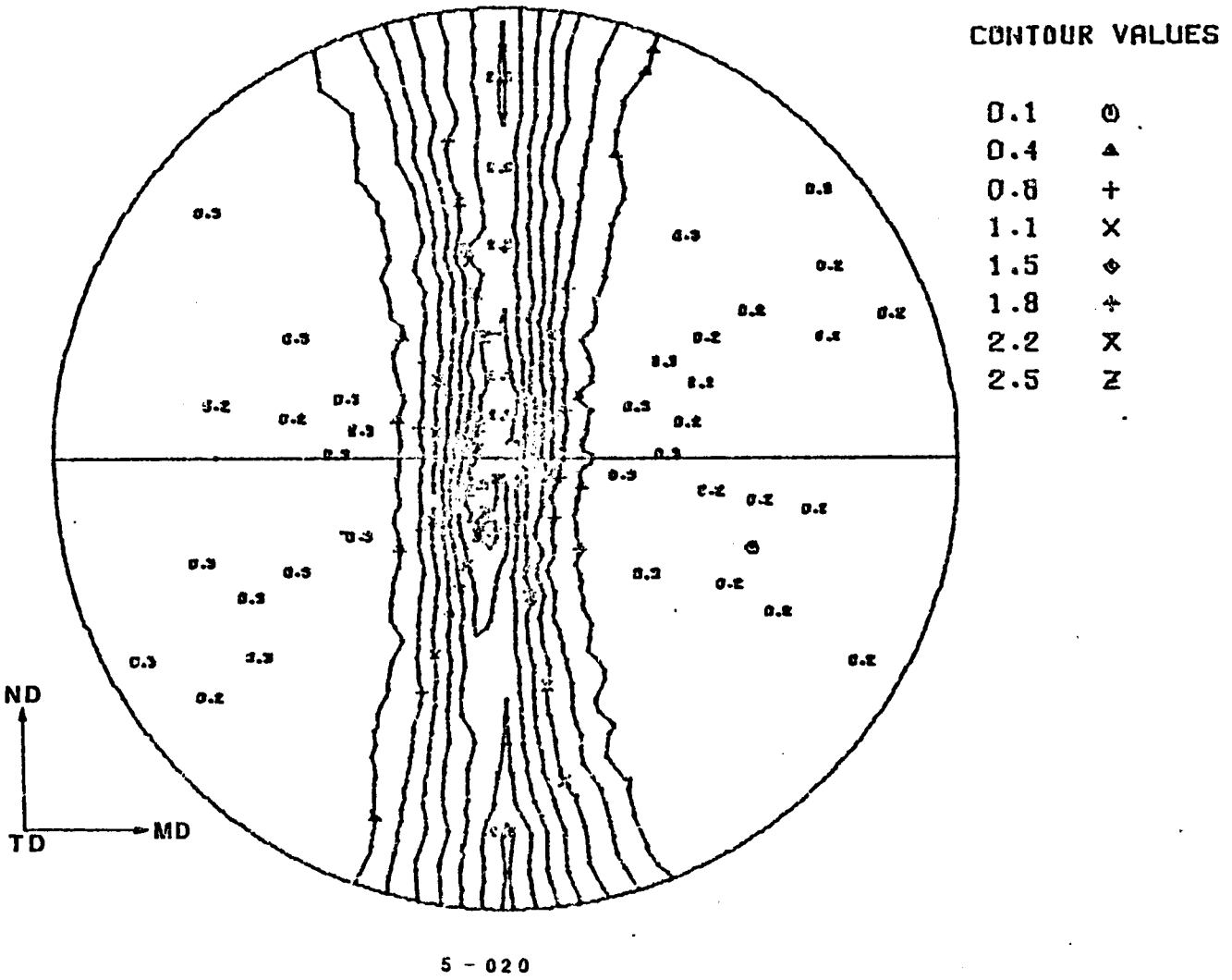

Figure A.9 020 pole figure of sample 5.

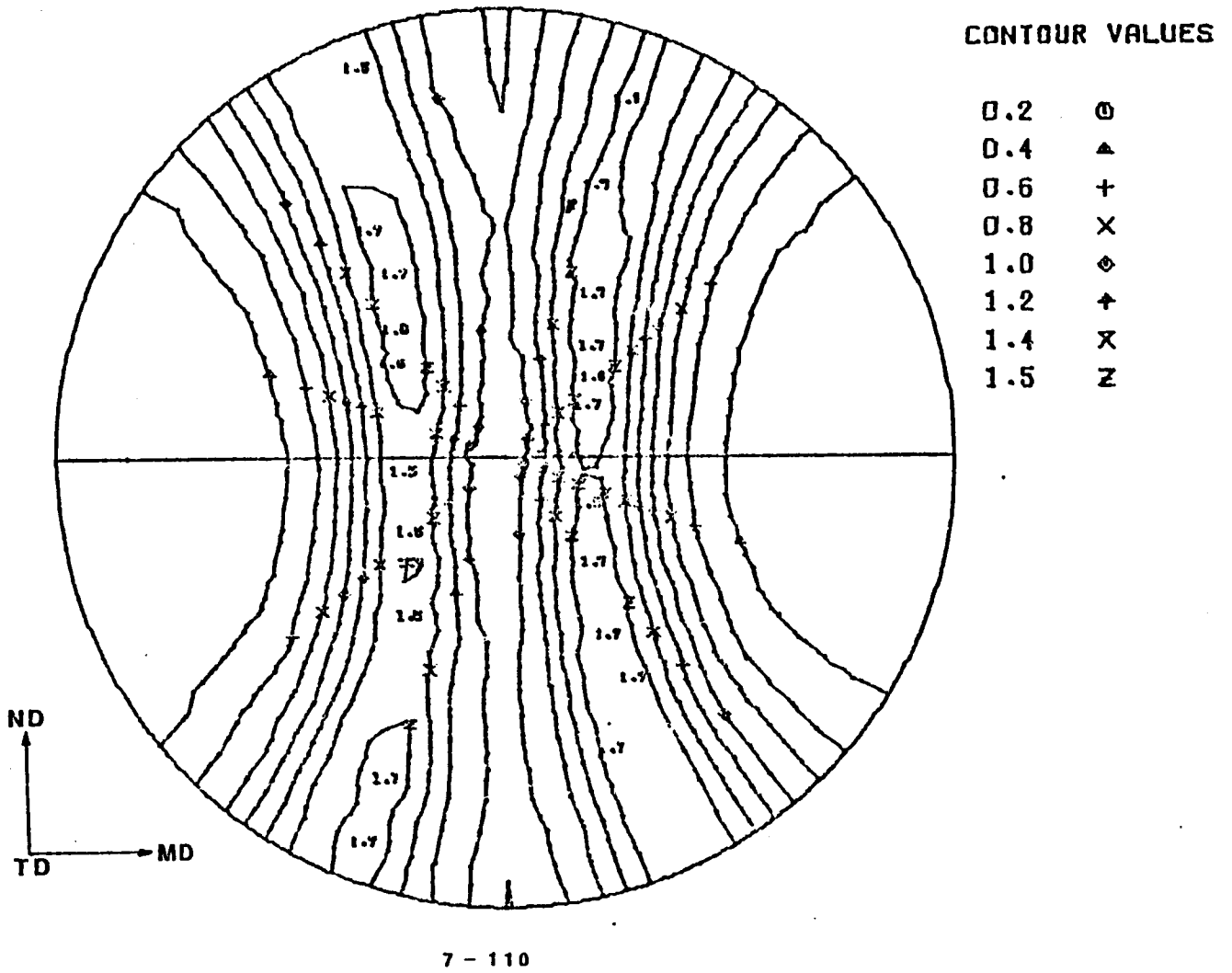

Figure A.10 110 pole figure of sample 7.

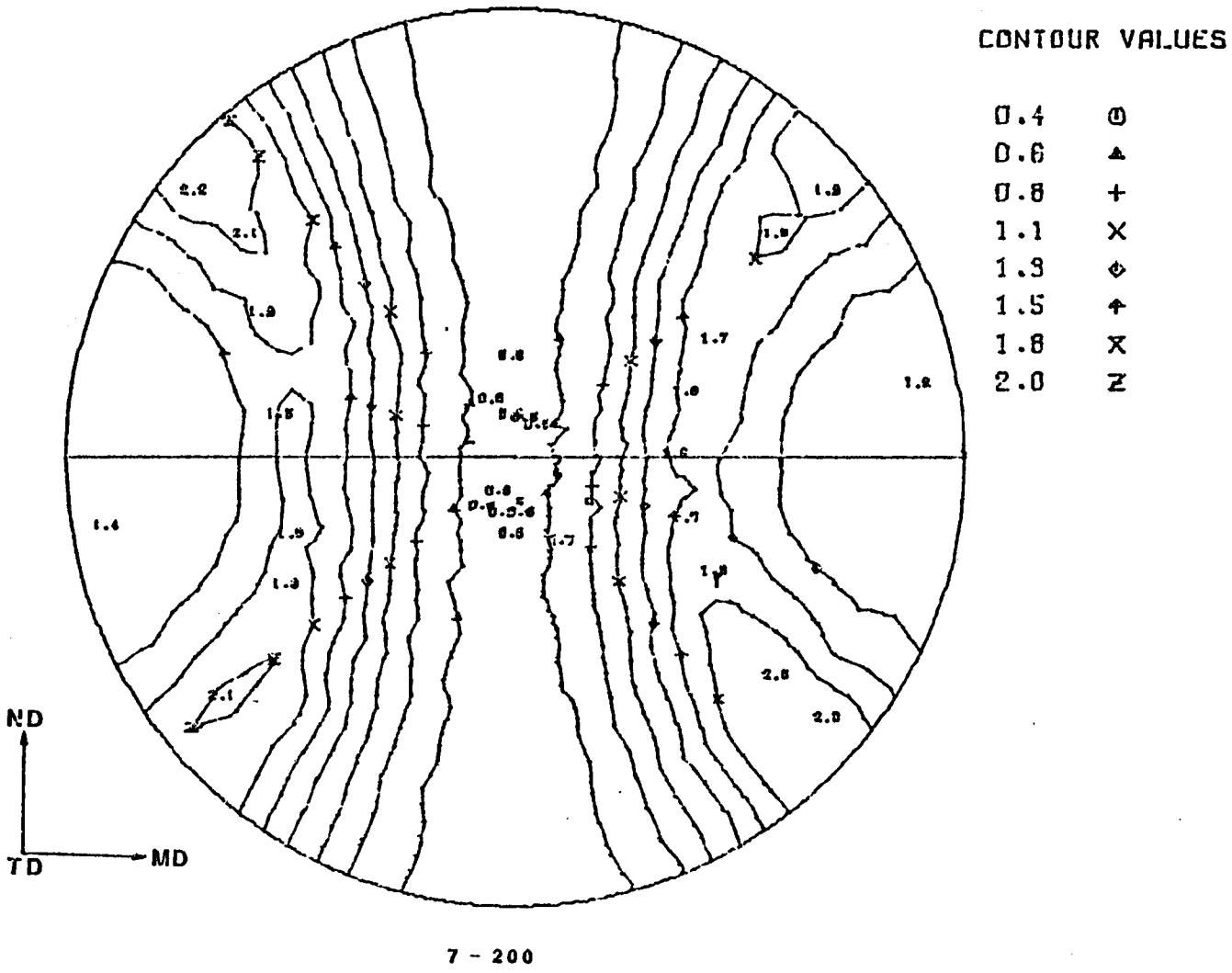

Figure A.11 200 pole figure of sample 7.

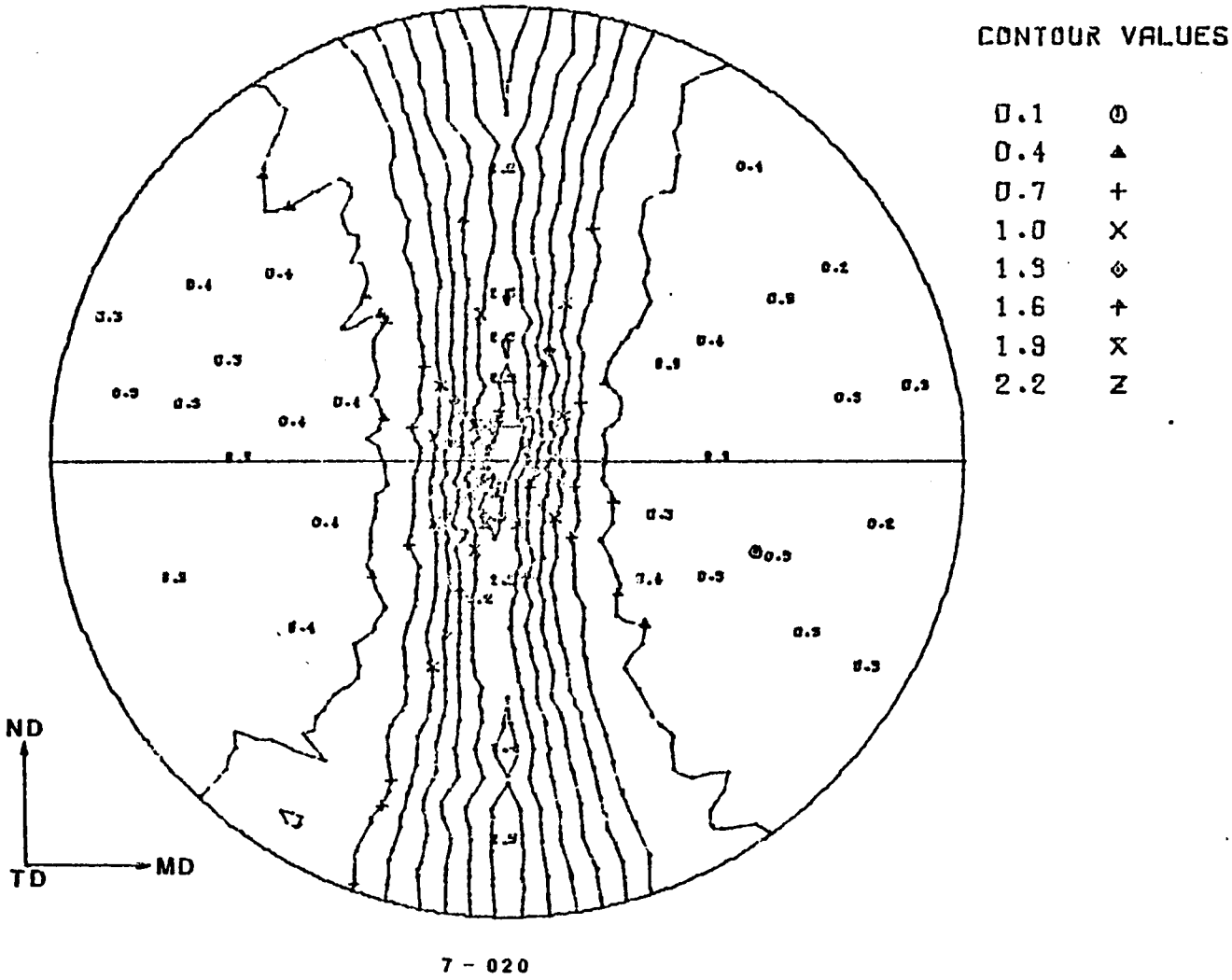

Figure A.12 020 pole figure of sample 7.

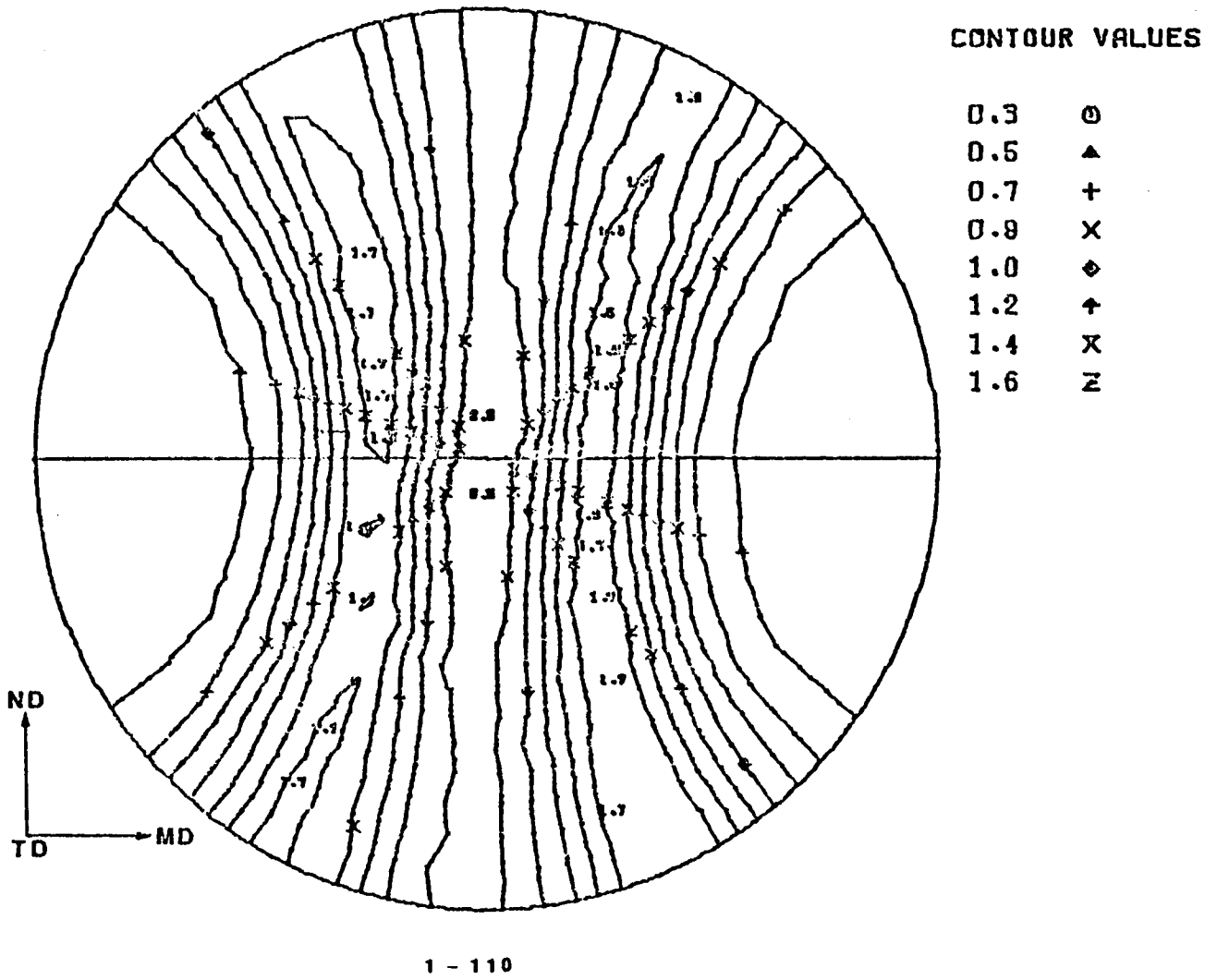

Figure A.13 110 pole figure of sample 1.

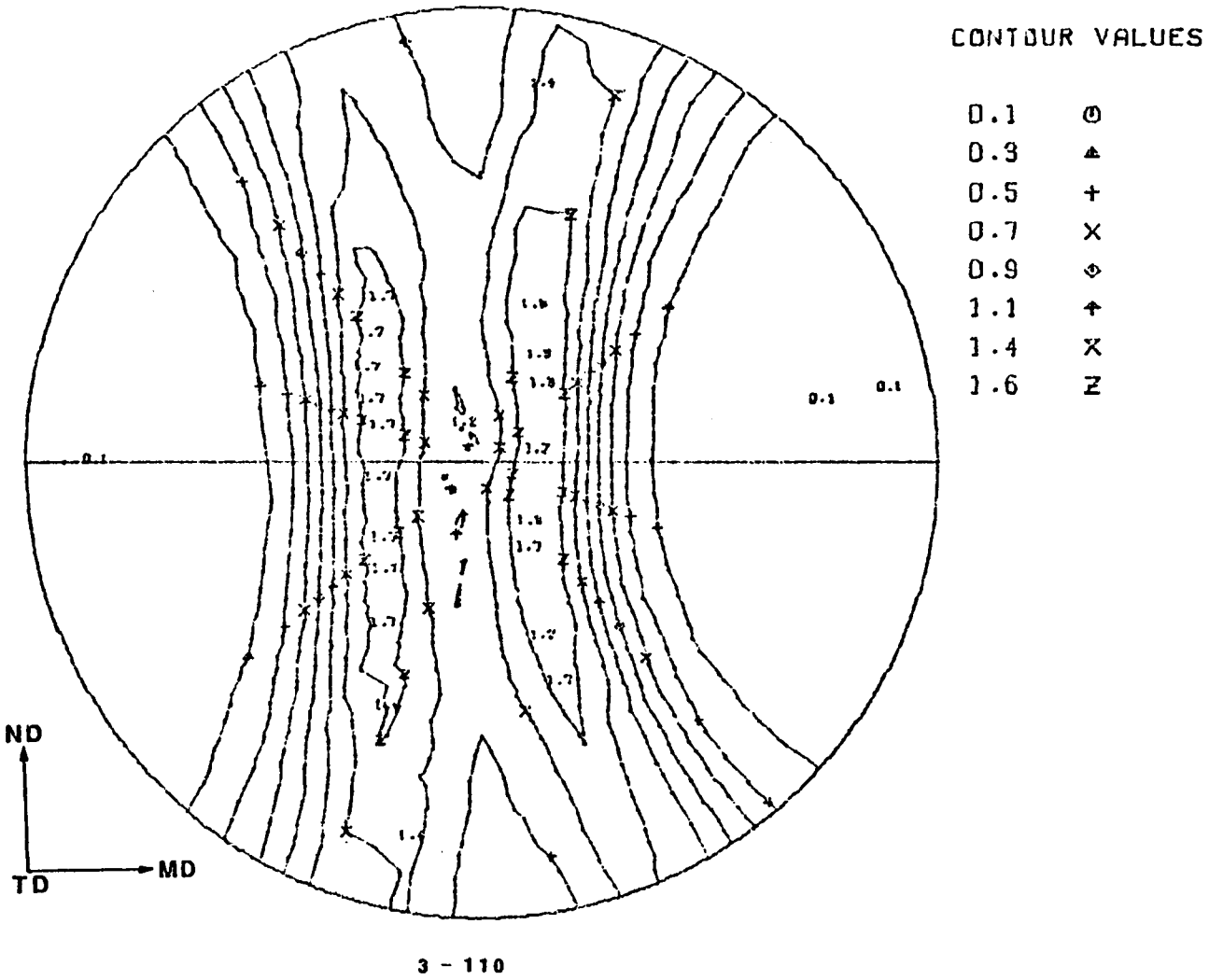

Figure A.14 110 pole figure of sample 3.

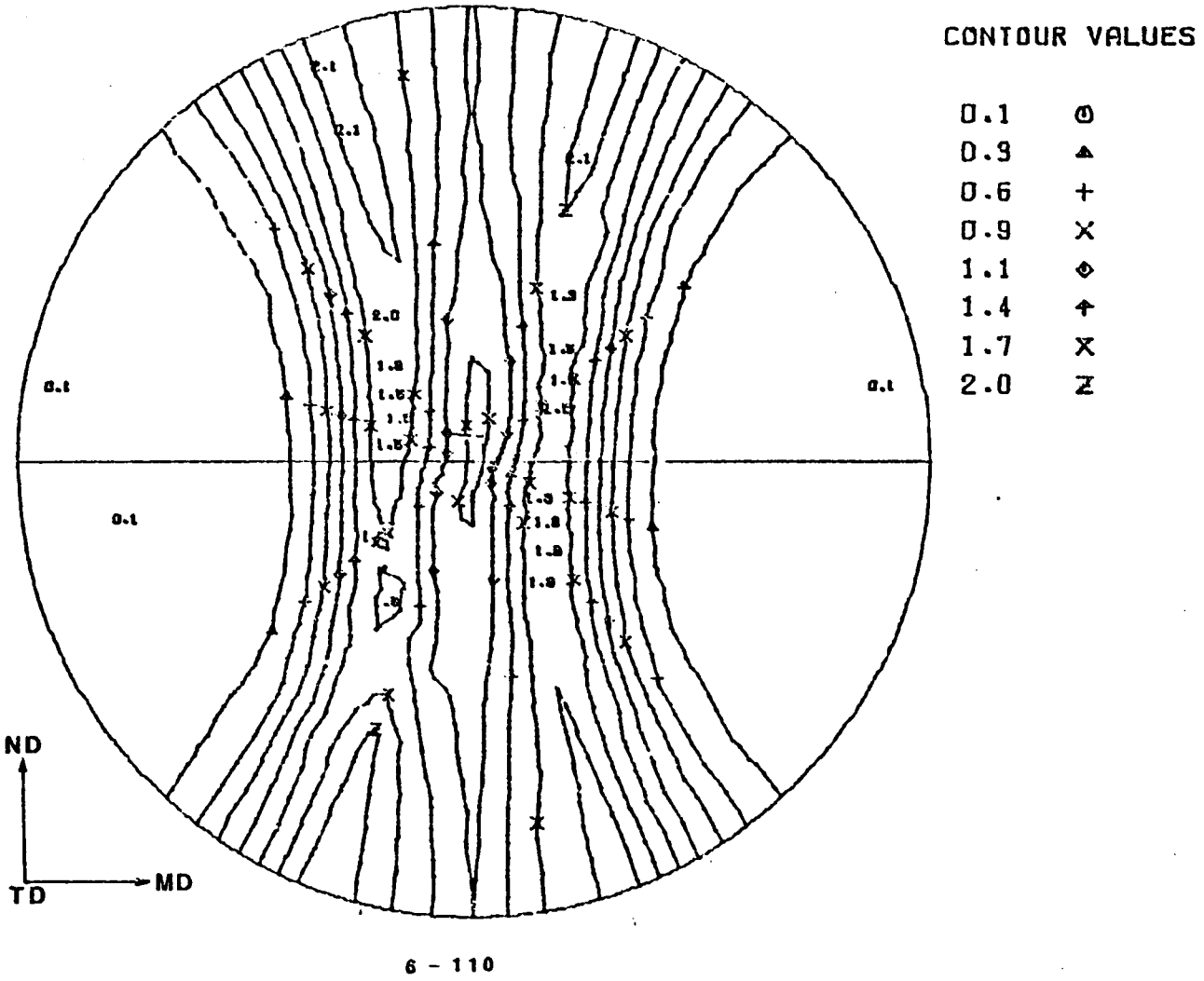

Figure A.15 110 pole figure of sample 6.

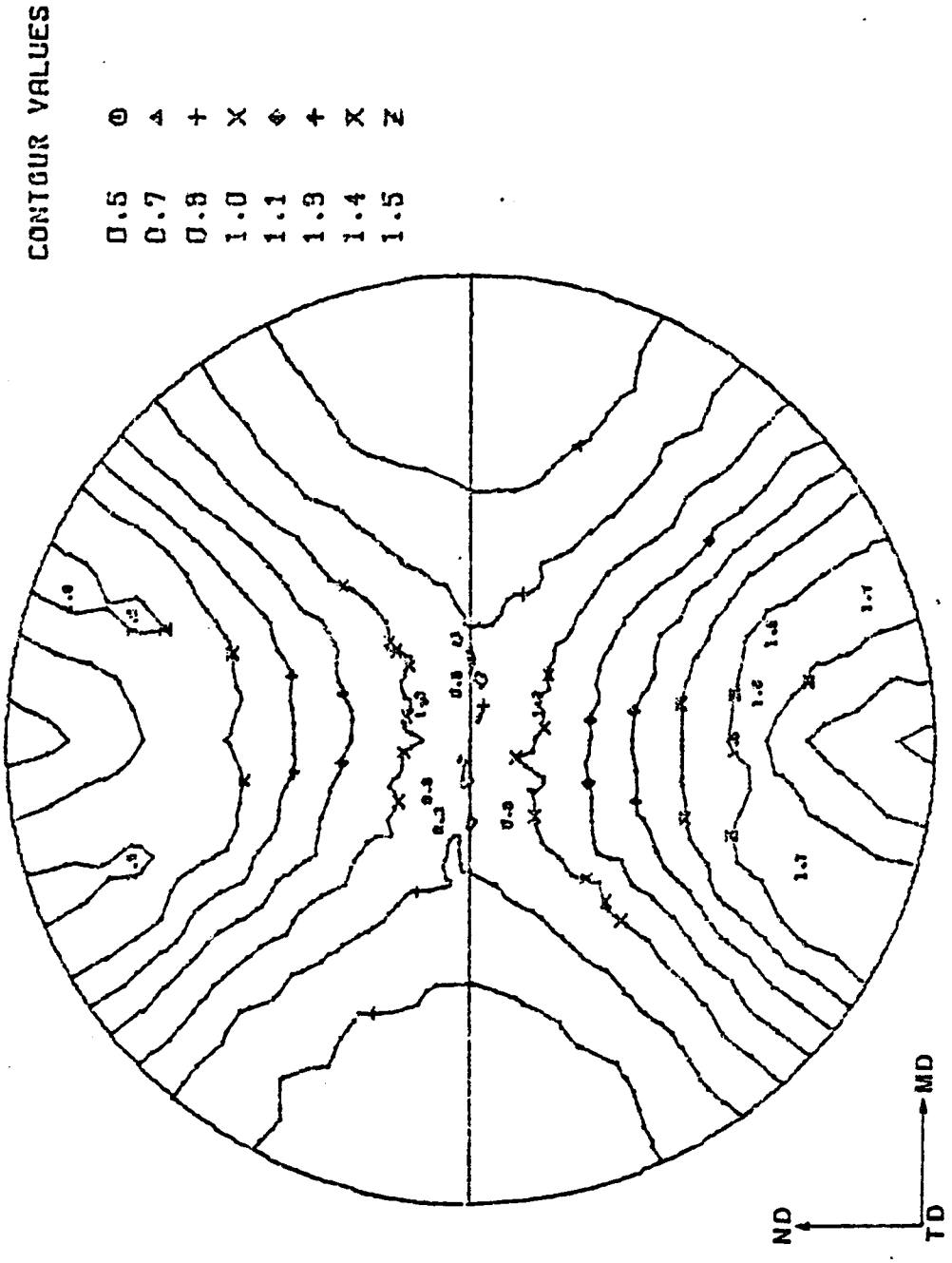

Figure A.16 110 pole figure of sample 8.

VITA

Kyung-Ju Choi was born in Seoul, Korea on September 14, 1945. He grew up in Jinju, Kyungnam province where he attened Govt. High School. In Feb. 1969 he graduated from the Yeungnam University with a Bachelor of Chemical Engineering degree. From Mar. 1969 to Feb. 1973 he served in the Hyupsung Commercial High School in Taegu as a science teacher. In Mar. 1973 he entered the Graduate School of the Kyungpook National University and in Feb. 1975 he received a Master's degree. After two years of teaching in the Kyungpook National University as a part time instructor, he entered the Graduate School of the University of Tennessee, Knoxville in September 1977.

The author is a member of SPE, the first president of the Korean Student Association at UT and a deacon of the Korean Presbyterian Church of Knoxville.

He is married to the former Jung-In Kang who is pursuing a Doctor of Philosophy at the same University with a pure mathematics major. They have a three-year-old son, Jin.